TECHNISCHE
UNIVERSITÄT
WIEN
Vienna University of Technology

DIPLOMARBEIT

Sub-millimetre and X-ray Observations of the Interstellar Medium

Ausgeführt am
Atominstitut der Technischen Universität Wien

in Zusammenarbeit mit dem
Institut für Astrophysik der Universität Wien

unter der Anleitung von
Univ.-Prof. Dr. Helmut Leeb, Univ.-Prof. João Alves, PhD,
und Dr. Jan Forbrich

durch

Birgit Hasenberger, BSc

Abstract

This work employs data sets obtained by various telescopes to deduce properties of the diffuse and dense interstellar medium and their variation throughout the sky. Due to the wavelength dependency of thermal dust emission and the extinction cross section, the sub-millimetre and the X-ray range are chosen to trace different constituents of the local interstellar medium. With new results from the *Planck* satellite recently published, measurements of dust emission in the microwave regime are available across the entire sky. Furthermore, the Orion Nebula Cluster has been surveyed by a number of high-resolution instruments, providing ideal conditions to study the dense interstellar medium in this region. Three analysis approaches utilising this wealth of data are followed: First, X-ray emission from extended sources is compared to thermal dust emission as observed by *Planck*. Second, the X-ray spectra of point sources are used to derive numerical values for the absorbing gas column density. Third, X-ray and sub-millimetre data covering the Orion Nebula Cluster are compared in order to derive the local gas-to-dust ratio. The new *Planck* data set necessitates a detailed study of the potential and limitations of the involved methods which is presented in this work. The complication that the compared quantities typically do not correspond to the same interstellar material is revealed. Additionally, restricting the analysis in such a way that X-ray absorption and thermal dust emission are comparable parameters is found to constitute a difficult undertaking. Nevertheless, the conducted studies are suggestive of significant variations in the properties of the interstellar medium, contradicting the common assumption of uniform characteristics across the sky.

Kurzfassung

Diese Arbeit verwendet Daten, die von verschiedensten Teleskopen gewonnen worden sind, um die Eigenschaften des diffusen und dichten interstellaren Mediums und deren räumliche Veränderung über den gesamten Himmel hinweg abzuleiten. Aufgrund der Wellenlängenabhängigkeit der thermischen Staubemission und des Extinktionswirkungsquerschnittes werden der Submillimeter- und der Röntgenbereich gewählt, sodass unterschiedliche Bestandteile des lokalen interstellaren Medium beobachtet werden können. Durch die vor Kurzem veröffentlichen Ergebnisse des Satelliten *Planck* sind Staubemissionsmessungen für den gesamten Himmel verfügbar. Weiters wurde der Cluster des Orionnebels mit einer Reihe von hochauflösenden Instrumenten vermessen, was ideale Voraussetzungen für die Untersuchung des dichten interstellaren Mediums in dieser Region schafft. Um die Fülle an Daten zu nutzen, werden im Zuge der Analyse drei Vorgehensweisen verfolgt: Erstens wird die Röntgenemission von ausgedehnten Quellen mit den Mikrowellenbeobachtungen von *Planck* verglichen. Zweitens werden Röntgenspektren von Punktquellen verwendet, die die Ableitung der absorbierenden Gassäulendichte erlauben. Drittens werden Röntgen- und Submillimeterdaten des Orionnebels verglichen um das lokale Gas-zu-Staub-Verhältnis zu bestimmen. Der neue *Planck*-Datensatz erfordert eine detaillierte Untersuchung des Potentials und der Einschränkungen der angewandten Methoden, die in dieser Arbeit präsentiert wird. Die grundlegende Komplikation, dass die zu vergleichenden Daten typischerweise nicht dasselbe interstellare Material widerspiegeln, wird aufgezeigt. Gleichzeitig stellt es sich als schwierig heraus, die beiden Datensätze in einer solchen Weise zu beschränken, dass sie vergleichbar sind. Nichtsdestotrotz legen diese Analysen eine wesentliche räumliche Änderung der Beschaffenheit des interstellaren Mediums nahe, was der üblichen Annahme einheitlicher Eigenschaften über den gesamten Himmel hinweg widerspricht.

Contents

1 Introduction

Within a galaxy, the space between stars is pervaded with gas and dust, matter which is commonly referred to as the interstellar medium (ISM). The ISM provides the material out of which stars are formed and at the same time, stars eject matter into interstellar space during their lifetime and final stages of existence (Draine, 2011a). Due to this constant mass flow between stellar objects and the ISM, it is involved in various dynamic processes and exhibits substantial changes in its properties. In the form of cold, dense clouds of mostly molecular gas the ISM represents a nursery for young stars, while it is heated and expanded by energetic events to produce a thin and hot plasma (Klessen and Glover, 2014). Similarly, the characteristics of the intermixed dust vary as a result of changing physical conditions which allow different sets of chemical reactions (Ferrière, 2001).

Although numerous properties of the ISM have been shown to vary across the sky (e.g., Mathis and Wallenhorst, 1981; Vuong et al., 2003), the knowledge on the 3-dimensional distribution of its different phases is limited and fundamental parameters such as the gas-to-dust ratio are assumed to be constant for many applications. The aim of this work is to investigate whether differences in the properties of the ISM can be determined and if so, to attempt to quantify them. As the emission and extinction properties of the ISM vary considerably with wavelength, observations in two different energy ranges are employed to deduce the characteristics of interstellar gas and dust. Thermal dust emission in the sub-millimetre regime provides a measure of the amount of dust along the line of sight, whereas photoelectric absorption attenuates radiation from an X-ray source, a process which can be used to derive the absorbing gas column density. With the extensive catalogues and all-sky surveys available in both wavelength ranges from telescopes such as ROSAT, XMM-*Newton* or *Planck*, a comparison between X-ray and sub-millimetre data can be conducted, yielding valuable information on the properties of the diffuse ISM if a correlation is revealed. Focussing on a region dominated by cold and dense gas, the Orion Nebula Cluster and its associated young stellar objects are examined with high-resolution data from *Chandra* and *Herschel*.

This work is intended to contribute to the knowledge on the properties of the ISM and their variation across the sky by analysing both diffuse, large-scale structures and the Orion Nebula Cluster as an example of an area where the dense ISM plays a vital role. Insights in this area of research are of importance not only for the understanding of the ISM itself, but also for extragalactic studies, where the ISM acts as an obscuring layer, and for theories concerning numerous stages of stellar evolution.

2 Properties of the Interstellar Medium and their Observation

The mixture of gas and dust that fills the space between stars within a galaxy is referred to as the interstellar medium. A continuous mass flow between stars and the ISM is maintained, as it provides the material out of which stars are formed, and at the same time stars add to the mass of the ISM by the ejection of matter into interstellar space, e.g. via stellar winds or supernovae (Draine, 2011a). These dynamic processes lead to temporal and spatial variations of the properties of the interstellar medium.

2.1 Phases of the Interstellar Medium

The state of the ISM is often described by phases according to its physical and chemical properties, for example temperature, density and the fraction of ionised particles. Although there is no general consensus on the definition of these phases, a summary of one possible classification is given in Table 1.

Interstellar matter is not distributed uniformly and it is estimated that, on the one hand, approximately half of the total mass of the ISM is present in discrete clouds, filling 1–2 % of the interstellar volume and mainly consisting of molecular gas and the cold neutral medium. On the other hand, warm and hot matter is spread out between these clouds (Ferrière, 2001). In this work, different states of the ISM are characterised by the terms 'dense' and 'diffuse', where 'dense ISM' refers to cold clouds mainly containing molecular gas, while the 'diffuse ISM' refers to less dense, large-scale structures.

Phase	Temperature [K]	Density [cm^{-3}]	Fractional ionisation	State of hydrogen
Molecular gas	10 – 20	$> 10^2$	$< 10^{-6}$	molecular
Cold neutral medium	50 – 100	20 – 50	$\sim 10^{-4}$	neutral atomic
Warm neutral medium	6 000 – 10 000	0.2 – 0.5	~ 0.1	neutral atomic
Warm ionised medium	$\sim 8\,000$	0.2 – 0.5	1.0	ionised
Hot ionised medium	$\sim 10^6$	$\sim 10^{-2}$	1.0	ionised

Table 1: Phases of the ISM, taken from Klessen and Glover (2014) and Ferrière (2001), along with their temperature, number density, fractional ionisation and the dominating state of hydrogen atoms.

2.2 Constituents of the Interstellar Medium

The ISM consists of ionised, atomic and molecular gas as well as solid particles, which are commonly referred to as dust. Generally, the abundances of elements in the local ISM are presumed to be similar to those of the Sun's photosphere, and the abundances in interstellar dust grains are inferred from a comparison between solar and gas-phase abundances. Atoms of chemical elements that are under-abundant in the gas phase relative to solar values are referred to as being depleted from the gas phase and are assumed to be incorporated into dust grains (Draine, 2011a). In the gaseous component of the ISM, approximately 70 % of the total mass can be attributed to hydrogen, 28 % to helium and 2 % to heavier species (Klessen and Glover, 2014). The fraction of atoms in the ionised, atomic or molecular state varies considerably depending on the phase of the ISM (see Section 2.1).

Dust grains in the ISM primarily contain amorphous silicates and carbonaceous material, e.g. graphite, amorphous carbon or polycyclic aromatic hydrocarbons (PAHs), and to a lesser extent metal oxides as well as metallic iron (Draine, 2011b; Kruegel, 2003). The total dust mass is dependent on the grain size distribution and the exact composition of the dust, parameters which are usually not known. However, observations can provide restrictions on these values. For example, an early dust grain model developed by Mathis et al. (1977) assumes spherical graphite and silicate particles and is capable of reproducing the extinction curve for the diffuse ISM and wavelengths between 0.1 and 1 μm. The grain size distribution is modelled by a power law of index -3.5 in a radius range from approximately 5 nm to 1 μm, which results in a large population of grains with small radii. More up-to-date models, e.g. by Zubko et al. (2004), additionally consider PAHs, amorphous carbon and ice (amongst others) as grain constituents and the presence of voids within dust grains.

Although gas and dust properties have been observed to vary between different phases of the ISM (e.g., Carrasco et al., 1973; Ferrière, 2001; Mathis and Wallenhorst, 1981), the gas-to-dust mass ratio is commonly assumed to be constant throughout the Milky Way with a value of approximately 100 (Spitzer, 1978). Lower ratios have been deduced, for example, from observations towards ρ Ophiuchi (Carrasco et al., 1973; Vuong et al., 2003), a nearby star-forming region.

2.3 Emission and Extinction Properties

The presence of interstellar matter was first inferred from the observations of ‘dark clouds’, regions in the sky that appeared to contain no stars (Barnard, 1907). This lead to the concept that light emitted from stars located behind these clouds of interstellar matter is absorbed and scattered on its way to the observer. The joined effects of absorption and scattering, which are referred to as extinction, thus result in a reduction of the observed brightness.

Extinction varies considerably with wavelength, as different physical processes govern absorption and scattering effects in different photon energy regimes. Ryter (1996) has compiled extinction cross sections for the diffuse ISM from the infrared to the X-ray range, as can be seen in Figure 1. The cross section per hydrogen atom spans six orders of magnitude, with a number of distinct features at certain wavelengths.

At a wavelength of approximately 91 nm, the Lyman limit, there is a steep rise in the extinction cross section as this corresponds to the lowest possible energy for photoelectric absorption in a hydrogen atom. For wavelengths longer than the Lyman limit, the cross section generally increases with higher energies, whereas it decreases for shorter wavelengths. This leads to the interesting feature that the cross section is of the same order of magnitude in the near-infrared and the X-ray range. The bump observed at 217.5 nm is believed to originate from carbonaceous material in dust grains, namely graphite or PAHs. Silicate components of dust, however, are responsible for the bump at approximately 10 µm (Draine, 2011a).

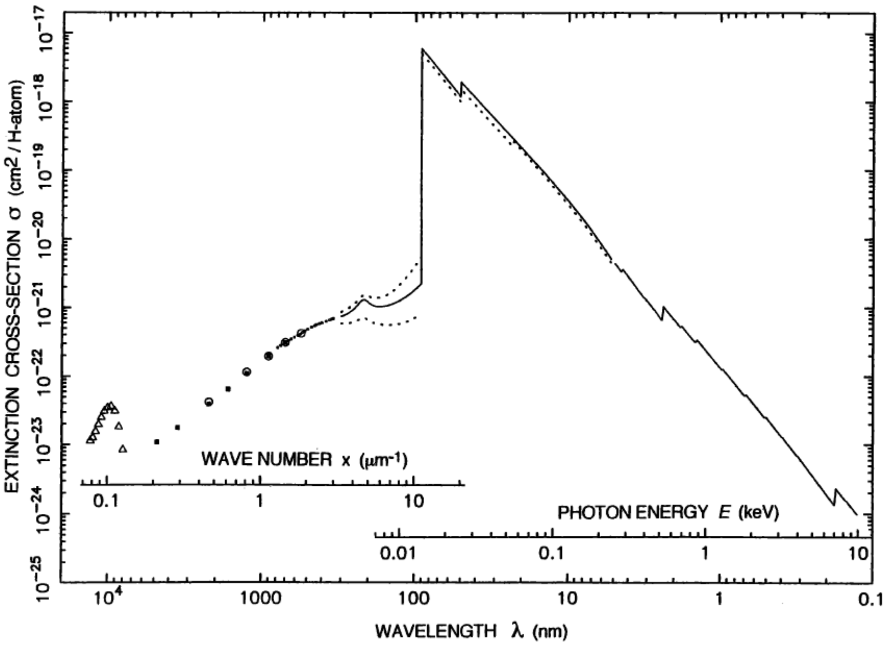

Figure 1: Extinction cross section per hydrogen atom for the diffuse ISM, taken from (Ryter, 1996).

2.3.1 Photoelectric Absorption

In the X-ray range, extinction is dominated by photoelectric absorption. For a single element, the cross section for this process shows steps where the binding energy of electrons in the atom is reached, and decreases with the photon energy E approximately as E^{-3} for energies larger than the absorption limit. Atoms in the atomic, ionised and molecular phase as well as atoms bound in dust grains contribute equally to the extinction cross section as photoelectric absorption is independent of the physical and chemical state of the element. However, large dust grains can become optically thick for X-ray radiation and only material on the surface of the grain adds to the extinction. This so-called ‘self-shielding’ effect is usually small (Morrison and McCammon, 1983; Wilms et al., 2000), but is accounted for in an absorption model by Wilms et al. (2000).

In order to calculate the total photoelectric absorption cross section, contributions from the individual species are summed taking their abundance in different phases (atomic, ionised, molecular or in grains) into account (e.g., Wilms et al., 2000):

$$\sigma_{ISM} = \sigma_{atomic} + \sigma_{ionised} + \sigma_{molecular} + \sigma_{grains}. \tag{1}$$

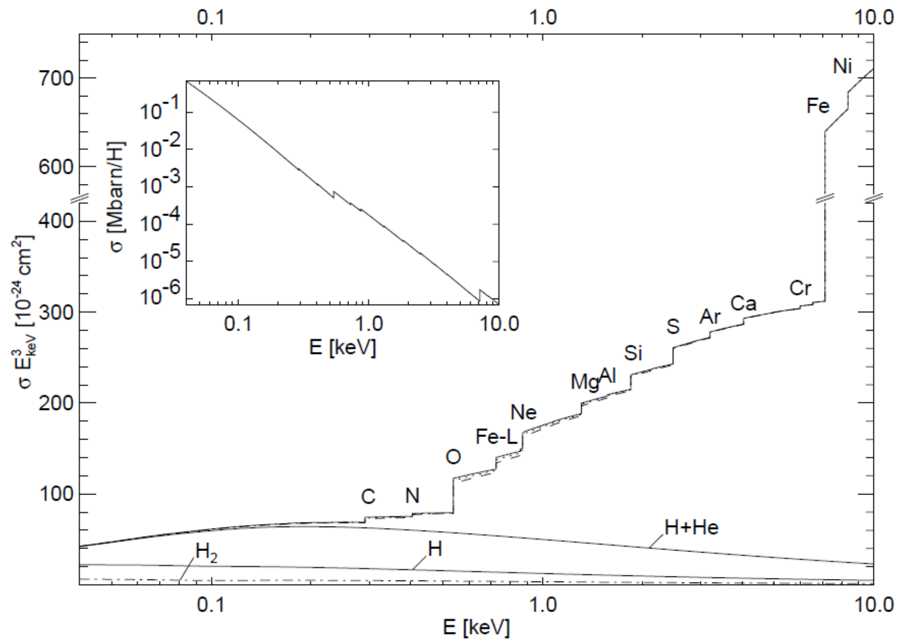

Figure 2: Total photoelectric absorption cross section per hydrogen atom, taken from Wilms et al. (2000).

Species with higher atomic numbers exhibit larger absorption cross sections, which is why not only hydrogen, but also heavier elements such as carbon, nitrogen or oxygen contribute significantly to extinction despite their low abundance, see Figure 2.

The radiative transfer equation for a homogeneous medium with only a background source yields

$$I_{obs}(E) = I_{source}(E)\mathrm{e}^{-\sigma_{ISM}(E)\cdot N_H}, \tag{2}$$

where I_{obs} is the observed intensity, I_{source} is the intensity of the source and N_H is the equivalent hydrogen column density. Therefore, by fitting the observed source spectrum with an assumed intrinsic source spectrum and an absorption term, contributions from the individual elements can be deduced. The equivalent hydrogen column density is then inferred from the assumption of relative element abundances.

The source type determines which intrinsic spectrum is adopted for the fitting of the observed spectrum, as various physical processes can lead to X-ray emission in different types of sources. A number of astrophysical objects emit X-ray radiation, for example stars in a variety of evolutionary stages and mass ranges, extended structures containing hot gas, compact objects, supernovae and galaxies (Trümper and Hasinger, 2008). In this work, X-ray emission from young stars, hot gas and galaxies is studied and therefore these sources are discussed in more detail.

Extended structures of hot gas with temperatures on the order of 10^6 K emit X-ray radiation whose spectrum is dominated by a thermal bremsstrahlung continuum and atomic emission lines rather than 'non-thermal' emission processes such as inverse Compton scattering or synchrotron emission. Several computer codes to model thermal emission by a hot plasma are available, for example the MEKAL code (after Mewe, Kaastra and Liedahl; Kaastra and Mewe, 1993) and APEC (Astrophysical Plasma Emission Code; Smith et al., 2001), which includes data on more atomic lines (> 1 million) than earlier models. Besides atomic data, the models are primarily characterised by the plasma temperature and density.

Since stellar coronae consist of hot, ionised gas, these two codes are also suitable for modelling the spectra of stars. However, the outer part of stellar atmospheres generally exhibits a temperature distribution rather than a single plasma temperature. This can partly be accounted for by using several components with different temperatures simultaneously during the fitting process. In the case of young, magnetically active stars, which are studied in this work, another complication arises: Both the MEKAL code and APEC assume an elemental abundance distribution proportional to solar elemental abundances, which may not be the accurate for these stars (Audard et al., 2003; Getman et al., 2005).

The X-ray spectrum of a galaxy can be approximated by a power-law function and results from the combination of the X-ray emission from all components of the galaxy. X-ray sources within a galaxy include hot interstellar gas, X-ray binaries, supernovae, supernova remnants and O-stars (Fabbiano, 2006; Lehmer et al., 2010). Active galaxies, however, exhibit spectra that are dominated by their central object, a supermassive black hole. The spectral shape of these active galactic nuclei (AGN) can also be approximated by a power-law, but additionally shows several emission lines. A physical process that produces a power-law X-ray spectrum and is therefore a possible cause for the observed radiation in this energy range is inverse Compton scattering of ultraviolet photons off a population of hot electrons (Lightman and Rybicki, 1979). The origin of both the ultraviolet photons and the hot electrons is believed to be connected to an accretion disc around the black hole.

2.3.2 Extinction by Dust Grains

From the infrared to the ultraviolet range, the absorption of radiation by dust grains and the scattering of radiation off dust grains is the dominant process leading to extinction. In astronomy, the attenuation of radiation by dust grains is commonly described by the extinction A_λ (in magnitudes) at the wavelength λ and is defined as

$$A_\lambda = 2.5 \cdot \log\left(\frac{{F_\lambda}^0}{F_\lambda}\right), \tag{3}$$

where ${F_\lambda}^0$ is the flux unaffected by dust and F_λ is the observed flux. The extinction of a source can be determined by a magnitude comparison with another source of the same spectral type and luminosity class that is not affected by extinction.

The change of A_λ with wavelength is referred to as the ‘extinction law’. Its shape has been determined observationally and is strongly dependent on dust properties that are generally not well-known, for example the grain size distribution, the shape of the grains or their composition. Although the extinction law varies depending on the line of sight, Cardelli et al. (1989) have derived a mean extinction law for wavelengths between 0.125

and 3.5 µm that is capable of describing extinction for both the diffuse and the dense ISM with one parameter, namely R_V. This parameter is defined as

$$R_V = \frac{A_V}{E_{B-V}} = \frac{A_V}{A_B - A_V}, \tag{4}$$

where A_V and A_B are the extinction in the V and B photometric band, respectively, and E_{B-V} is the standard colour excess. In the diffuse ISM, the extinction law has approximately the same shape in all directions of the sky with a value of 3.1 for R_V. Substantial variations occur in the shape of the extinction law for different regions of the dense ISM, where higher values for R_V have been deduced, for example $R_V = 5.5$ for θ^1 Orionis C (e.g., Mathis and Wallenhorst, 1981).

The extinction law as deduced by Cardelli et al. (1989) is shown in Figure 3 for different values of R_V. In the optical and ultraviolet range, the shape of the extinction law varies considerably if different values of R_V are adopted. This is not the case in the infrared range, where only minor differences can be observed.

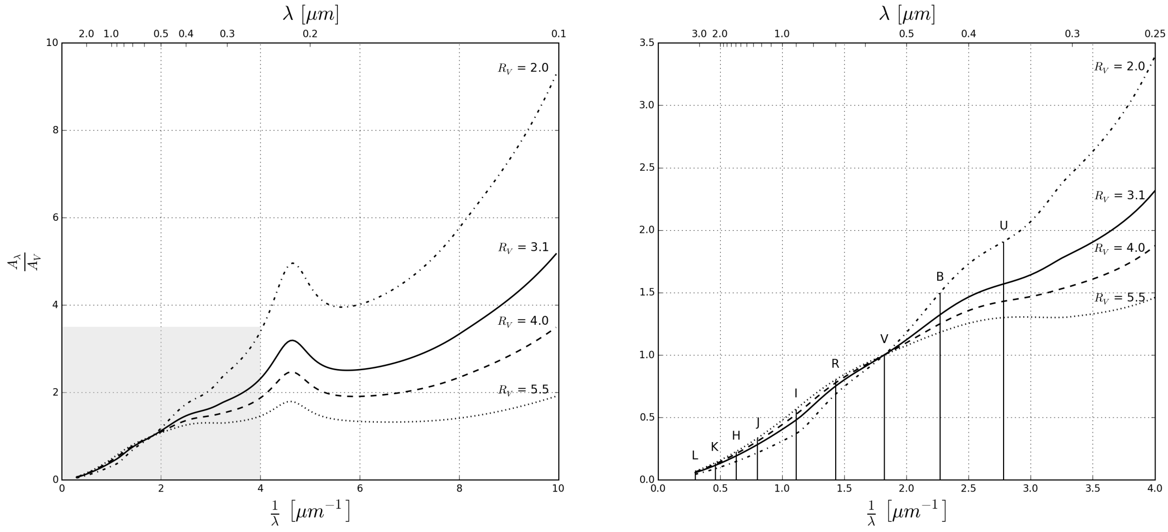

Figure 3: Extinction law as given by Cardelli et al. (1989) for four different values of R_V. *Left:* Extinction law for wave numbers up to 10 µm^{-1}. The area covered in the right plot is indicated by grey shading. *Right:* Extinction law for wave numbers up to 4 µm^{-1}. Vertical lines mark the central wavelengths of several photometric bands.

Assuming a value for R_V and thus defining the relevant extinction law allows for the calculation of A_λ from observations of source colours. Astronomers refer to the magnitude difference in two photometric bands as the ‘colour’ of the observed source, for example $(J - H)$, where J and H are the magnitude in the J and H band, respectively. The Near-Infrared Color Excess (NICE) technique has been developed to calculate extinction values using this concept and to construct extinction maps from the data (Lada et al., 1994). The method has been revised and optimised (Near-Infrared Color Excess

Revisited, NICER) to enable the use of multiple source colours, for example $(J - H)$ and $(H - K)$ (Lombardi and Alves, 2001).

2.3.3 Thermal Emission from Dust Grains

Besides extinction by dust grains, their thermal emission can be used to observe the ISM in the infrared range, as dust is primarily heated by starlight and cools by radiating energy in the infrared. Due to the low temperature of interstellar dust in molecular clouds on the order of 15 K, its blackbody radiation peaks in the sub-millimetre or infrared range. For a single dust grain, the radiated energy can thus be described by a Planck function which is dependent on the temperature of the grain. Modelling the infrared emission of dust requires detailed knowledge about grain properties, as, for example, the grain temperature varies with their size (e.g., Draine, 2011a; Ferrière, 2001). In order to describe thermal radiation produced by a population of dust grains, a modified blackbody model can be used (Klessen and Glover, 2014; Planck Collaboration et al., 2014),

$$I_\nu = \tau_\nu B_\nu \left(T\right), \tag{5}$$

$$I_\nu = \tau_{\nu_0} B_\nu \left(T_{obs}\right) \left(\frac{\nu}{\nu_0}\right)^{\beta_{obs}}, \tag{6}$$

where I_ν is the specific intensity, τ_ν the optical depth, B_ν the Planck function and T the dust temperature. Assumptions on the frequency dependency of τ_ν have been employed to give a relation that depends on a reference frequency ν_0 and a spectral index β_{obs}. For a given reference frequency, fitting an observed intensity spectrum thus yields values for the parameters τ_{ν_0}, T_{obs} and β_{obs}. The actual intensity distribution may follow a more complex relation than Equation 6, because the frequency dependency of the optical depth changes with varying dust properties.

3 Telescopes and Data Sets

In the following, the data used in this work will be presented. An overview will be given in tabular form (see Table 2) before each data set and the corresponding telescope are described.

Telescope	Spectral range	Spectral resolution	Angular resolution	Field of view	Years of operation
ROSAT PSPC[a]	0.1 – 2.4 keV	$\sim 1 - 2.4$	$\sim 1.8'$ [k]	$\sim 2^\circ$	1990 – 1999
XMM-*Newton* EPIC[b]	0.15 – 15 keV	$\sim 20 - 50$	$6.6''$	$30'$	since 1999
Chandra ACIS[c]	0.08 – 10 keV	$\sim 20 - 50$	$0.5''$	$17' \times 17'$	since 1999
Planck HFI[d]	100 – 857 GHz	~ 3	$5 - 10'$	$\sim 8^\circ$	2009 – 2013
Herschel PACS[e] SPIRE[f]	 60 – 210 µm 250 – 500 µm	 ~ 3 ~ 3	 $5 - 16''$ $18 - 36''$	 $1.75 \times 3.5'$ $4 \times 8'$	 2009 – 2013
VISTA VIRCAM[g]	0.8 – 2.3 µm	Z, Y, J, H, K_s	$\sim 0.5''$	1.65°	since 2009
2MASS FLWO[h] CTIO[h]	0.8 – 2.5 µm	J, H, K_s	$\sim 2.5''$	$8.5 \times 8.5'$	1997 – 2001
SDSS Camera[i] BOSS[j]	 3 000 – 10 500 Å 3 600 – 10 400 Å	 u, g, r, i, z $\sim 1\,560 - 2\,650$	 $1.3''$ [l] $2''$ [m]	 3°	 since 1998

Table 2: List of telescopes and data sets used in this work. *Column 1:* The telescope name and the relevant telescope instrument are given. The references used in this table are listed in the footnotes on the following page. *Column 3:* Either the numerical spectral resolution or the names of the spectral bands covered by the instrument are tabulated. *Column 4:* Unless otherwise stated, the angular resolution values represent the full-width half-maximum (FWHM) of the point-spread function (PSF). *Column 5:* Single angular values represent the diameter of the field of view area, otherwise the length and width of a rectangular field of view are given.

Since both ROSAT and *Planck* data cover the entire sky, these data sets are chosen to study the diffuse interstellar medium on large scales (see Section 4.1). X-ray emitting and absorbing structures are mapped by ROSAT with high sensitivity in the soft X-ray range while *Planck* provides information on thermal dust emission in the microwave regime. In the next part, point source spectra recorded by XMM-*Newton* are used to gain information on X-ray absorption (see Section 4.2) by the diffuse ISM. While XMM-*Newton* is not an all-sky survey, it has observed a large number of sources and given rise to several valuable catalogues. The Sloan Digital Sky Survey is employed for source classification due to its immense number of consistently classified objects. Similarly, the 2MASS catalogue comprises near-infrared magnitudes for sources across the entire sky which are used as a measure for dust extinction. The Orion Nebula Cluster is the region of interest in the last part of the data analysis which studies the dense ISM (see Section 4.3). Data sets with high angular resolution are required to resolve the small-scale structures of dense clouds and characterise the associated closely spaced stars. Therefore, source parameters deduced from *Chandra* observations in the X-ray range are used along with *Planck* and *Herschel* data in the sub-millimetre regime and near-infrared magnitudes from VISTA.

3.1 ROSAT

The Röntgensatellit (ROSAT) was capable of detecting point sources and diffuse emission in the soft X-ray range with high sensitivity. It comprised two Position Sensitive Proportional Counters (PSPC) and the High Resolution Imager (HRI) in the focal plane of the X-ray Telescope (XRT) as well as the Wide-Field Camera (WFC) that operated in the extreme ultraviolet. The mission was divided into two phases: In the first phase, which lasted for six months, the satellite scanned the entire sky and produced an all-sky

---

[a] Snowden et al. (1994, 1997); HEASARC: ROSAT X-ray Astronomy Data - Guest Observer Facility, URL `https://heasarc.gsfc.nasa.gov/docs/rosat/rosgof.html` (accessed March 2015)

[b] Jansen et al. (2001); XMM-Newton: A Technical Description, URL `http://xmm.esac.esa.int/external/xmm_user_support/documentation/technical/` (accessed March 2015)

[c] Garmire et al. (2003); Weisskopf et al. (2002); Chandra X-ray Observatory, URL `https://heasarc.gsfc.nasa.gov/docs/chandra/chandra.html` (accessed March 2015)

[d] Planck Collaboration (2006); Tauber et al. (2004)

[e] Pilbratt et al. (2010); PACS Observer's Manual (from July 2013)

[f] Pilbratt et al. (2010); The Spectral and Photometric Imaging Receiver (SPIRE) Handbook (from March 2014)

[g] Sutherland et al. (2015); ESO - VIRCAM @ VISTA, URL `http://www.eso.org/sci/facilities/paranal/instruments/vircam.html` (accessed April 2015)

[h] Skrutskie et al. (2006); The Two Micron All Sky Survey (2MASS) at IPAC, URL `http://www.ipac.caltech.edu/2mass/` (accessed April 2015)

[i] Gunn et al. (2006); SDSS-III DR12, URL `http://www.sdss.org/` (accessed April 2015); The Scope of DR9 - SDSS-III, URL `https://www.sdss3.org/dr9/scope.php` (accessed April 2015)

[j] SDSS-III DR12, URL `http://www.sdss.org/` (accessed April 2015)

[k] 50 % encircled energy

[l] PSF FWHM in the r spectral band

[m] fibre diameter

survey with the PSPCs and the WFC. In the second phase, selected sources were examined in pointed observations. Only X-ray data from the all-sky survey are used in this work, specifically the soft X-ray background maps produced by Snowden et al. (1997).

Due to the low energy resolution of the PSPCs, spectral information is obtained by using seven bands as listed in Table 3 (Snowden et al., 1997). The upper energy limits for R1 and R2 are identical as they are restricted by the absorption edge of carbon which is contained in the PSPC entrance window. For a similar reason, the R3 band is usually not considered: Its response curve shows a minimum at the carbon absorption edge and contributions on both sides of the minimum, making count rates in this band hard to interpret (Snowden et al., 1994).

Band name	Energy range [keV]
R1	0.11 – 0.284
R2	0.14 – 0.284
R3	0.20 – 0.83
R4	0.44 – 1.01
R5	0.56 – 1.21
R6	0.73 – 1.56
R7	1.05 – 2.04

Table 3: ROSAT energy bands, taken from Snowden et al. (1994).

During data reduction, $1.6' \times 1.6'$ pixels were used that oversample the point response averaged over the complete all-sky survey ($\sim 1.8'$; Snowden et al., 1997). In order to improve the statistical significance, a binning in pixels of $12' \times 12'$ is applied for the final maps. The final product is available in the form of six projections centred at the galactic poles, which correspond to (0°, 90°) and (0°, -90°), and four positions along the galactic plane, namely (0°, 0°), (90°, 0°), (180°, 0°) and (270°, 0°). Here, coordinates are given as galactic coordinates (l, b), where l is the galactic longitude and b the galactic latitude. Figure 4 shows a projection of the all-sky data with the photon energy indicated by different colours.

Clearly, the three energy ranges defined for this presentation of the ROSAT data show very different morphologies. While the intensity for high energies (blue in Figure 4) is concentrated in the galactic plane and makes numerous point sources visible, the medium and low-energy count-rates (red and green) appear to trace more diffuse components off the galactic plane. An interesting feature examined in this work is the fact that several large-scale structures are evident in the lower energy bands which can be associated with foreground material, as soft X-rays have a relatively short mean free path length ($\sim$ 65 pc; Snowden et al., 1997). By correlating ROSAT data with measures of dust emission or extinction, the medium forming these structures can be analysed. Since the sensitivity of ROSAT for soft X-rays is higher than that of XMM-*Newton* or *Chandra*, it provides an ideal data set for this study.

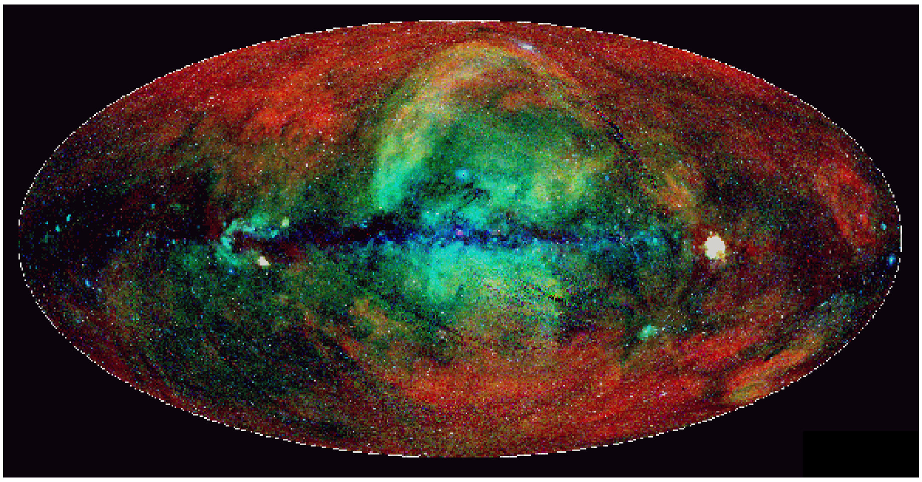

Figure 4: ROSAT all-sky survey data as a three-colour image. *Red:* 0.1 – 0.4 keV. *Green:* 0.5 – 0.9 keV. *Blue:* 0.9 – 2.0 keV. Taken from Freyberg and Egger (1999).

3.2 XMM-*Newton*

The X-ray Multi-Mirror (XMM) mission is an ESA satellite equipped with three X-ray CCD cameras which are collectively referred to as the European Photon Imaging Camera (EPIC). One camera uses pn CCDs whereas the other two are designed as MOS (Metal-Oxide Semiconductor) CCD arrays. For the MOS cameras, approximately half of the light in the X-ray beam is diverted to the Reflection Grating Spectrometers (RGS) which provide a higher spectral resolution of $\sim 100 - 500$ in the soft X-ray range (den Herder et al., 2001). This work makes use of two catalogues based on XMM-*Newton* imaging spectroscopy data.

XMM-*Newton* Spectral-Fit Database

The XMM-*Newton* spectral-fit database (XMMFITCAT) is built from the latest release of the XMM-*Newton* Serendipitous Source Catalogue (3XMM-DR4) which lists sources detected by EPIC between 2000 and 2012[n]. In total, more than 370 000 unique sources and 794 square degrees of sky area (or 2 % of the total sky) have been observed. The spectral-fit database aims at providing best-fit parameters of fits applied to source spectra obtained by XMM-*Newton* using different models (Corral et al., 2014). For each observation, source detections are filtered by the number of recorded counts and the extracted source spectrum is then fitted with a maximum of six spectral models. For this work, only the absorbed power-law model is relevant which uses photoelectric absorption cross-sections by Morrison and McCammon (1983) and relative element abundances as given by Anders and Ebihara (1982). The fit parameters in this model are the column density of the absorption component, the photon index of the power-law component and

---

[n] XMM Catalogue Public Pages, URL `http://xmmssc-www.star.le.ac.uk/Catalogue/xcat_public_3XMM-DR4.html` (accessed March 2015).

the normalisation of the total spectrum. If spectra from multiple CCDs are available, the fit is performed simultaneously for all spectra. The final catalogue consists of entries for more than 114 000 observations corresponding to almost 78 000 unique sources, giving (among other data) the best-fit parameters for each fitted model along with their errors, the reduced χ^2 value and a spectral fitting flag indicating problems that occurred during the automated fitting procedure.

X-ray Survey of YSOs in Orion A

In the X-ray Survey of YSOs in Orion A catalogue (Pillitteri et al., 2013), which will also be referred to as the 'Pillitteri catalogue' in the following, best-fit parameters for 464 source spectra observed by XMM-*Newton* are listed along with infrared data obtained by a match with the Spitzer survey by Megeath et al. (2012). Ten different XMM-*Newton* fields in the Orion A cloud and three fields in the ONC region are the basis for this catalogue. After several data reduction and source extraction steps, the spectra are fitted with one or two components of a plasma emission model (APEC; Smith et al., 2001) and an absorption term. Similar to the XMM-*Newton* spectral-fit catalogue, the best-fit parameters, their errors and the reduced χ^2 value of the model are provided in the final catalogue.

3.3 *Chandra*

The *Chandra* X-ray Observatory (*Chandra*) is equipped with four pairs of iridium-coated mirrors that focus incoming X-rays onto the High Resolution Camera (HRC) and the Advanced CCD Imaging Spectrometer (ACIS). Transmission gratings can be positioned behind the mirrors to allow for high-resolution X-ray spectroscopy. The HRC uses two Micro-Channel Plates as detectors, whereas ACIS consists of an array of ten CCDs with each pixel covering approximately $0.5''$ of the sky (Garmire et al., 2003; Weisskopf et al., 2002).

Based on ACIS observations from January 2003 with a total exposure time of almost ten days, the *Chandra* Orion Ultradeep Project (COUP) provides X-ray data on more than 1 600 sources in the Orion Nebula Cluster (ONC; Getman et al., 2005). Two different source detection algorithms were used in combination to give the final source list, which is the basis for the subsequent spectrum extraction and spectral analysis. The fitted spectral model comprises one or two components of thermal plasma emission (MEKAL; Kaastra and Mewe, 1993) and an absorption component which is calculated using cross-sections by Morrison and McCammon (1983) and element abundances by Anders and Ebihara (1982). In the catalogue, the best-fit parameters for plasma temperatures and the absorbing hydrogen column density are given along with their errors, as well as a χ^2 value, a model flag with information on the components of the fitted model and a spectral fit flag indicating spectral features and fitting problems. Additionally, a match with several infrared catalogues was performed, including data obtained by the Very Large Telescope (VLT) instrument ISAAC (Infrared Spectrometer and Array

Camera) and 2MASS (see Section 3.7). The thus found magnitude values for the J, H and K_s band are provided in the COUP catalogue.

3.4 *Planck*

Designed to measure temperature variations in the cosmic microwave background (CMB), the *Planck* satellite mapped microwave radiation over the whole sky using its Low Frequency Instrument (LFI) and High Frequency Instrument (HFI; Planck Collaboration, 2006). In order to extract the CMB from the *Planck* maps, it is necessary to subtract several foreground components, for example extragalactic sources, synchrotron emission or emission from interstellar dust. Therefore, foreground maps are constructed which are then used to deduce the CMB emission while also containing valuable information on the nature of the foreground components. The dust emission map derived from three *Planck* HFI bands (353 GHz, 545 GHz and 857 GHz) along with IRAS and DIRBE data at 3 000 GHz (Planck Collaboration et al., 2014) is used in this work. By fitting the spectral energy distribution (SED) of the dust emission with a modified blackbody spectrum according to Equation 6 in Section 2.3.3 at a spatial resolution of $5'$, the optical depth τ_{ν_0}, the dust temperature T_{obs} and the spectral index β_{obs} are deduced. The reference frequency ν_0 was chosen to be 353 GHz. The final dust emission products in the *Planck* Public Data Release 1 from 2013 include maps of τ_{353}, T_{obs} and β_{obs} with their errors, and a radiance map calculated from the three fitting parameters. Figure 5 shows the *Planck* all-sky map of τ_{353}.

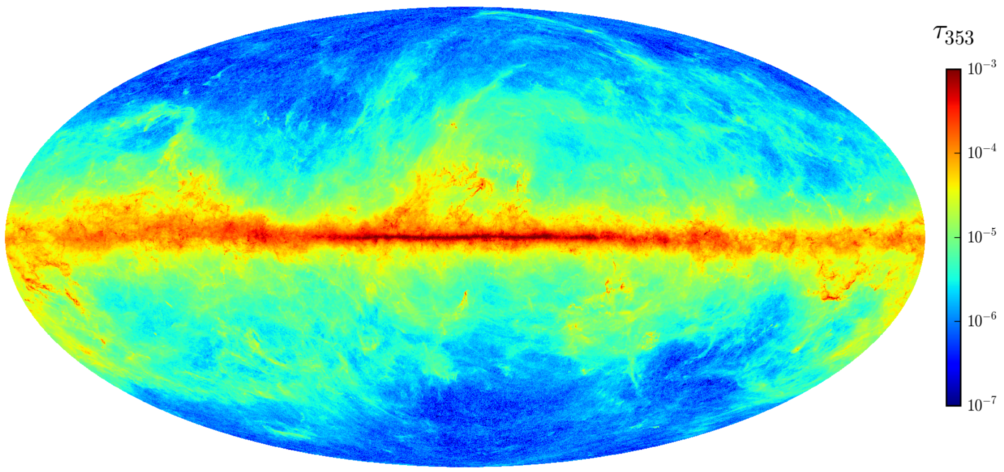

Figure 5: Map of the optical depth at a frequency of 353 GHz, τ_{353}, based on data obtained by the *Planck* satellite.

3.5 *Herschel*

The *Herschel* Space Observatory (*Herschel*) operated in the far-infrared range and carried three instruments: the Heterodyne Instrument for the Far-Infrared (HIFI), the Photodetecting Array Camera and Spectrometer (PACS) and the Spectral and Photometric Imaging Receiver (SPIRE; Pilbratt et al., 2010). With a spectral resolving power of $\sim 10^6$, HIFI was capable of recording single-pixel spectra in two wavelength bands (157 – 212 µm and 240 – 625 µm). PACS and SPIRE used bolometer and photoconductor arrays as detectors and could both be operated as either photometers or spectrometers[o,p].

For the data set used in this work, PACS and SPIRE were used simultaneously in the photometric scan mode to map the molecular clouds Orion A and B. Lombardi et al. (2014) have combined *Planck* and *Herschel* dust emission maps and near-infrared extinction data from 2MASS (see Section 3.7) to create an optical depth map of the Orion A and B clouds and derive a conversion factor between τ_{353} and the extinction in the K band A_K.

3.6 VISTA

With its 4.1 m silver-coated primary mirror, the Visible and Infrared Survey Telescope for Astronomy (VISTA) is the largest infrared telescope ever built. It is equipped with one instrument, the VISTA Infrared Camera (VIRCAM), which comprises a detector with 67 million pixels each of $0.339''$ (on average) in size on the sky[q] (Sutherland et al., 2015). The currently available filters include Z, Y, J, H and $\mathrm{K_s}$ broad band filters.

As part the Vienna Survey in Orion (VISION), an effort to study star formation processes in this region, a VISTA survey of the Orion A cloud has been conducted (Meingast et al., *in prep.*). Magnitudes in the J, H and $\mathrm{K_s}$ bands have been deduced for approximately 800 000 sources and compiled in a catalogue, which will be referred to as the 'VISION catalogue' in the following.

3.7 2MASS

The data for the Two Micron All-Sky Survey (2MASS) were collected between 1997 and 2001 by instruments at the Fred Lawrence Whipple Observatory (FLWO) in Arizona and the Cerro Tololo Inter-American Observatory (CTIO) in Chile[r] (Skrutskie et al., 2006), both equipped with primary mirrors 1.3 m in diameter. The survey covers the entire sky and provides near-infrared data in the form of J, H and $\mathrm{K_s}$-band magnitudes for more than 470 million point sources and 1.6 million extended sources.

---

[o] PACS Observer's Manual (from July 2013)

[p] The Spectral and Photometric Imaging Receiver (SPIRE) Handbook (from March 2014)

[q] ESO - VIRCAM @ VISTA, URL `http://www.eso.org/sci/facilities/paranal/instruments/vircam.html` (accessed April 2015)

[r] The Two Micron All Sky Survey (2MASS) at IPAC, URL `http://www.ipac.caltech.edu/2mass/` (accessed April 2015)

3.8 SDSS

The Sloan Digital Sky Survey (SDSS) is based on observations by the 2.5 m SDSS telescope located in New Mexico (Gunn et al., 2006) which is equipped with several spectrograph instruments and an imaging camera. While the spectrographs cover the near-infrared and optical range and are capable of recording high-resolution spectra for multiple sources simultaneously, the imaging camera uses 30 $2\,024 \times 2\,024$ pixel CCDs to measure source magnitudes in five spectral bands. The central wavelength for each spectral band is given in Table 4.

Band name	Central wavelength[s]
u	3 551 Å
g	4 686 Å
r	6 166 Å
i	7 480 Å
z	8 932 Å

Table 4: SDSS spectral bands.

Seven major surveys have been completed in the first three generations of the SDSS from 2000 until 2014, mapping large parts of the northern sky, monitoring supernovae and providing insights on the dynamics of the Milky Way, the clustering of galaxies and exoplanet populations: the SDSS legacy survey, the SDSS supernova survey, the Sloan Extension for Galactic Understanding and Exploration (SEGUE-1 and SEGUE-2), the Apache Point Observatory Galactic Evolution Experiment (APOGEE), the Baryon Oscillation Spectroscopic Survey (BOSS) and the Multi-Object APO Radial Velocity Exoplanet Large-area Survey (MARVELS). In the current fourth generation of the SDSS (2014 – 2018), the following three surveys will extend the available data: the APO Galaxy Evolution Experiment North and South (APOGEE-2), the Extended Baryon Oscillation Spectroscopic Survey (eBOSS) and Mapping Nearby Galaxies at APO (MaNGA).

The latest data release available in VizieR[t] (data release 9) covers more than 14 500 square degrees of sky area (or 35 % of the total sky) and lists 469 million unique objects[u] (Ahn et al., 2012). Approximately 2.6 million catalogue entries have been recorded with useful spectra which can be used for source classification by comparison with template spectra of each source type. This way, 1.4 million sources have been classified as galaxies, 670 000 as stars and 230 000 as quasars. This work puts to use the source classification based on BOSS spectra and the optical band magnitudes measured by the imaging camera.

---

[s] SDSS-III DR12, URL `http://www.sdss.org/` (accessed April 2015)

[t] The VizieR Service for Astronomical Catalogues (CDS, Strasbourg, France), URL `http://vizier.u-strasbg.fr` (accessed April 2015)

[u] The Scope of DR9 - SDSS-III, URL `https://www.sdss3.org/dr9/scope.php` (accessed April 2015)

4 Data Analysis

4.1 Extended Emission and Absorption by the Diffuse ISM

4.1.1 Background and Motivation

The ROSAT soft X-ray maps provide information on the X-ray background across the entire sky for photon energies between 0.11 and 2.04 keV (see Section 3.1). As discussed in Section 2.3.1, the intensity of X-ray radiation is attenuated by photoelectric absorption processes as it permeates the interstellar medium. Thus, the properties of the ISM in the foreground are imprinted on the soft X-ray background radiation. Similarly, the sub-millimetre emission measured by the *Planck* satellite (see Section 3.4) can be separated into various components, one of them being thermal emission by dust grains (see Section 2.3.3). Since both X-ray absorption and microwave emission are caused by constituents of the ISM, an anti-correlation between the observed X-ray intensity and the dust optical depth would be expected if both X-ray absorption and sub-millimetre emission are caused the same medium.

Generally, the relation between the source intensity, the properties of the emitting and absorbing medium and the observed intensity is described by the radiative transfer equation. For a homogeneous medium, it can be written as

$$I_\nu = {I_\nu}^0 \mathrm{e}^{-\tau_\nu} + S_\nu \left(1 - \mathrm{e}^{-\tau_\nu}\right) , \tag{7}$$

where I_ν is the observed specific intensity at the frequency ν, ${I_\nu}^0$ is the source intensity, τ_ν the optical depth and S_ν the source function. Using the definition $S_\nu = \frac{j_\nu}{\kappa_\nu}$, the source function can be expressed in terms of the emission coefficient j_ν and absorption coefficient κ_ν. If the optical depth is small ($\tau_\nu \ll 1$) and no emitting medium is present ($S_\nu = 0$, cf. Equation 2), the radiative transfer equation can be simplified to

$$I_\nu = {I_\nu}^0 \left(1 - \tau_\nu\right) . \tag{8}$$

While this equation specifies the relation between the observed X-ray intensity and the optical depth, the soft X-ray background (SXRB) is believed to originate from a number of sources at different distances to the Sun, leading to a more complex situation which will be discussed in the following.

After the discovery of the SXRB in the late 1960s (Bowyer et al., 1968) an anti-correlation with the galactic neutral hydrogen column density was found, which lead to the conclusion that the origin of the observed X-ray radiation is extragalactic or located in the galactic halo. However, global models assuming a smoothly varying background emission failed to explain the available data (McCammon et al., 1983) and the idea of the Sun being located within the Local Hot Bubble (LHB) was created (Snowden et al., 1990). The LHB is a region of irregular shape filled with low-density, hot gas that emits X-rays. Including the LHB resulted in SXRB models that were in good agreement with the data. With the angular resolution of the ROSAT satellite, a wealth of detailed structure in the SXRB was discovered in the softest ROSAT bands that could not be explained by previous models (Snowden et al., 1995). In particular, the soft X-ray emission believed to originate from the LHB and the galactic halo appears to vary considerably across the sky, complicating the overall picture of the SXRB. Several components have been identified (Kuntz and Snowden, 2000; Trümper and Hasinger, 2008), including

- unresolved extragalactic point sources (e.g., AGN) composing a uniform extragalactic background,
- diffuse distant galactic emission from the galactic halo,
- diffuse local emission from the Local Hot Bubble, and
- very local emission from solar-wind charge-exchange processes.

Disentangling the origin of the observed X-ray radiation requires some knowledge on the structures and objects along the line of sight gained from data in other wavelength ranges or better spectral resolution than is possible for ROSAT observations to permit reliable modelling and fitting of various SXRB components. The second method relies on the fact that softer X-ray radiation originates locally while harder radiation has long mean free path lengths due to the energy dependency of the photoelectric absorption cross section (see Sections 2.3.1 and 3.1). Another possible approach are so-called 'shadowing studies' that examine the correlation between hydrogen column density and SXRB intensity for large-scale structures within the Galaxy mainly consisting of neutral hydrogen (e.g., Snowden et al., 2000). These objects commonly appear as dark 'shadows' in soft X-ray observations such as the R1 and R2 bands in the ROSAT all-sky maps, as can be seen in Figure 4. Background and foreground contributions to the observed X-ray intensity can be deduced in this way, and if the distance to the shadowing object is known, a statement on the distribution of X-ray emitting and absorbing material along the line of sight can be made.

Separating the various components of the SXRB has proven to be a difficult undertaking (e.g., Kuntz and Snowden, 2000), in part because of observational constraints, but also because of the limited knowledge on the 3-dimensional structure of the interstellar medium. The contributions from different constituents of the SXRB have been shown to vary across the sky, and additionally the properties of these constituents change depending on the line of sight (Kuntz and Snowden, 2000; Snowden et al., 2000). Nevertheless, shadowing studies toward selected objects have provided valuable insights on the nature of the SXRB (e.g., Burrows and Mendenhall, 1991).

Although the origin of the soft X-ray radiation observed by ROSAT is generally not clear, a study of the relation with the dust optical depth can still be employed to make statements on the connection between absorption by the interstellar medium and dust emission. With thermal dust and soft X-ray emission data available for the entire sky, this is now possible for any line of sight.

4.1.2 Map Preparation

The correlation between the X-ray intensity measured by ROSAT and the dust optical depth deduced from *Planck* data will be based on a pixel-by-pixel comparison of the two data sets. Since the available ROSAT and *Planck* data are stored in different map formats and projections and have different resolutions, a number of preparatory steps need to be taken before the analysis.

As mentioned in Section 3.1, the soft X-ray maps produced by Snowden et al. (1997) are not available as a single all-sky map similar to *Planck*, but as six partly overlapping projections. In order to avoid data loss in the ROSAT maps, they are not reprojected to create an all-sky map. Instead, the *Planck* data are smoothed and reprojected to give maps with the same resolution and pixel size as the X-ray maps. The necessary steps, which are discussed in more detail in the following, can be summarised as

1. Region extraction from *Planck* maps,
2. Smoothing of the extracted maps,
3. Reprojection of the smoothed maps, and
4. Cropping of the ROSAT maps to the size of the reprojected *Planck* maps.

The *Planck* maps are stored in a data cube consisting of several layers, each presenting an all-sky map of a dust emission model parameter in the HEALPix (Górski et al., 2005) format. As the HEALPix pixelation scheme is not directly compatible with the ROSAT maps, twelve regions are chosen and extracted using the healpix2tan[v] tool which generates local tangent plane projections of HEALPix maps for a given central position, pixel size and extraction region size. The pixel size is chosen as $1'$ and the region size as 2048×2048 (pixel)^2, corresponding to approximately $30^\circ \times 30^\circ$, for all twelve regions. Table 5 lists the selected regions with their central positions in galactic coordinates. The regions are chosen with the criterion of covering a range of possible configurations in both the ROSAT and *Planck* maps. For example, several regions show a large dynamic range in both the X-ray count rates in the lower ROSAT bands and the τ_{353} map from *Planck* (e.g., Region 03, Region 05). Regions close to the galactic centre (Region pipe and Region sofue14) on the other hand exhibit very little contrast in ROSAT data while the dust optical depth assumes a large range of values. This way, a significant part of the possible (non-)correlations between the X-ray intensity and the dust optical depth can be studied while avoiding the need to analyse the maps in their entirety.

As a next step, the extracted *Planck* maps are smoothed to the resolution of the ROSAT maps, namely $12'$, using a Gaussian kernel. The FWHM of the kernel, $FWHM_k$, can be calculated as

$$FWHM_k = \sqrt{FWHM_R^2 - FWHM_P^2}, \tag{9}$$

where $FWHM_R$ and $FWHM_P$ are the FWHM of the ROSAT and *Planck* point-spread functions, respectively. This equation is based the assumption that the PSF of both telescopes can be approximated by a Gaussian function and on the fact that the convolution of two Gaussian functions again results in a Gaussian function. Assuming

---

[v] Planck Software and Analysis Products, URL `http://irsa.ipac.caltech.edu/data/Planck/release_1/software/` (accessed April 2015)

Region name	Centre	
	l	b
Region 01	40°	33°
Region 02	250°	-30°
Region 03	217°	-27°
Region 04	188°	10°
Region 05	129°	33°
Region 06	344°	67°
Region cra	4°	-24°
Region g225	226°	-66°
Region pipe	0°	5°
Region pol	0°	90°
Region sofue14	0°	0°
Region sofue14b	20°	30°

Table 5: Names and central coordinates of the regions selected for the comparison between ROSAT and *Planck* data. Coordinates are given as galactic coordinates.

$FWHM_R = 12'$ and $FWHM_P = 4.4'$, the FWHM of the Gaussian function needed to smooth the *Planck* maps accordingly is $\sim 11.2'$. The final *Planck* maps are then produced by a reprojection which ensures that the astrometry and pixel sizes in the *Planck* and ROSAT data are equal. For this task, the Python package Montage[w] is employed. This piece of software uses the astrometry information given in the FITS file header to reproject images while preserving the mapped flux. Finally, the ROSAT maps are cropped to the same size as the reprojected *Planck* maps.

The X-ray intensity is given in the native units of the ROSAT all-sky maps, $\frac{10^{-6}\text{ counts}}{\text{s}\cdot\text{arcmin}^2}$, throughout the analysis to preserve the original information. Nevertheless, an outline of the necessary steps required to convert the count rate to physical flux values and the involved difficulties will be described in the following. In order to convert the measured intensity to physical flux units, $\frac{\text{erg}}{\text{s}\cdot\text{cm}^2\cdot\text{sr}}$, a division by the energy-dependent instrument effective area and the conversion of every detected photon count to its energy is needed, which is dependent on the exact source spectrum. The available ROSAT maps do not provide information on the energy of individual photons and therefore only average values for each band can be used. The conversion can be written as

$$10^{-6}\left[\frac{\text{counts}}{\text{s}\cdot\text{arcmin}^2}\right] \rightarrow 10^{-6}\left[\frac{\text{counts}}{\text{s}\cdot\text{arcmin}^2}\right]\cdot E_m\left[\frac{\text{keV}}{\text{count}}\right]\cdot 1.6\cdot 10^{-9}\left[\frac{\text{erg}}{\text{keV}}\right]\cdot$$
$$\cdot 1.2\cdot 10^{7}\left[\frac{\text{arcmin}^2}{\text{sr}}\right]\cdot\frac{1}{A_{eff}}\left[\frac{1}{\text{cm}^2}\right],$$

---

[w] Montage - Image Mosaic Software for Astronomers, URL `http://montage.ipac.caltech.edu/index.html` (accessed April 2015)

where E_m is the mean energy and A_{eff} the effective area (Collier et al., 2014). For a mean energy of 0.25 keV and an effective area of 220 cm^2,

$$10^{-6}\left[\frac{\text{counts}}{\text{s}\cdot\text{arcmin}^2}\right] \rightarrow 2.2\cdot 10^{-11}\left[\frac{\text{erg}}{\text{s}\cdot\text{cm}^2\cdot\text{sr}}\right]. \tag{10}$$

Using these relations, the count rates for every energy band can be translated to physical flux values, yielding a measurement of the X-ray flux that can be compared between different energy bands. At this point, however, the analysis does not include physical models which predict flux values or make use of more than one energy band simultaneously. Therefore, the original units are used.

4.1.3 Results and Discussion

As mentioned in Sections 2.3.1 and 4.1.1, the lower ROSAT energy bands are more sensitive to absorbing foreground material and therefore, the analysis focusses on the bands R1 and R2. Due to the almost identical energy ranges of these bands the count rates measured by ROSAT are similar, which is why only plots for the R2 band are shown in this section. Also, the band R3 is not included in this study for the reasons stated in Section 3.1. Graphs for R1 and the higher ROSAT bands can be found in the Appendix.

First, the smoothed and reprojected *Planck* maps are compared to the ROSAT maps visually by overplotting the *Planck* region maps with contours of the measured X-ray count rate, as can be seen in Figure 6 for the R2 band (Figures 30 to 34 for R1 and R4 to R7). In several regions similar morphologies of the X-ray intensity and the dust optical depth can be found, most prominently in Regions 01, 02 and sofue14b. However, this correlation is generally not present throughout the entire region, see, for example, Region 03, where the lower half of the image appears correlated while this is not the case for the upper part. In a small number of regions, no relation between the X-ray and dust morphology can be observed (e.g., Regions 04, g225 and pipe). For higher energy bands, the measured count rates are generally lower except for detections of point sources, and no correlation between the ROSAT and *Planck* data is found.

A more quantitative study of the relation between X-ray intensity and dust optical depth can be conducted via a pixel-by-pixel comparison of the two data sets (see Figure 7 for R2 and Figures 35 to 39 for R1 and R4 to R7). For this analysis, pixels with a signal-to-noise ratio lower than 3 in either the ROSAT or τ_{353} value are not considered.

Similar to the results of the previous study, several regions exhibit a clear negative correlation while others appear to expose no relation between the ROSAT and *Planck* data. The latter applies to regions close to the galactic centre (Region pipe and sofue14), where the X-ray intensity is low and shows little variation while the dust optical depth assumes its highest values and varies considerably. In the direction of the galactic centre, a large amount of interstellar material is located along the line of sight causing the mean free path of soft X-ray radiation to become shorter. Thus, emission from distant sources is not detectable in the lower bands and only radiation of local origin can be traced (Snowden et al., 1997). The thermal dust emission detected by *Planck*, however, is

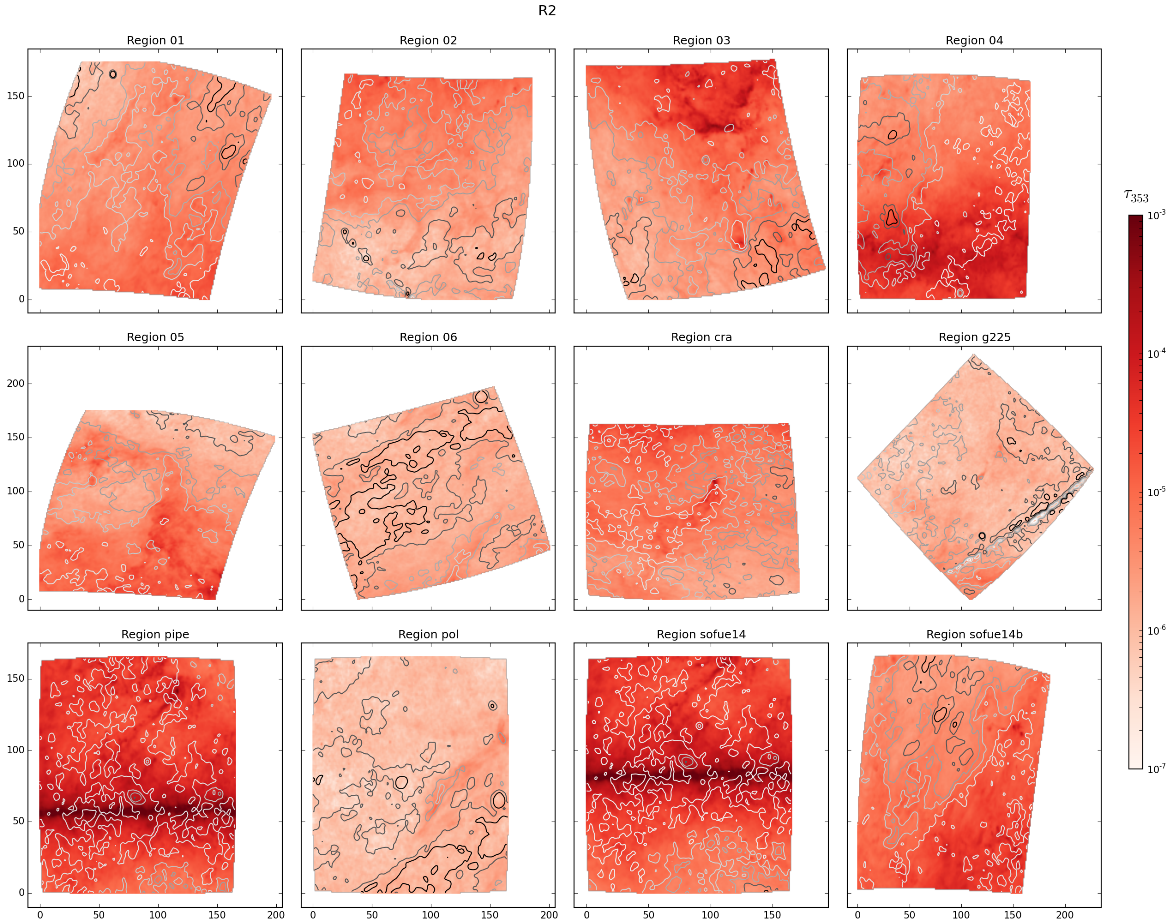

Figure 6: Comparison of X-ray intensity (contours) and dust optical depth (red colour-scale image) in the R2 energy band, where darker colours correspond to higher values. The x and y axis give the position in ROSAT pixels. The contours have been smoothed using a 1.5-σ Gaussian kernel and correspond to (50, 100, 200, 300, 400, 600 and 800) $\cdot 10^{-6}$ $\frac{\text{counts}}{\text{s}\cdot\text{arcmin}^2}$. In Region g225, the stripe of low values almost parallel to the lower right edge of the image is caused by a thin area on the sky without valid ROSAT data.

measured along the entire line of sight. For large values of τ_{353}, the relation between the measurements of the ISM by ROSAT and *Planck* may therefore not be comparable as they trace material at different distances to the observer. This discrepancy is a possible explanation for the observed non-correlation in regions close to the galactic centre.

For the regions which exhibit an obvious correlation, the plots reveal interesting features: The correlation can only be observed at low values of τ_{353}, in agreement with the statement in the previous paragraph. In regions also covering higher optical depths, a kink occurs where the slope of the correlation changes from a negative value to a flat relation. Additionally, the graphs for several regions (e.g., Region 01, 03 and cra) appear to consist of at least two clouds of data points that individually show a systematic

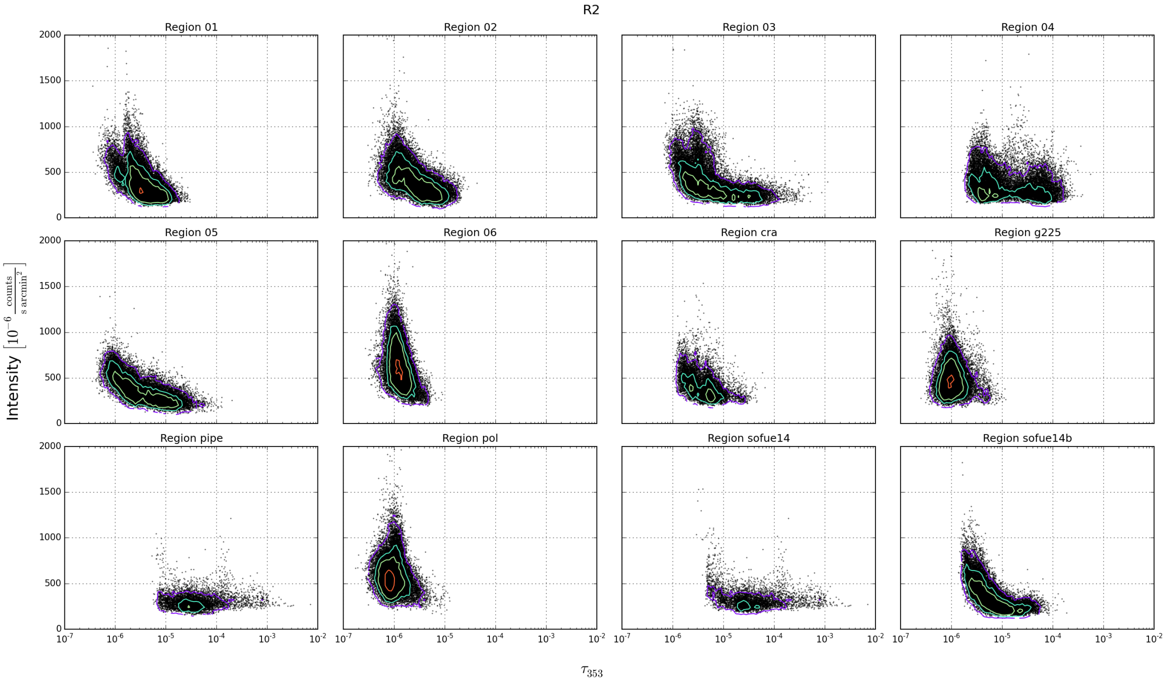

Figure 7: X-ray intensity in the R2 band as a function of dust optical depth. Every data point corresponds to one pixel. Contours of a 2-dimensional histogram are shown to illustrate the data point density. The histogram is calculated using 100 bins in the x and 50 bins in the y axis. The contours correspond to a number of 10, 50, 100 and 300 data points per bin.

behaviour. To investigate the shape of the correlations further, the graphs are displayed with information on the position of the data points within the region. For Regions 01 and 03, these plots are shown in Figures 8 and 9, respectively, while the graphs for the other regions can be found in Section 5 (Figures 40 to 49).

In Region 01, it becomes clear that smaller areas within the region determine the shape of the overall correlation. The data points forming the two spikes in the R1 and R2 band are located in two different corners of the image, namely the top left and top right corner in case of the spike at lower and higher optical depths, respectively. A similar phenomenon can be observed for Region 03, where the lower part of the image contributes to the correlation at low τ_{353} while the upper part shows no correlation. Additionally, the two clouds of data points forming the correlation can be separated by their position along the x axis. Analogous statements can be posed for the other regions, although the connection between the position in the ROSAT and *Planck* image and the position in the plots of intensity as a function of optical depth is not always as obvious. It has to be noted however, that structures aligned parallel to either of the two image axes would appear more clearly in these graphs than more complex shapes since the x and y coordinates of the image are chosen as an indicator of the pixel's location. Nevertheless, some regions evidently consist of several areas with distinct emission and

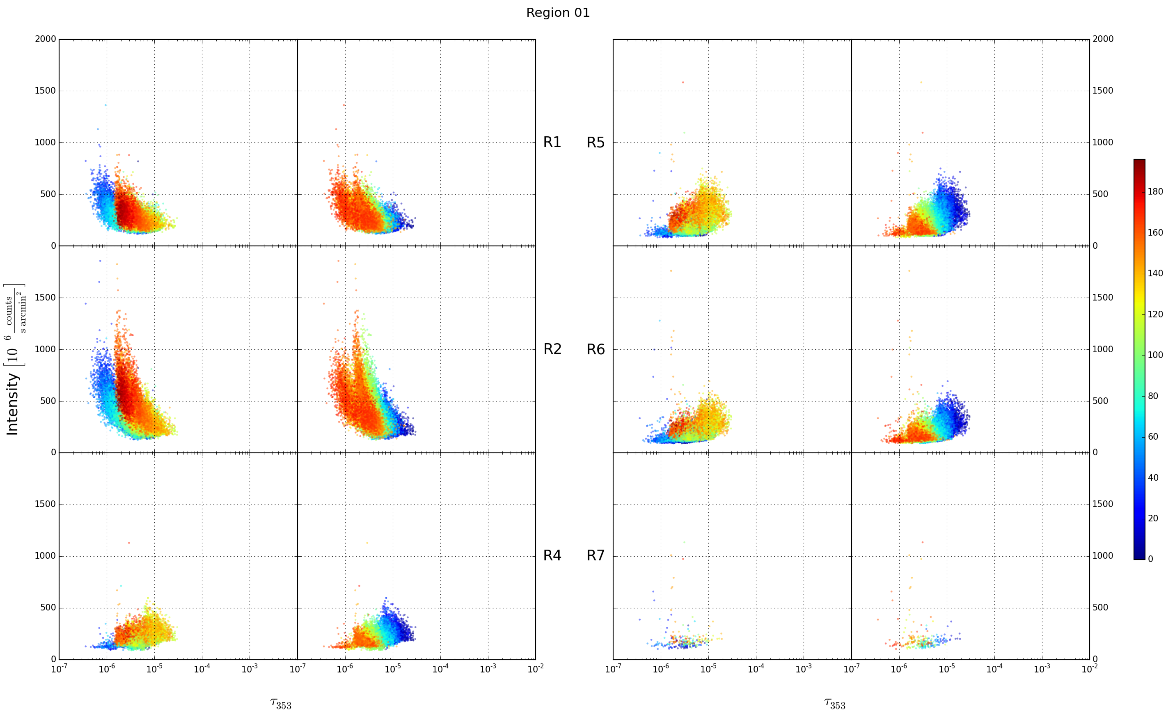

Figure 8: X-ray intensity as a function of dust optical depth in Region 01 for all bands, colour-coded with the pixel position. For each band, the left and right graphs show the position on the x and yaxis, respectively. The data points are semi-transparent and those with higher values in x or y are plotted on top.

absorption characteristics producing different patterns in the correlation between X-ray intensity and dust optical depth.

At least one of these substructures can be identified unambiguously, namely the North Polar Spur (NPS). In Region 01, it is located in the upper right corner of the image and Region sofue14b is centred on the lower section of the NPS. The North Polar Spur extends from the galactic plane at a longitude of approximately 20° in the direction of the north galactic pole and can be observed in both X-rays and the radio range as a prominent emitting structure (Sofue, 2015). A common theory states that the NPS is a part of a shock front caused by an event in the galactic centre and contains hot gas which is responsible for the emission in the X-ray and radio range. As discussed earlier, one cloud of correlated data points in Region 01 originates from the area of the NPS and is separated from another, also correlated cloud. Examining Region sofue14b (see Figure 49), no such differentiation is possible, implying that the area of the NPS has uniform emission and absorption properties and that therefore, a change in the geometry of emitting and absorbing structures within the NPS is unlikely. This is compatible with a study by Sofue (2015), who ultimately concluded that the NPS is a continuous structure located behind a region of dense material, the Aquila Rift.

Apart from localised formations of matter that absorb or emit X-ray radiation at different distances to the observer, changes in the shape of the correlation between X-

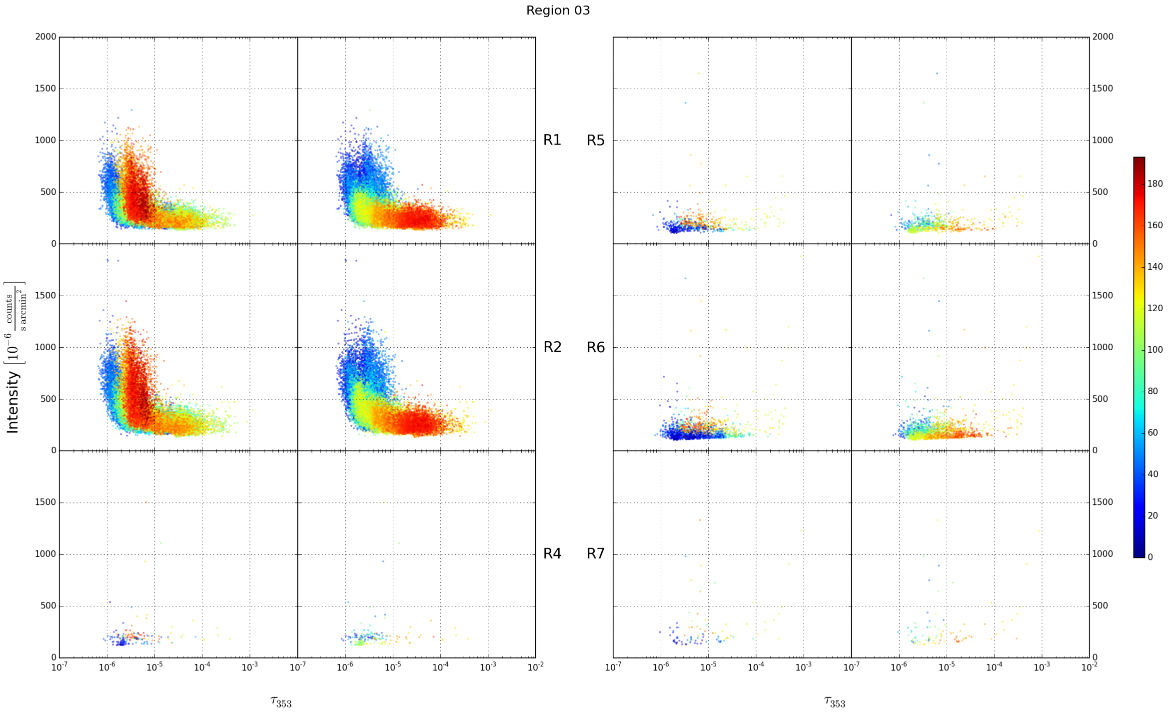

Figure 9: Same as Figure 8, but for Region 03.

ray intensity and dust optical depth can also be caused by varying ISM characteristics, for example dust properties. In order to study whether there is a connection between (non-)correlations in the previous plots and the characteristics of the emitting dust, the dust temperature is employed. The thermal dust emission detected by *Planck* is fitted with a dust model that includes the temperature T_{obs} as a fitting parameter (see Section 2.3.3). The true dust temperature corresponds to a temperature value averaged along the line of sight and weighted by the density. Although T_{obs} is generally not equivalent to the true dust temperature (Planck Collaboration et al., 2014), it contains information on the shape of the emission spectrum nonetheless. Figure 10 shows the results for R2 (for R1 and R4 to R7, see Figures 50 to 54).

A general trend for higher temperatures to occur where the optical depth is low can be observed. Correlations between the fit parameters of the *Planck* dust model have been examined by the creators of the maps (Planck Collaboration et al., 2014), who found global relations between β_{obs} and T_{obs} as well as β_{obs} and $\frac{\tau_{353}}{N_H}$. They concluded that the correlations are not artefacts of the data reduction process and also cannot be explained by noise in the data, and must therefore originate from real changes in the emission spectrum. Apart from the general negative correlation between T_{obs} and τ_{353}, the additional temperature information exhibits a behaviour different from the x and y positions, i.e. the substructures showing different correlations between the X-ray intensity and the dust optical depth within one region cannot be distinguished by their temperature.

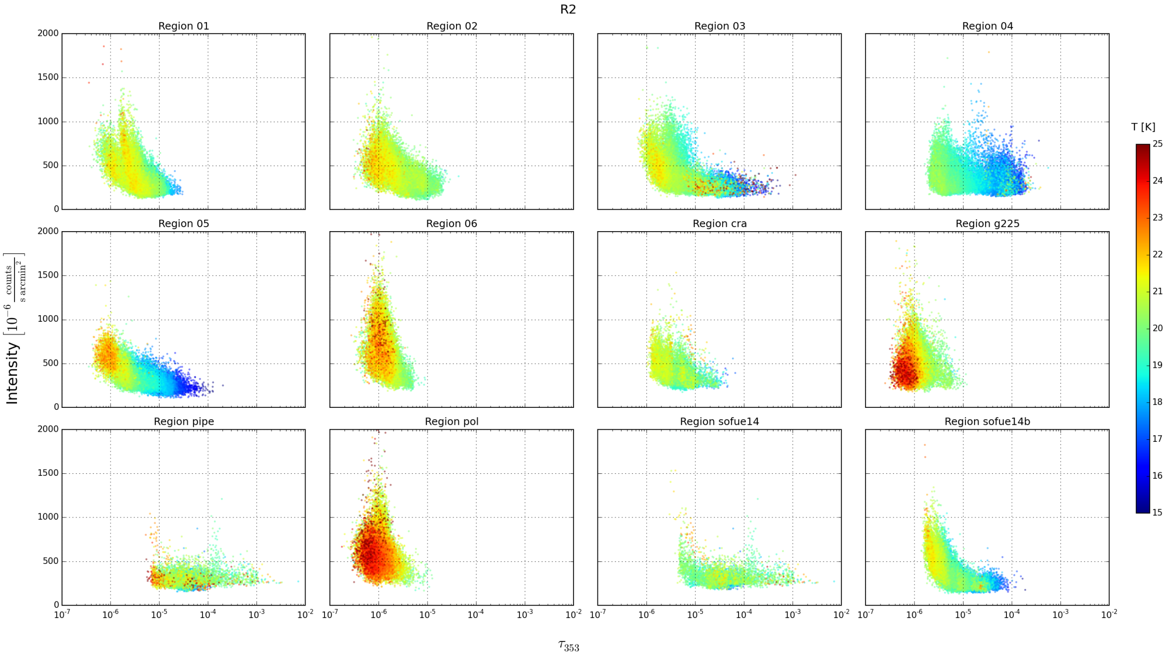

Figure 10: X-ray intensity as a function of dust optical depth in the R2 band, colour-coded with the dust temperature. The data points are semi-transparent and those with higher temperature values are plotted on top.

4.1.4 Conclusion

The comparison of X-ray intensities measured by ROSAT and the dust optical depth as deduced from *Planck* data in Regions approximately 30° × 30° in size has revealed a number of correlations in the lower ROSAT energy bands R1 and R2. Anticorrelations are generally only found for low values of τ_{353}, which can be attributed to the different distances along the line of sight traced by ROSAT and *Planck*. For several regions, a division into substructures can be conducted which separates areas showing a different shape in the relation between X-ray intensity and τ_{353}. This phenomenon suggests that the geometry or the properties of the emitting and absorbing material along the line of sight have changed. Therefore, any further analysis on the correlation should consider these substructures rather than the entire region. Using the dust temperature derived from *Planck* data, the areas causing different shapes in the correlation cannot be distinguished.

More detailed conclusions on the properties of the ISM across the entire sky are difficult to draw from this analysis, as this information is entangled with effects of the arrangement of X-ray emitting and absorbing layers. Analogous to the study of the North Polar Spur by Sofue (2015), every substructure that can be found to show a correlation between the X-ray intensity and dust optical depth would have to be analysed individually, and information on the 3-dimensional structure of the various phases of the

ISM would have to be retrieved from observations with other instruments or in different wavelength ranges.

4.2 Emission and Absorption by the Diffuse ISM Using Extragalactic Point Sources

4.2.1 Background and Motivation

In this part, the aim is to compare X-ray absorption as measured by point source observations to the dust optical depth deduced from microwave observations. To this end, the XMM-*Newton* spectral fit catalogue (see Section 3.2) and the *Planck* all-sky maps (see Section 3.4) are put to use along with the Sloan Digital Sky Survey (see Section 3.8) and the 2MASS catalogue (see Section 3.7).

The dust optical depth τ_ν, a product of the *Planck* observations relevant for this study, can be written as

$$\tau_\nu = \sigma_\nu N_H, \tag{11}$$

$$\tau_\nu = \kappa_\nu M_{dust} = \kappa_\nu \frac{M_{dust}}{M_{gas}} \mu m_H N_H, \tag{12}$$

where σ_ν is the dust opacity, N_H the equivalent hydrogen column density, κ_ν the dust emissivity cross-section per unit mass and M_{dust} the dust mass column density (Planck Collaboration et al., 2014). Although κ_ν depends on the composition and structure of dust grains, it is independent from the size distribution as the wavelength is large compared to the grain size. The gas mass column density $M_{gas} = \mu m_H N_H$, with μ being the mean molecular weight and m_H the mass of a hydrogen atom. If the properties of the diffuse ISM are similar in any direction of the sky, a comparison of the optical depth and the hydrogen column density for several point sources should give a linear relationship with the slope corresponding to the dust opacity.

As opposed to the previous study (see Section 4.1), X-ray observations of point sources are used to deduce the absorbing column density. This has several implications concerning data analysis and interpretation: On the one hand, the use of point sources allows for a more precise definition of the origin of X-ray radiation as it is simply the point source itself. Besides, an additional measure of extinction towards the source in the near-infrared range can be gained easily by a match with the 2MASS catalogue. On the other hand, conclusions on the properties of the ISM can only be drawn for individual lines of sight instead of larger regions or even the entire sky. Also, the absorbing column density N_H can only be derived if an intrinsic source spectrum is assumed, which requires additional knowledge about the source. Another feature of this comparison is that N_H is a measure of X-ray absorption only as far as the source's location, whereas the optical depth, being derived from dust emission, traces dust along the total line of sight. To overcome this complication, only extragalactic point sources are taken into account which is achieved by a match with the SDSS catalogue.

During the SDSS data reduction process, a source can be classified as either

- a galaxy, with the subclasses
    - starforming,
    - starburst and
    - active galactic nucleus (AGN),
- a star, with subclasses corresponding to stellar spectral types, or
- a quasi-stellar object (quasar, QSO).

Sources that are classified as galaxies or QSOs and show broad emission lines in their spectra are labelled by the word ‘broadline’ appended to their subclass name. As mentioned above, the goal is to identify extragalactic sources to ensure that all of the emitting and absorbing material is located in front of the source and at the same time, one of the models in the XMM-*Newton* spectral fit catalogue should represent the source spectra so that satisfying fitting results can be achieved. As galaxies are of extragalactic nature and their spectra are often well-described by a power-law model, they are chosen to be the sample of this study. In order to minimise the influence of intrinsic absorption additional constraints on the source type are necessary, which will be discussed in Section 4.2.3.

4.2.2 Data Analysis Procedure

As a first step, a match between the XMM-*Newton* spectral fit catalogue and the SDSS catalogue is performed in order to gain information on the source type. Due to the size of the SDSS database, several data access systems have been developed to execute different types of queries. However, all browser-based systems are connected with limits of the number of output entries and time out limits. Using SQL queries or spectroscopic form queries it is therefore not possible to download a list with all sources classified as galaxies, because this would exceed the row limit of 500 000. Although the spectroscopic query form allows for a position-constrained source search and would thus provide the desired galaxy matches without exceeding the row limit, the query surpasses the time limit if a list of more than approximately 5 900 positions and a search radius of $3''$ are given. With more than 114 000 entries in the XMM-*Newton* spectral fit catalogue, this is not a time efficient option. Because of these limitations, the SDSS catalogue available in the VizieR database is put to use instead. The complete list of source positions from the XMM-*Newton* spectral fit catalogue can be passed to VizieR, returning all matches within a radius of $3''$ from the source coordinates. For 62 398 entries in the XMM catalogue an SDSS match is found including 3 474 classified as galaxies which are shown in Figure 11.

An obvious disadvantage of using the SDSS catalogue in VizieR is the fact that the latest SDSS data release available in VizieR is SDSS DR9 which includes all data obtained by July 2011 (Ahn et al., 2012). The most recently published data release is DR12, comprising all observations within the first three SDSS generations that lasted

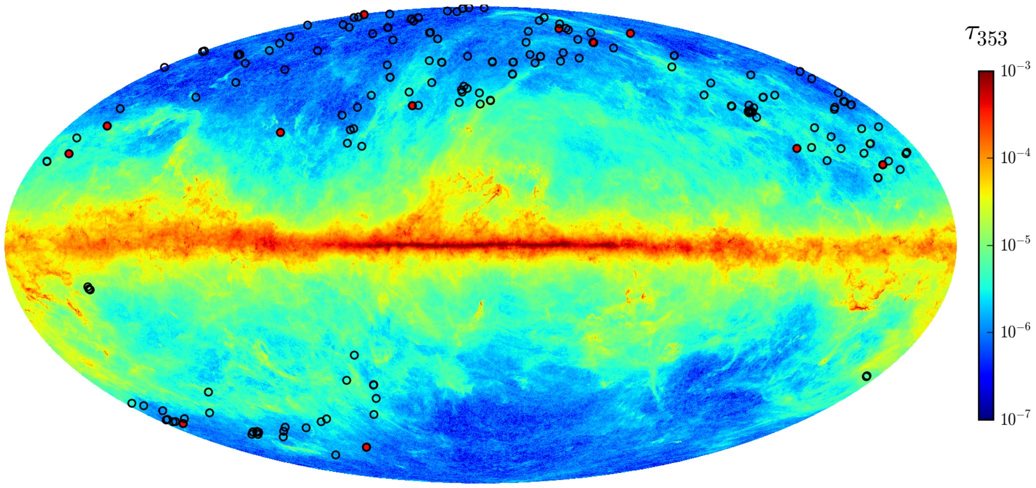

Figure 11: Map of τ_{353} based on data obtained by the *Planck* satellite overplotted with the locations of cross-correlated XMM-*Newton* and SDSS sources classified as galaxies. Filled red circles indicate broad-line AGN.

until July 2014. Furthermore, the SDSS catalogue in VizieR is a slim version of the original database and therefore does not contain all source parameters. But since the analysis will be restricted to X-ray sources that have an SDSS match classified as a galaxy, the number of relevant entries is reduced significantly and obtaining the missing data from the original catalogue with the spectroscopic query form is possible without exceeding the time out limit.

Next, the resulting catalogue of XMM and SDSS sources is matched with 2MASS data. Again, the positional search function of VizieR is employed with a match radius of $3''$. The final data set consists of 62 398 XMM-*Newton* spectral fit catalogue entries with SDSS matches, 23 083 of which have counterparts in the 2MASS catalogue. For each entry, the optical depth is found by identifying the pixel in which the source's coordinates lie and extracting the corresponding pixel value from the *Planck* τ_{353} map.

4.2.3 Results and Discussion

A comparison between the column density N_H from the XMM-*Newton* spectral fit catalogue and the optical depth τ_{353} as given by the *Planck* all-sky dust model is shown in Figure 12 for all sources that are classified as galaxies in the SDSS catalogue. Only sources with a spectral fitting flag equal to 0 are taken into account, as this ensures that the fitting procedure was performed without any problems and valid errors are given. The spectral fit catalogue lists every source observation as an independent entry and spectra of the same source obtained during separate observations are fit individually. For this reason, the same source can be listed with several different values of N_H. In order to circumvent this complication, a weighted mean of the column density is calculated for each unique source, using the errors in N_H as weights.

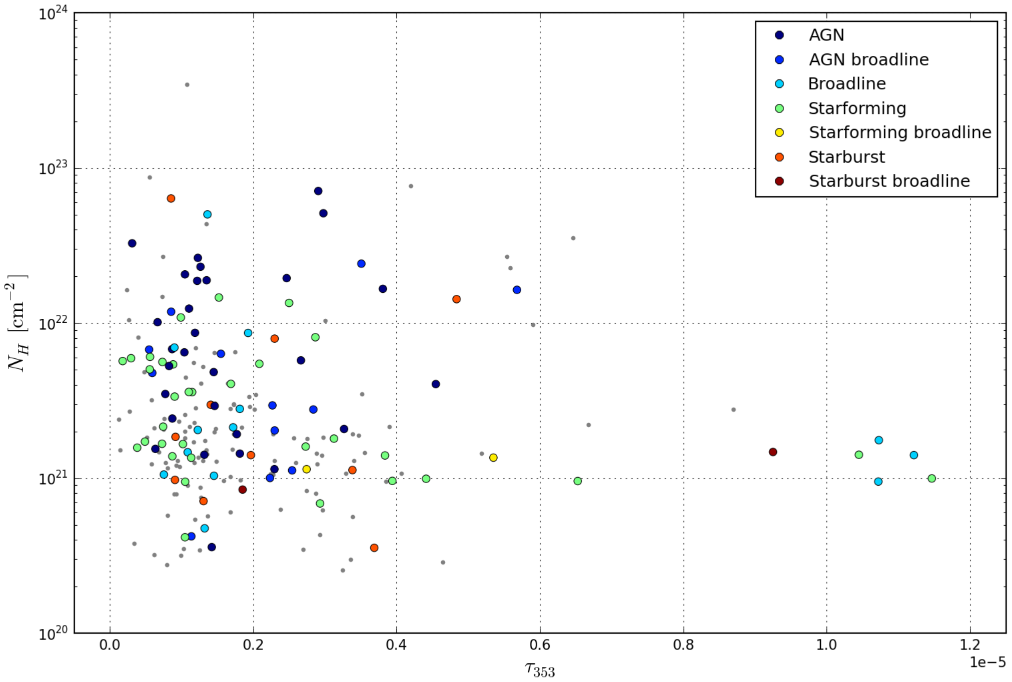

Figure 12: Hydrogen column density N_H as a function of optical depth τ_{353} for galaxies. Colours indicate the assigned subclass, grey points mark sources without a subclass label.

For the complete galaxy sample, no correlation between N_H and τ_{353} can be observed. Some possible explanations are:

(a) The optical depth used for each source corresponds to the value of the pixel in which the source is located. Any variations that occur within one *Planck* pixel are averaged to give the resulting τ_{353} value. This discrepancy between the pin-point measurement of the hydrogen column density and the spatially averaged measurement of the optical depth may corrupt the correlation.

(b) The intrinsic absorption of each galaxy is different, as it depends on the exact source type and the inclination of the system with respect to the line of sight. Intrinsic absorption is directly translated into higher N_H values because it alters the X-ray spectrum of the galaxy but is not reflected in the measured dust emission intensity towards the source. Therefore, the correlation may be lost.

(c) For sources that are not galaxies, it is not clear whether their spectra can be approximated by the absorbed power-law model in the XMM-*Newton* spectral fit catalogue. The hydrogen column density for the absorbed power-law model may therefore not be the appropriate value for these sources. If the sample is contaminated by sources that have been classified as galaxies but actually belong to another source type, the linear relationship between N_H and τ_{353} may not be evident.

(d) The properties of the ISM change considerably from one line of sight to another. If this is the case, it is not possible to find a single value for the dust opacity that is valid throughout the entire sky and no linear relation can be observed for sources located in different parts of the sky.

The variation of the optical depth within one pixel of the *Planck* map can only be assessed by a comparison with a higher-resolution map of τ_{353} that is deduced from a similar dust emission model. Maps produced from *Herschel* data could therefore be used for such a test. However, *Herschel* maps are not available for the entire sky and suffer from the same fundamental problem as *Planck* data because of their limited angular resolution. Acquiring a reliable measure of the influence of spatial resolution on the correlation examined here would therefore require a dedicated study, which is beyond the scope of this work. Nevertheless it can be said that considering the distribution of data points in Figure 12 it seems unlikely that the non-correlation between N_H and τ_{353} can be explained by scatter around a functional relation that is primarily caused by the spatial resolution of the optical depth data.

In order to examine the importance of intrinsic absorption in this comparison, a sample subset needs to be found that includes sources with little or no intrinsic absorption. Recovering the expected linear relation using only this subset would imply that the non-correlation for the complete galaxy subset is indeed caused by varying intrinsic absorption.

For AGN, a clear statement on the intrinsic absorption can be made. An active galactic nucleus is a supermassive black hole at the centre of a galaxy. Its spectrum consists of continuum emission that can be approximated by a power-law (see Section 2.3.1) and emission lines that originate from gas orbiting the AGN. As the width of the emission lines is determined by the motion of the emitting gas in the AGN's gravitational potential, broad lines are generated closer to the central object than narrow lines. Depending on the width of the emission lines occurring in their spectrum, one type of AGN, namely Seyfert galaxies, are classified as either Seyfert 1 galaxies with both broad and narrow lines or Seyfert 2 galaxies revealing only narrow lines. The fact that Seyfert 2 galaxies show evidence for strong intrinsic absorption indicates that the broad-line region is located behind obscuring material in those objects (Comastri et al., 1995). Consequently, low intrinsic absorption is a prerequisite for the detection of broad emission lines as observed in Seyfert 1 galaxies (Kazanas et al., 2012). As a result, the subclass of broad-line AGN is chosen as a suitable subsample to examine the correlation between N_H and τ_{353} which is shown in Figure 13.

Also for broad-line AGN, the correlation between the column density and the optical depth is not clear. To ensure that all sources in the subsample are correctly classified as galaxies and AGN, the reduced-χ^2 value of the SDSS fit can be put to use. As can be seen in Figure 14, most galaxies show a reduced-χ^2 value between 1 and 3. A threshold value of 5 is chosen, causing two broad-line AGN to be labelled as possible misclassifications. Although this procedure excludes one outlier, a clear trend is not evident. Assuming a linear relation between N_H and τ_{353} as discussed in Section 4.2.1, the data points are fitted employing an ordinary least-squares algorithm and the errors in the

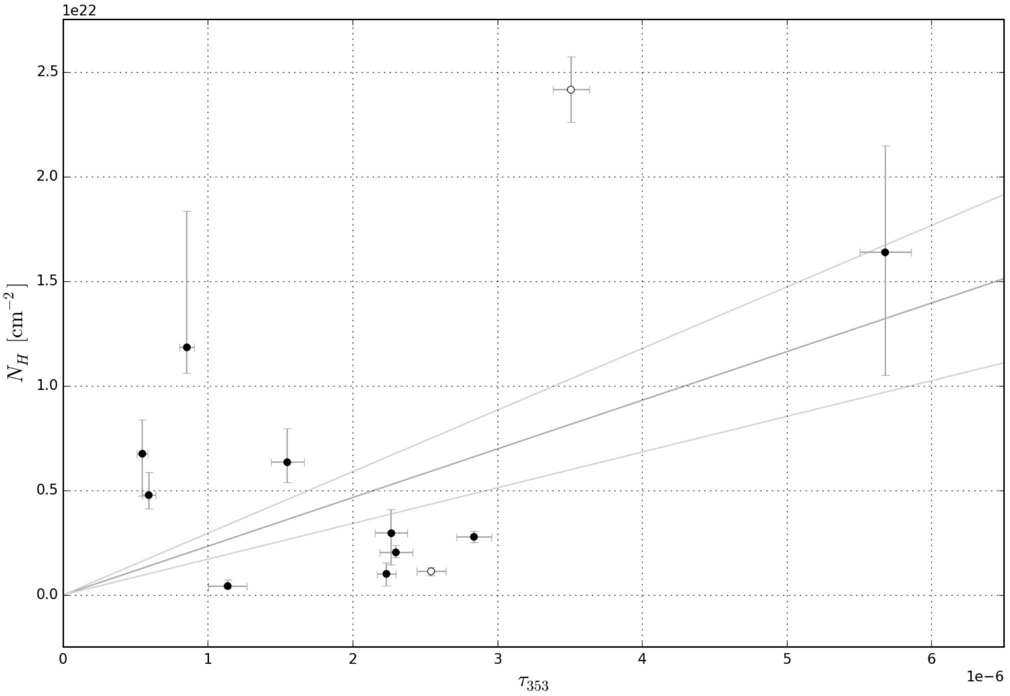

Figure 13: Hydrogen column density N_H as a function of optical depth τ_{353} for broad-line AGN. As a measure of the errors, the error bars represent the uncertainty for every data point in terms of 1-σ values in τ_{353} and 90 % confidence intervals in N_H. The dark and light grey lines show the best linear fit and its 1-σ deviation, respectively. Possible misclassifications are marked with empty circles.

optical depth as weights. The confidence intervals given in the XMM-*Newton* spectral fit catalogue are not taken into account for two reasons: First, the confidence intervals are generally asymmetric, a case which is not implemented in the fitting algorithm. Second, only the error of N_H as a fitting parameter is represented by the confidence intervals and instrumental uncertainties or any errors introduced during data reduction are not included. Some data points therefore have very low relative errors ($< 5\,\%$), which would force the fit line towards these points. Using this fitting setup, the fitted line is represented by the function

$$N_H = (2.33 \pm 0.62) \cdot 10^{27}\,\mathrm{cm}^{-2} \cdot \tau_{353} \tag{13}$$

$$\longrightarrow \frac{\tau_{353}}{N_H} = \sigma_{353} = (4.30 \pm 1.14) \cdot 10^{-28}\,\mathrm{cm}^2. \tag{14}$$

For optical depths less than $3 \cdot 10^{-6}$, a large scatter around the fit line can be seen and only the data point at $\tau_{353} \sim 5.7 \cdot 10^{-6}$ lies within its 1-σ range. Furthermore, the fit is very sensitive to the position of this data point as it has a strong influence on the correlation. Omitting this data point would give a completely different picture of the

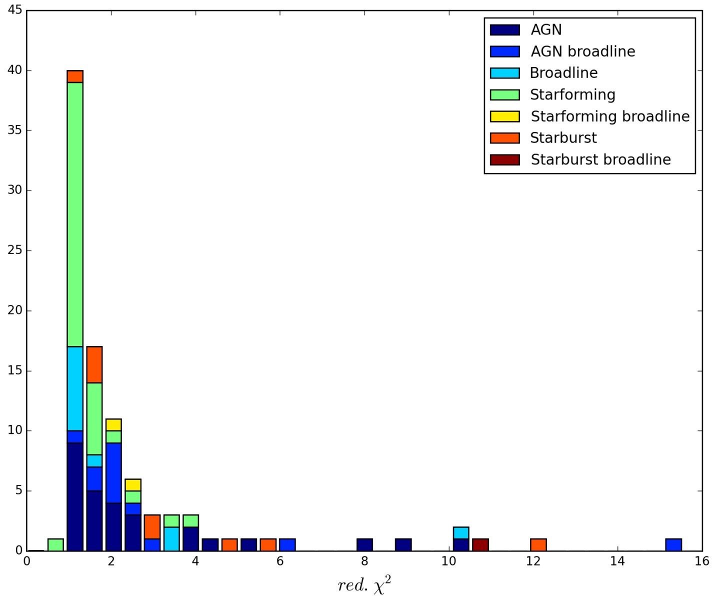

Figure 14: Histogram of reduced-χ^2 values for galaxies. Colours indicate the assigned subclass. Sources without a subclass label are not included in the graph.

general trend the data appear to follow. The fact that only a weak correlation can be observed can be an indication that the assumption of a similar dust opacity towards all studied AGN is incorrect, which is also mentioned in the publication of the *Planck* all-sky dust model in more general terms (Planck Collaboration et al., 2014). However, the small sample size limits the power of any conclusions that can be drawn from the available data.

Instead of using thermal dust emission, the optical magnitudes given in the SDSS catalogue and near-infrared magnitudes from the 2MASS catalogue can be employed as a measure of dust extinction. The results are presented in Figures 15, 16, 17 and 18.

For both the optical and the near-infrared colours, no connection to the hydrogen column density can be found if all galaxies are considered. Nevertheless, restricting the sample to broad-line AGN yields a clear correlation between N_H and the three optical colours $(g-r)$, $(r-i)$ and $(i-z)$. Following a similar fitting procedure as described above, the data points are fitted with the same algorithm, taking errors in the optical colours into account and excluding sources with reduced-χ^2 values larger than 5. The scatter around the linear fitting curve is smaller than for τ_{353} and as opposed to the comparison with *Planck* data, there is no single data point that dominates the correlation. The parametrisation of the fitted lines can be written as

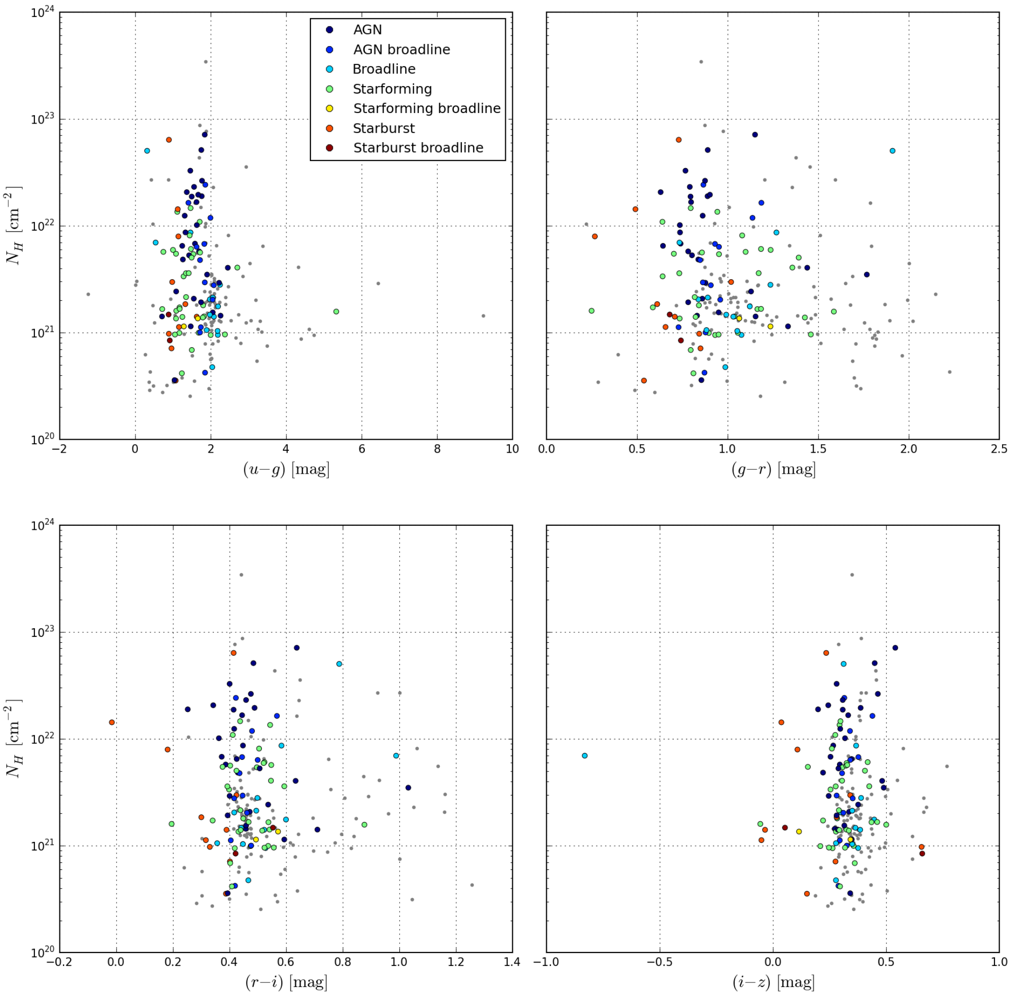

Figure 15: Hydrogen column density N_H as a function of optical colours for galaxies. Colours indicate the assigned subclass, grey points mark sources without a subclass label.

$$N_H = (3.95 \pm 0.66) \cdot 10^{22}\,\frac{\mathrm{cm}^{-2}}{\mathrm{mag}} \cdot (g-r) + (-3.22 \pm 0.63) \cdot 10^{22}\,\mathrm{cm}^{-2}, \tag{15}$$

$$N_H = (8.85 \pm 2.51) \cdot 10^{22}\,\frac{\mathrm{cm}^{-2}}{\mathrm{mag}} \cdot (r-i) + (-3.57 \pm 1.17) \cdot 10^{22}\,\mathrm{cm}^{-2}, \tag{16}$$

$$N_H = (8.67 \pm 2.36) \cdot 10^{22}\,\frac{\mathrm{cm}^{-2}}{\mathrm{mag}} \cdot (i-z) + (-2.36 \pm 0.80) \cdot 10^{22}\,\mathrm{cm}^{-2}. \tag{17}$$

For $(u-g)$, the correlation is weaker and yields a negative slope, which is contradictory to the mean extinction law since the extinction at longer wavelengths is expected to be lower (see Section 2.3.2). Similar to the comparison with τ_{353}, one data point has a

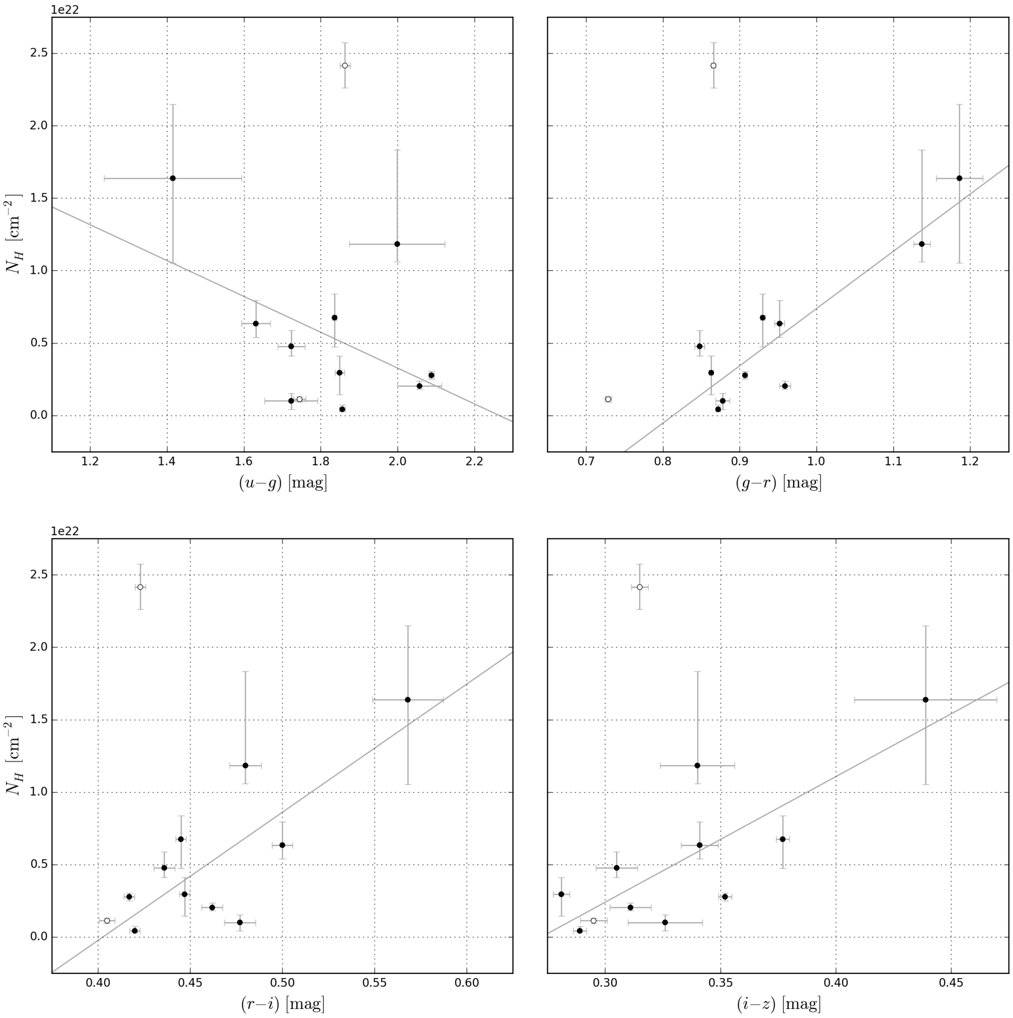

Figure 16: Hydrogen column density N_H as a function of optical colours for broad-line AGN. Error bars correspond to 1-σ values. The grey line shows the best linear fit. Possible misclassifications are marked with empty circles.

strong influence on the type of correlation and its absence would leave the data set appearing uncorrelated. The fitting curve is given by

$$N_H = (-1.24 \pm 0.76) \cdot 10^{22} \, \frac{\mathrm{cm}^{-2}}{\mathrm{mag}} \cdot (u - g) + (2.80 \pm 1.39) \cdot 10^{22} \, \mathrm{cm}^{-2}. \tag{18}$$

Considering the near-infrared colours $(J - H)$ and $(H - K)$, no correlation with N_H can be observed. Although this may be due to real physical phenomena, the errors in $(J - H)$ and $(H - K)$ are too large to pose a reliable statement on the relation between the extinction in the near-infrared and the hydrogen column density.

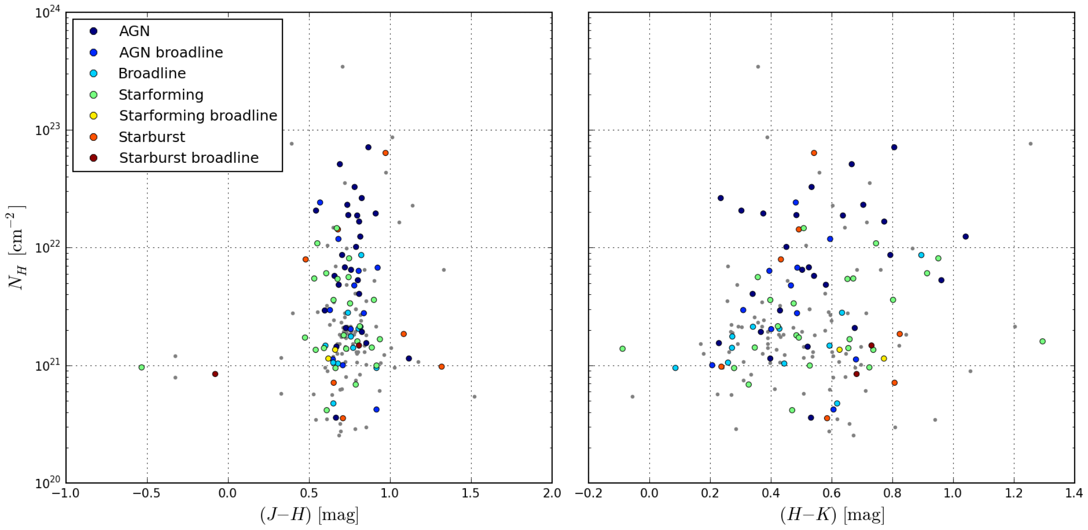

Figure 17: Hydrogen column density N_H as a function of near-infrared colours for galaxies. Colours indicate the assigned subclass, grey points mark sources without a subclass label.

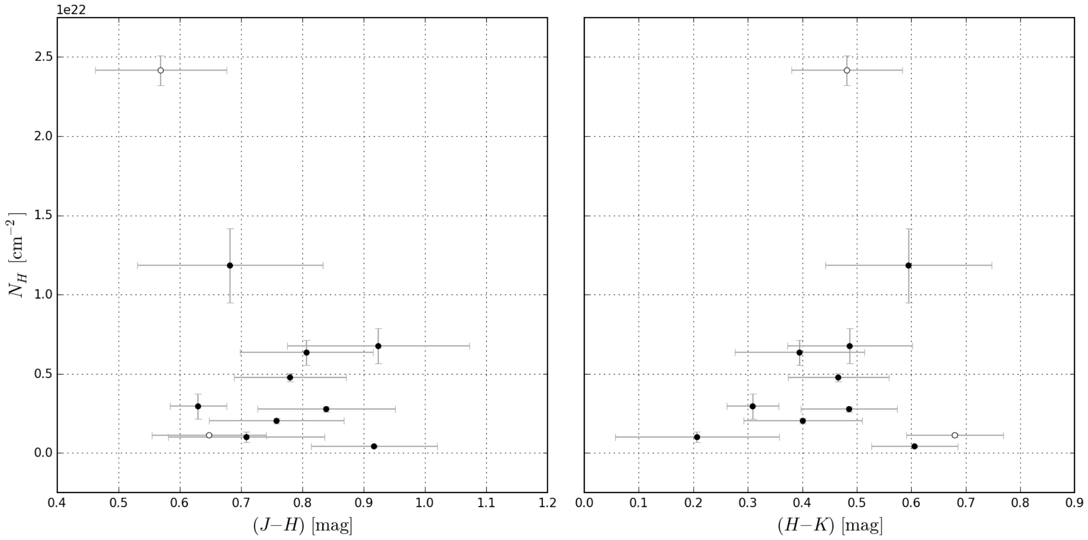

Figure 18: Hydrogen column density N_H as a function of near-infrared colours for broad-line AGN. Error bars correspond to 1-σ values. Possible misclassifications are marked with empty circles.

4.2.4 Conclusion

The equivalent hydrogen column density derived from X-ray spectra of galaxies is compared to several measurements of dust emission and extinction. In an effort to avoid the influence of intrinsic absorption, the source sample is restricted to broad-line AGN. Only a weak correlation between N_H and the dust optical depth as given by sub-millimetre measurements of thermal dust emission can be found. Due to the small sample size and the lack of reliable error estimates for N_H, the significance of conclusions drawn from these data is however limited. Nevertheless it can be said that this study suggests that the dust opacity varies considerably for different lines of sight.

A much stronger correlation is observed if the hydrogen column density is compared to the optical colours $(g-r)$, $(r-i)$ and $(i-z)$. The improvement of the correlation could be caused by the fact that both the hydrogen column density and the optical magnitudes are deduced from pin-point measurements, which is not the case for τ_{353}. At the same time, optical and sub-millimetre observations trace different characteristics of interstellar dust (see Sections 2.3.2 and 2.3.3) and are therefore difficult to compare directly. Finally, the relation between N_H and the near-infrared colours $(J-H)$ and $(H-K)$ is studied. However, no conclusions can be drawn from this comparison due to the large error bars in the 2MASS data.

While the data analysis described in this section implies that the interstellar medium shows some variation in its properties at different locations in the sky, conclusions need to be drawn with care. Several mechanisms that cannot be avoided at this point may alter the (non-)correlations, including differences in measurement techniques and error calculations. The choice of a suitable source sample and comparable data sets is therefore of paramount importance for such studies.

4.3 Emission and Absorption by the Dense ISM Using Young Stellar Objects in Orion

4.3.1 Background and Motivation

In the third part of the data analysis, the dense ISM is studied by using high-resolution data on the Orion Nebula Cluster. The ONC is a nearby star-forming region at a distance of 414 pc containing several thousand stars (Hillenbrand, 1997; Menten et al., 2007). Apart from a young stellar population within the dense gas of the nebula, the examined area also accommodates a foreground population as well as foreground and background field stars (Alves and Bouy, 2012). As one of the best-studied star-forming regions, observations in various wavelength ranges are available. Here, the *Chandra* Orion Ultradeep Project (see Section 3.3) and Pillitteri catalogues (see Section 3.2) are used along with an extinction map produced from *Planck* and *Herschel* data (see Section 3.5) and the VISION catalogue (see Section 3.6) which was built from VISTA data. Additionally, the Orion A catalogue by Bouy et al. (2014) provides a list of probable foreground sources.

Similar to the previous study, the equivalent hydrogen column density N_H derived from X-ray observations is compared to the a measure of the amount of dust along the line of sight. In Section 4.2, the optical depth τ_ν is employed, which is expected to exhibit a linear relation to N_H with the dust opacity $\sigma_\nu = \frac{\tau_\nu}{N_H}$ as a proportionality factor. However, dust emission and extinction have been shown to correlate in the entire Orion complex (Lombardi et al., 2014), and therefore the *Herschel* map is calibrated to give the dust extinction in terms of A_K.

A major advantage of this analysis is the fact that a large number of surveys have targeted the ONC, and thus, the properties of the observed region can be constrained to a larger extent than is possible for an arbitrary line of sight. For example, the VISION catalogue, which gives information on the near-infrared magnitudes of the sources, can be used to provide an additional measure of dust extinction. Furthermore, the characteristics of the ISM are not expected to change substantially within a small region on the sky, increasing the chances of finding a correlation between N_H and A_K. Finally, addressing the issue of variations within one *Planck* pixel as mentioned in Section 4.2.3, the available high-resolution images by *Herschel* are less likely to compromise the conclusions drawn from the comparison.

4.3.2 Data Analysis Procedure

First, the COUP catalogue is combined with the COUP membership catalogue as available in VizieR, by matching the COUP sequence numbers given in both catalogues. The remaining data preparation steps required in this study are performed in an analogous manner for the COUP and Pillitteri catalogues. The positions of the COUP and Pillitteri sample are correlated with the source coordinates in the VISION catalogue in a radius of $3''$. For 1 333 entries in the COUP and 171 in the Pillitteri catalogue, a near-infrared match can be found. Then, a match with the optical and near-infrared catalogue by Bouy et al. (2014) with the same search radius is conducted in order to gain information on the sources' membership to the foreground population. Objects with a membership probability higher than 99.5 % are regarded as foreground sources in this study. As a final step, the pixel of the *Herschel* map in which the source coordinates lie is identified for each COUP and Pillitteri entry, and the corresponding pixel value multiplied by the conversion factor of $\frac{A_K}{\tau_{353}} = 2.64 \cdot 10^3$ mag as derived by Lombardi et al. (2014) is assumed as the A_K value.

4.3.3 Results and Discussion for the COUP sample

Due to the differences in the results for the COUP and the Pillitteri catalogue, they are presented in two sections. For the results from the Pillitteri sample, see Section 4.3.4.

In Figure 19, a comparison between the equivalent hydrogen column density as deduced in the COUP catalogue and the extinction in the K band, taken from the *Herschel* map, is depicted. Data points corresponding to saturated *Herschel* pixels as well as sources that are listed with unreliable values of N_H in the COUP catalogue. Hydrogen column densities are regarded as reliable if no complications occurred during the fitting process and the χ^2 value lies between 0.5 and 2.0.

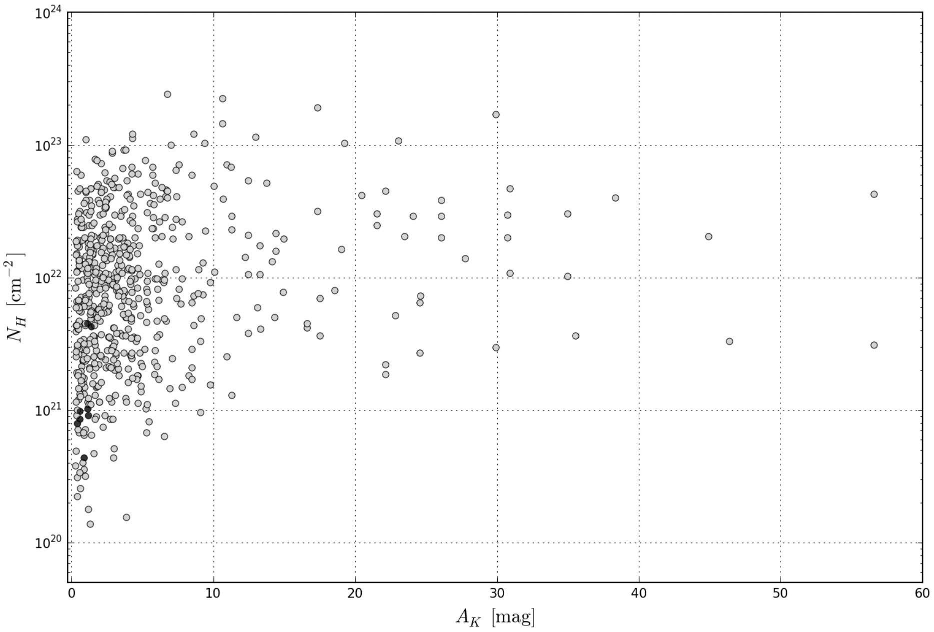

Figure 19: Hydrogen column density N_H as a function of extinction in the K band A_K for the COUP sample. Foreground sources are plotted on top as black points.

Both the hydrogen column density and the extinction span a large range of values, which is particularly noteworthy for A_K since a previous study by Vuong et al. (2003) found a correlation between N_H and A_V for A_V values up to approximately 3. Using the conversion proposed by Cardelli et al. (1989) (see Section 2.3.2) for $R_V = 3.1$, an extinction value of $A_V = 3$ can be converted to $A_K = 0.34$ compared to the maximum A_K of approximately 60 in this study. However, no correlation can be observed between the hydrogen column density and extinction. Similar to the analyses in Section 4.1 and 4.2, an obvious explanation is related to the difference between the distances traced by X-ray absorption of point sources and thermal dust emission. For objects in front of the Orion Nebula in particular, the largest part of the dust traced by *Herschel* and *Planck* is located behind the source, implying that the hydrogen column density and dust emission are not correlated. A total of 20 entries in the matched COUP and VISION sample are flagged as probable foreground sources in the optical and near-infrared catalogue on Orion A created by Bouy et al. (2014) and are indicated specifically in the graphs of this analysis. Analogous effects resulting in a non-correlation may arise for objects within the cloud. The location of sources with respect to the dense cloud may thus represent a crucial aspect in the study of the correlation between N_H and A_K.

In order to evaluate this possibility, an alternative measurement of dust column density, namely near-infrared colour observations, are used. These trace only material in front of the source and are therefore comparable to the X-ray extinction values. The COUP catalogue provides near-infrared magnitudes in the J, H and K band for 1 311 sources. Again, entries with unreliable N_H values are not considered in this analysis. The resulting comparison between the two colours $(J-H)$ and $(H-K)$ and the hydrogen column density is shown in Figure 20. Here, a clear correlation between N_H and the near-infrared colours can be observed, confirming the earlier hypothesis that material located behind the star influences the *Herschel* measurements substantially for a large number of sources. In a logarithmic plot the relation follows an exponential function, corresponding to the expected linear relationship between N_H and extinction.

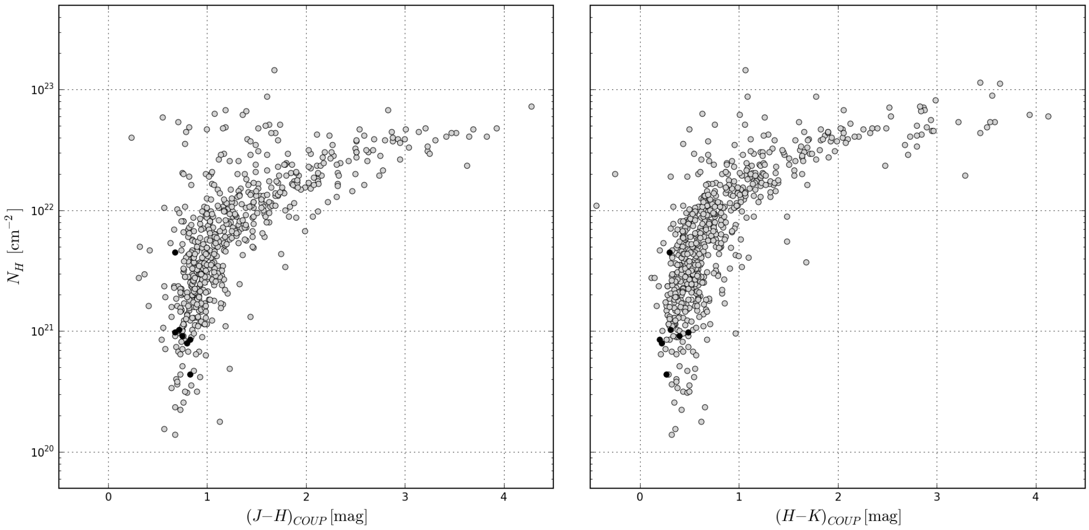

Figure 20: Hydrogen column density N_H as a function of near-infrared colours as given in the COUP catalogue. Foreground sources are plotted on top as black points.

With the VISION catalogue covering the entire Orion A cloud including the ONC, the near-infrared colours as listed in the COUP and VISION catalogues can be compared directly (see Figure 21). COUP data points are included irrespective of their behaviour

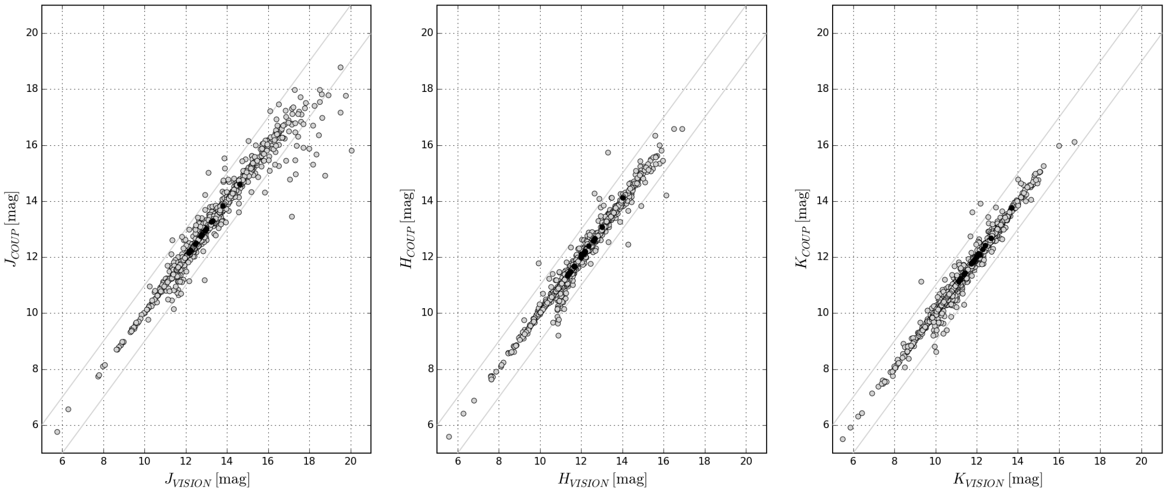

Figure 21: COUP and VISION near-infrared colour magnitudes compared. Foreground sources are plotted on top as black points. Grey lines indicate a deviation of 1 mag from equality.

during the fitting process, as the near-infrared magnitudes are not derived from the *Chandra* X-ray data. To a large extent, the two data sets list matching values for all three bands. However, several outliers can be identified, particularly for the J band where the COUP magnitude is significantly lower than the magnitude reported in the VISION catalogue for approximately 20 sources. As this behaviour may be caused by systematic errors in either catalogue and it is beyond the scope of this work to evaluate which of the two catalogues provides a more reliable measurement of near-infrared magnitudes, sources with considerable differences between the COUP and VISION magnitudes, i.e. ΔJ, ΔH or $\Delta K > 1\,\mathrm{mag}$, are excluded from the study. The COUP catalogue does not include error estimates for the J, H and K-band magnitudes, which is why the VISION catalogue is used in the following analysis.

Instead of analysing each of the colours individually, the NICER algorithm (see Section 2.3.2) is employed. The algorithm estimates the extinction A_V for each source with the following input parameters:

- the J, H and K-band magnitudes of the source and their errors. They are retrieved directly from the VISION catalogue.
- the covariance matrix of near-infrared colour magnitudes and their average value for a similar source population not affected by extinction, $(J-H)_0$ and $(H-K)_0$. For these parameters, the VISION control field is used. Comprising almost 94 000 sources, the field is located at a similar galactic latitude as the Orion Nebula, but shifted in galactic longitude by approximately 24°. The derived values for $(J-H)_0$ and $(H-K)_0$ are 0.62 and 0.39, respectively.

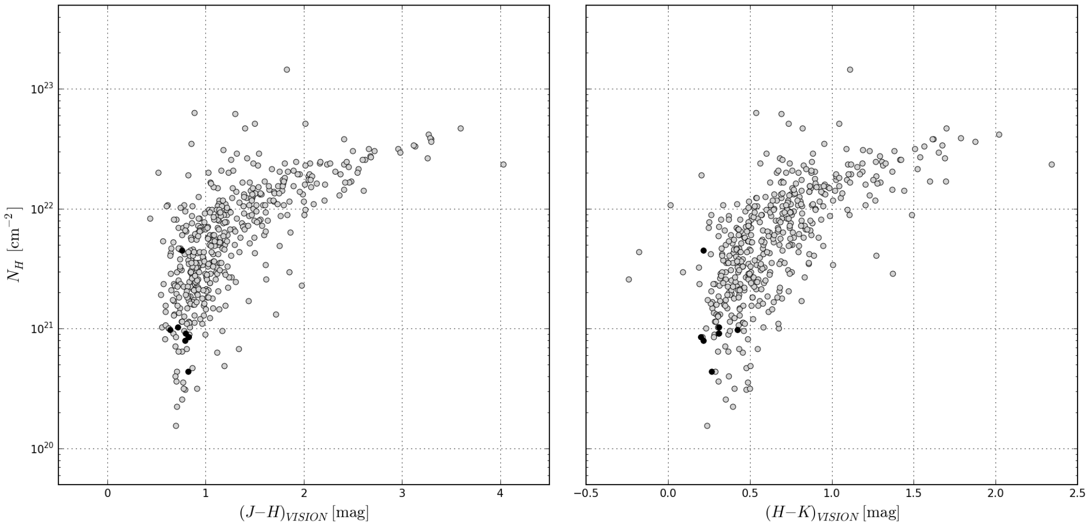

Figure 22: Hydrogen column density N_H as a function of near-infrared colours as given in the VISION catalogue for the COUP sample. Foreground sources are plotted on top as black points.

- the values of $\frac{A_J - A_H}{A_V}$ and $\frac{A_H - A_K}{A_V}$. As discussed in Section 2.3.2, the shape of the extinction law can be described by one parameter, namely R_V, which is set to the galactic value of 3.1 in a first analysis. Also, the effect of altering this value is examined.

The correlation between the hydrogen column density and A_V as calculated using the NICER algorithm can be observed in Figure 23. Catalogue entries listed with an unreliable value of N_H or a large difference between the COUP and VISION magnitudes are excluded from the graph.

The data points, excluding those as well as those flagged as foreground sources, are fitted with a linear function, which yields the relation

$$\frac{N_H}{A_V} = (1.195 \pm 0.037) \cdot 10^{21} \, \frac{\mathrm{cm}^{-2}}{\mathrm{mag}}. \tag{19}$$

This ratio is considerably smaller than the value derived previously for the diffuse ISM in the Milky Way: Vuong et al. (2003) have compiled a list of studies which employed X-ray absorption to derive $\frac{N_H}{A_V}$, giving values between 1.8 and 2.2 $\frac{\mathrm{cm}^{-2}}{\mathrm{mag}}$. The same authors examined the gas-to-dust ratio in nearby dense clouds and also found $\frac{N_H}{A_J}$ to be lower than the galactic value for ρ Ophiuchus. Assuming no systematic error in the data sets at hand, this can be explained by a different gas-to-dust ratio or altered dust properties in the ONC region compared to the diffuse ISM of the Milky Way.

First, a possible change in the gas-to-dust ratio is examined. The ratio $\frac{N_H}{A_V}$ can be written as

$$\frac{N_H}{A_V} = \frac{M_{gas}}{M_{dust}} \cdot \frac{1}{m_H} \cdot \frac{M_{dust}}{A_V}, \tag{20}$$

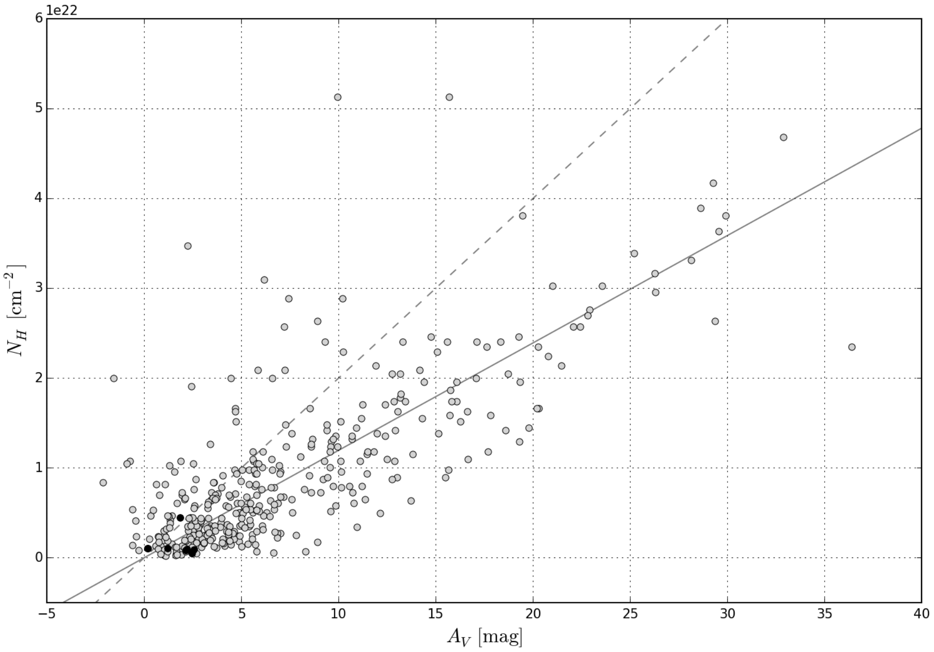

Figure 23: Hydrogen column density N_H as a function of extinction A_V calculated using the NICER algorithm and near-infrared colours from the VISION catalogue for the COUP sample. Foreground sources are plotted on top as black points. The solid line represents a linear fit to the data points. The dashed line corresponds to the galactic value of $\frac{N_H}{A_V} = 2 \cdot 10^{21}\,\frac{\text{cm}^{-2}}{\text{mag}}$.

where M_{gas} and M_{dust} are the gas and dust column mass densities, respectively, and m_H is the mass of the hydrogen atom. For a given grain size distribution $n(a)$ between the radii a_{min} and a_{max},

$$M_{dust} = \int_{a_{min}}^{a_{max}} \rho(a) \cdot \frac{4}{3}\pi a^3 \cdot n(a) da, \tag{21}$$

$$A_V = \int_{a_{min}}^{a_{max}} Q_V(a) \cdot \pi a^2 \cdot n(a) da, \tag{22}$$

with the dust mass density $\rho(a)$ and the extinction cross section $Q_V(a)$. If the dust parameters $n(a)$, $\rho(a)$, $Q_V(a)$, a_{min} and a_{max} are assumed to be equal for the Milky Way and the ONC, then $\frac{N_H}{A_V}$ is proportional to the gas to dust ratio with the same proportionality factor and thus

$$\left(\frac{M_{gas}}{M_{dust}}\right)_{ONC} = \frac{\left(\frac{N_H}{A_V}\right)_{ONC}}{\left(\frac{N_H}{A_V}\right)_{gal}} \cdot \left(\frac{M_{gas}}{M_{dust}}\right)_{gal}. \tag{23}$$

Adopting the galactic value for $\frac{N_H}{A_V}$, $2 \cdot 10^{21}\,\frac{\text{cm}^{-2}}{\text{mag}}$, and a gas-to-dust ratio of 100, the gas-to-dust ratio in the ONC region is approximately 60. While a similar value has been derived for ρ Ophiuchus (Vuong et al., 2003), further observations are needed to confirm the assumption of uniform dust parameters and the resulting increase in dust mass.

A change in dust properties can be traced by R_V which determines one of the input parameters for the NICER algorithm. Therefore, the algorithm is used with varying values of R_V to examine the influence of R_V on the $\frac{N_H}{A_V}$ ratio. For the star θ^1 Orionis C, Mathis and Wallenhorst (1981) derived a value of 5.5 for R_V, significantly larger than the galactic value of 3.1. Assuming $R_V = 5.5$,

$$\frac{N_H}{A_V} = (1.414 \pm 0.043) \cdot 10^{21} \, \frac{\text{cm}^{-2}}{\text{mag}}, \tag{24}$$

which is still well below the galactic value. Even for $R_V = 10.0$,

$$\frac{N_H}{A_V} = (1.541 \pm 0.047) \cdot 10^{21} \, \frac{\text{cm}^{-2}}{\text{mag}}. \tag{25}$$

It can be said that R_V has little effect on the $\frac{N_H}{A_V}$ ratio, as the shape of the extinction law in the near-infrared range shows only slight variations with changing values of R_V (see Section 2.3.2). For typical values of R_V in dense clouds, the galactic $\frac{N_H}{A_V}$ ratio can thus not be reproduced from the COUP and VISION data.

The observation of a clear correlation between the absorbing hydrogen column density and near-infrared colour magnitudes confirms the hypothesis that the non-correlation with extinction values from *Herschel* is due to the fact that microwave measurements trace dust emission along the entire line of sight. In an attempt to identify sources for which N_H and A_K provide comparable measurements of interstellar matter, the visual extinction derived from VISION data and the extinction in the K band from the *Herschel* map are compared for the entire Orion A region in Figure 24. VISION catalogue entries which correspond to saturated *Herschel* pixels are excluded from the graph.

As can be seen in Figure 24, the majority of sources in the Orion A region follows a linear relation between A_K and A_V. However, there is a group of data points with positions away from this general trend at higher A_K values, supporting the idea that for part of the objects, a significant fraction of the observed dust is located behind the X-ray source. Considering the distribution of COUP sources within this graph, it is clear that the linear relationship between the K-band and visual extinction cannot be observed as most data points exhibit A_K values above this function. Nevertheless, this information can be used to restrict the COUP data set in such a way that the X-ray absorption measurements and the observations of thermal dust emission trace the same material: Sources which are part of the linear relation are expected to fulfil this requirement and may thus constitute a reliable sample to study the $\frac{N_H}{A_K}$ ratio.

In Figure 25, the hydrogen column density is compared to the extinction as deduced from *Herschel* data, with the $\frac{A_K}{A_V}$ ratio indicated by different colours. For ratios lower than approximately 0.5, each of the three value ranges (indicated in green, dark blue and light blue) shows a systematic relation between N_H and A_K that follows an exponential function in a logarithmic plot. In particular, data points with $\frac{A_K}{A_V}$ values between 0.07 and 0.2 (indicated in light blue) appear to follow the $\frac{N_H}{A_K}$ relation that has been deduced

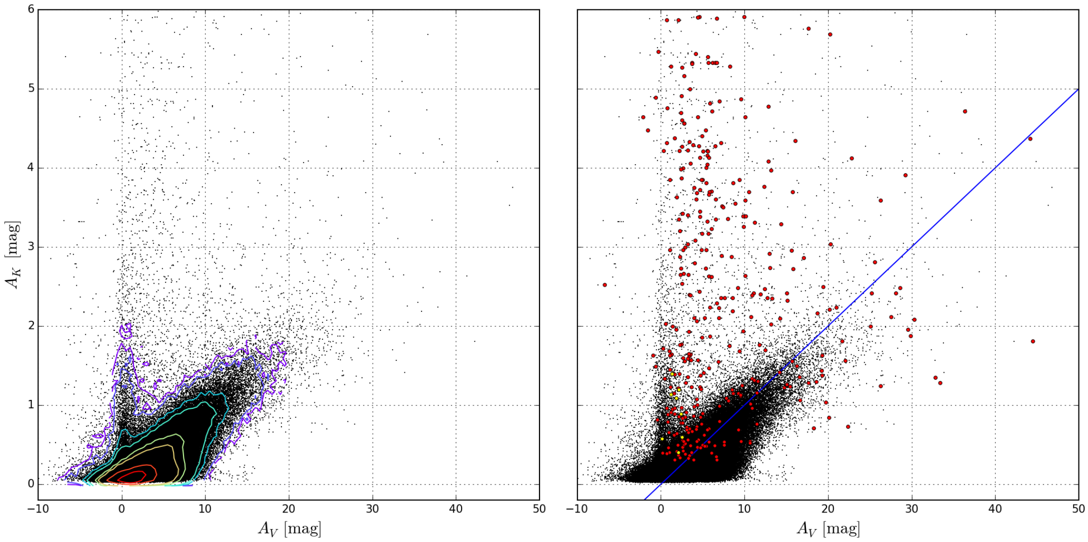

Figure 24: Extinction in the K band A_K as a function of visual extinction A_V calculated using the NICER algorithm and near-infrared colours from the VISION catalogue for the Orion A region. *Left:* Contours of a 2-dimensional histogram are shown to illustrate the data point density. The histogram is calculated using 100 bins each in the x and y axis. The contours correspond to a number of 5, 10, 50, 100, 500, 1 000, 5 000 and 10 000 data points per bin. *Right:* COUP sources are indicated by filled red circles. Foreground sources are plotted on top as yellow points. The blue line at $A_K = 0.1\,A_V$ is intended as a guide to the eye.

from VISION data. This statement remains true for typical values of R_V due to the weak dependency of $\frac{N_H}{A_K}$ on the parameter. For lower or higher values of the extinction ratio, namely $\frac{A_K}{A_V} < 0.07$ and $\frac{A_K}{A_V} > 0.2$, no clear statement can be made on the comparability of X-ray and microwave observations, as the majority of sources in Orion A follows a different trend. Therefore, the $\frac{N_H}{A_V}$ ratio calculated from near-infrared colours can be reproduced with data by *Planck* and *Herschel* if the sample can be restricted to sources for which comparable X-ray and microwave measurements are available.

4.3.4 Results and Discussion for the Pillitteri sample

The data analysis is performed in an analogous manner as for the COUP catalogue. However, the Pillitteri catalogue contains no information on possible complications that occurred during the fitting procedure, which is why only the χ^2 parameter can be used to assess the reliability of the hydrogen column density values. A comparison of N_H with the K-band extinction is shown in Figure 26, with near-infrared colours as given in the Pillitteri catalogue in Figure 27.

Similar to the COUP sources, no functional relation between hydrogen column densities and A_K can be observed. While a correlation is obvious for $(J - H)$ and $(H - K)$

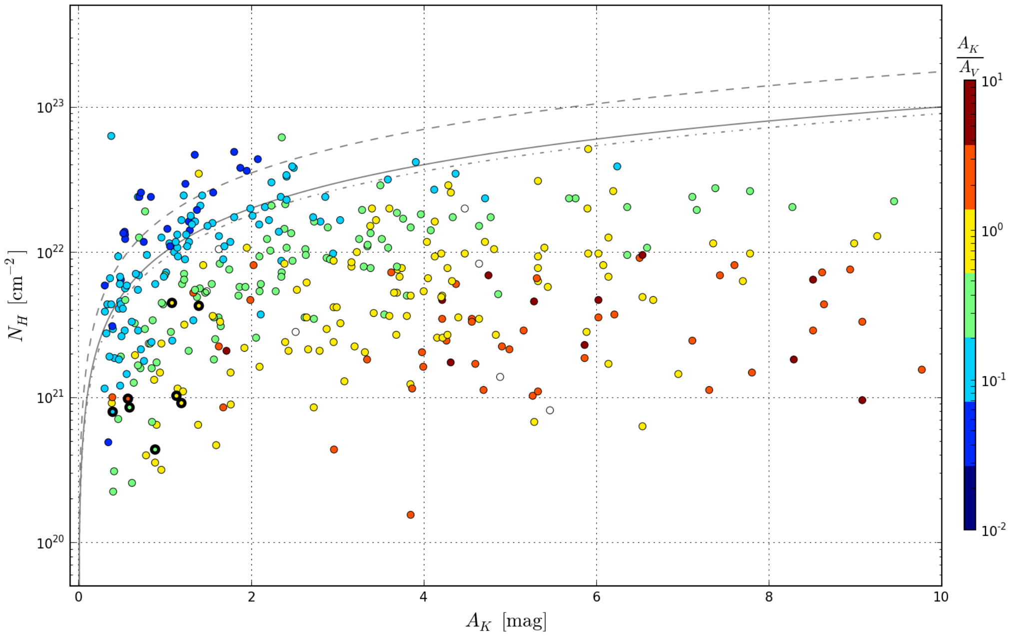

Figure 25: Hydrogen column density N_H as a function of extinction in the K band A_K for the COUP sample. Colours indicate ranges of values in the $\frac{A_K}{A_V}$ ratio. Foreground sources are plotted on top with thick black outlines. The dashed line corresponds to the galactic value of $\frac{N_H}{A_K} = 1.75 \cdot 10^{22}\ \frac{\mathrm{cm}^{-2}}{\mathrm{mag}}$, calculated from the galactic $\frac{N_H}{A_V}$ value assuming $R_V = 3.1$. The solid and dot-dashed line represent the relation found in this work, $\frac{N_H}{A_K} = 1.05 \cdot 10^{22}\ \frac{\mathrm{cm}^{-2}}{\mathrm{mag}}$ and $\frac{N_H}{A_K} = 8.92 \cdot 10^{21}\ \frac{\mathrm{cm}^{-2}}{\mathrm{mag}}$, using $R_V = 3.1$ and $R_V = 5.5$, respectively.

in the COUP sample, this is not the case for the sources in the Pillitteri catalogue. The same applies to the VISION magnitudes, which are in excellent agreement with the 2MASS data retrieved from the catalogue (see Figure 28). As a result, no correlation can be found between N_H and the visual extinction A_V calculated by employing the NICER algorithm. This is illustrated in Figure 29.

At this point it is unclear why this study fails to reveal a relation between X-ray absorption and dust extinction in the near-infrared for the Pillitteri sample. Due to the agreement between the magnitudes from 2MASS and VISION, the near-infrared colours can be excluded as a potential cause. A number of possible explanations are listed in the following:

(a) The COUP and Pillitteri catalogues are derived from two different instruments and differ in their assumed fitting models. Examining which procedure is more robust and leads to more reliable best-fit parameters would require a detailed analysis of the instrument and model characteristics.

(b) The Pillitteri sample contains 232 sources while more than 1 600 entries are listed in the COUP catalogue. Fewer data points may impair the clearness of the correlation.

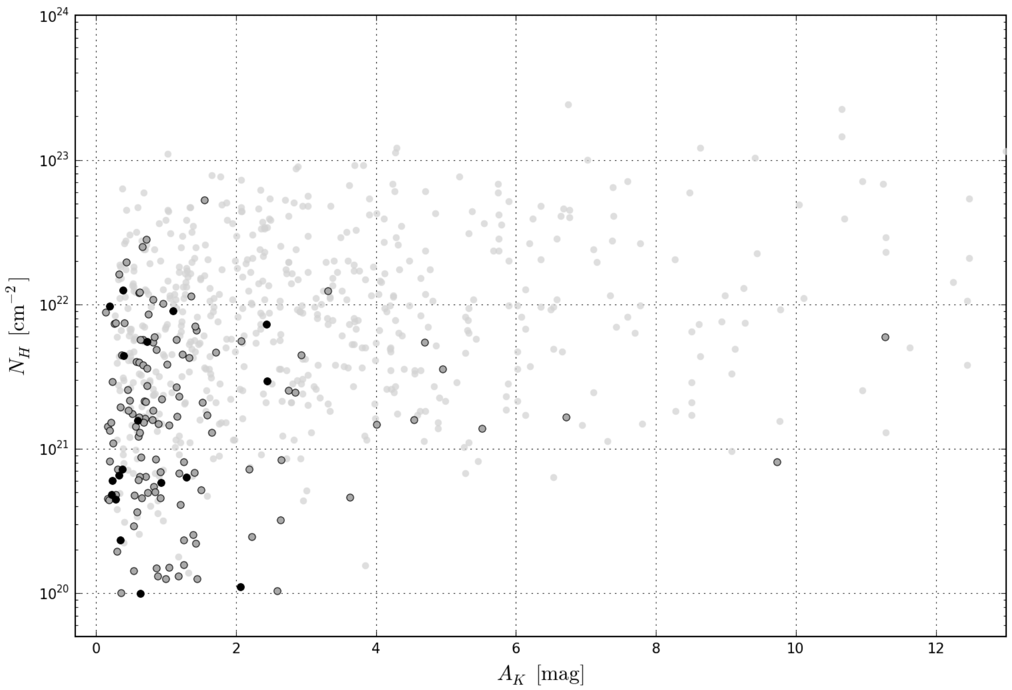

Figure 26: Hydrogen column density N_H as a function of extinction in the K band A_K for the Pillitteri sample. Foreground sources are plotted on top as black points. The COUP sources are indicated by semi-transparent points.

(c) The sources of the Pillitteri sample are distributed in the Orion A region. If considerable changes in the $\frac{N_H}{A_V}$ ratio occur within this area, no linear relation can be found even if sources with comparable X-ray and sub-millimetre measurements of the ISM are chosen.

Identifying the true explanation for the inconclusive results of this study would require an immense effort, as the original XMM-*Newton* and *Chandra* data as well as the automated fitting procedures used to create the catalogues would need to be reproduced, analysed and compared. It is therefore beyond the scope of this work to assess whether any of the reasons mentioned above provides the true cause of the observed non-correlation.

4.3.5 Conclusion

A comparison of the X-ray absorbing hydrogen column density and the extinction in the K band as derived from sub-millimetre observations for sources in the Orion A cloud and Orion Nebula Cluster exhibits no correlation between the two parameters. However, a clear linear relation can be found in the ONC if near-infrared colour magnitudes are employed as an alternative measurement of dust column density, indicating that a substantial amount of dust is located behind the objects. A linear fit of N_H as a function of the visual extinction A_V calculated from $(J - H)$ and $(H - K)$ using the NICER algorithm yields a slope significantly lower than the observed galactic value.

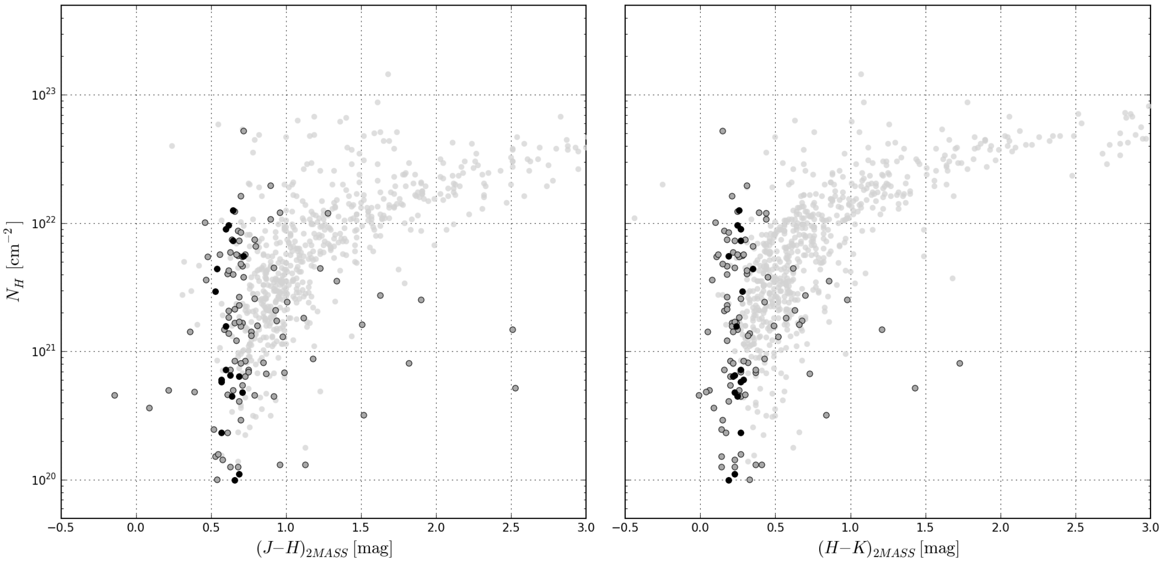

Figure 27: Hydrogen column density N_H as a function of near-infrared colours as given in the Pillitteri catalogue. Foreground sources are plotted on top as black points. The COUP sources are indicated by semi-transparent points.

While a change in the parameter R_V is not capable of reproducing the galactic relation, the discrepancy can be explained by a lower gas-to-dust mass ratio of approximately 60. Comparing the extinction deduced from microwave and near-infrared measurements, A_K and A_V, respectively, in the entire Orion A cloud, a linear relation can be observed for the majority of objects. This correlation is interpreted as an indication that the two measurements trace the same interstellar material. If the X-ray sources are constrained to objects following the linear relation, the $\frac{N_H}{A_K}$ ratio is compatible with the value of $\frac{N_H}{A_V}$ derived from near-infrared magnitudes. For reasons that have yet to be determined precisely, no correlation is observed for sources in the Pillitteri catalogue which are distributed in the Orion A region.

Similar to the previous studies in this work, this analysis shows that the restrictions defining the studied source sample need to be considered carefully. Here, additional observations in the near-infrared are required in order to asses the comparability of sub-millimetre and X-ray data. As an essential result, a significant difference in the gas-to-dust ratio between the average galactic value and the Orion Nebula Cluster region can be deduced, indicating variations in the properties of the dense and diffuse ISM.

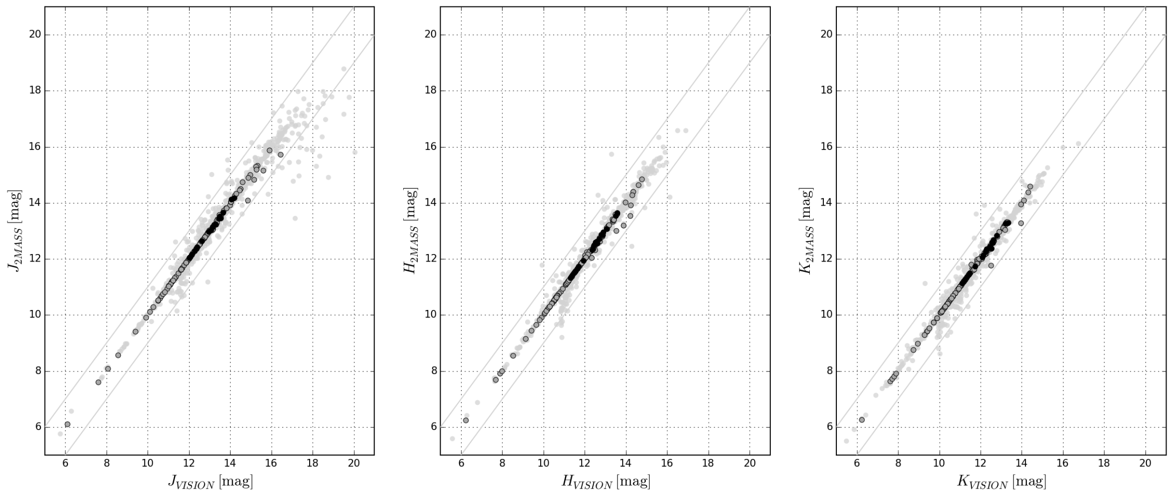

Figure 28: 2MASS and VISION near-infrared colour magnitudes compared for the Pillitteri sample. Foreground sources are plotted on top as black points. The COUP sources are indicated by semi-transparent points. Grey lines indicate a deviation of 1 mag from equality.

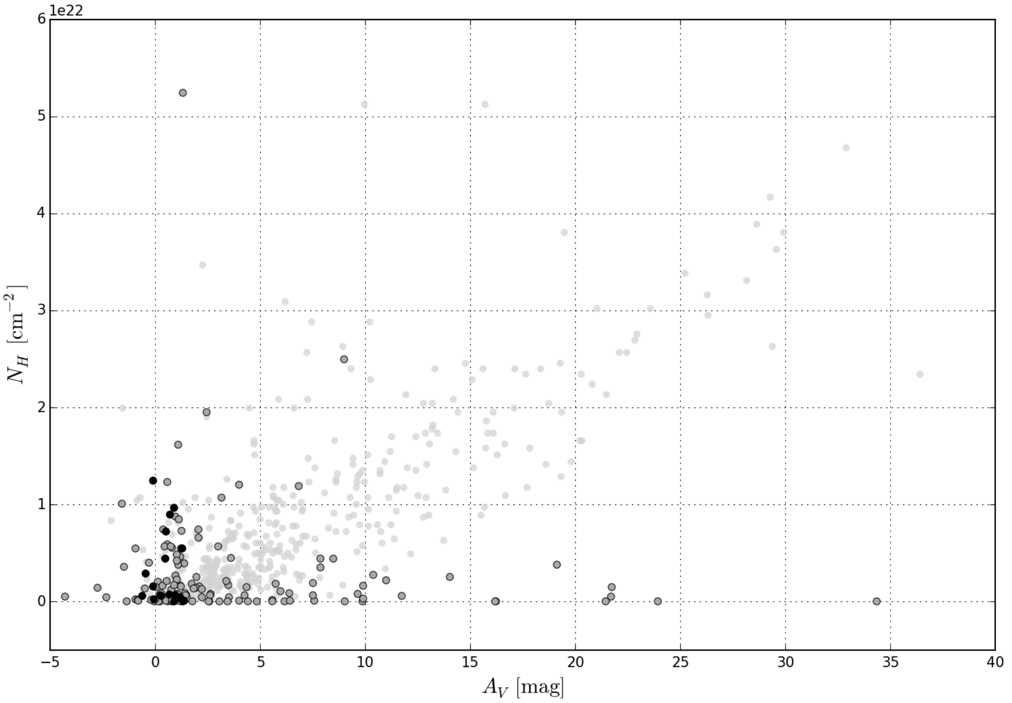

Figure 29: Hydrogen column density N_H as a function of extinction A_V calculated using the NICER algorithm and near-infrared colours from the VISION catalogue for the Pillitteri sample. Foreground sources are plotted on top as black points. The COUP sources are indicated by semi-transparent points.

5 Summary and Outlook

Deducing the properties of the diffuse ISM has proven to be a challenging task. The interpretation of the extended X-ray emission traced by the ROSAT satellite is complex due to the generally unknown arrangement of emitting and absorbing layers along the line of sight. Nevertheless, a correlation between soft X-ray intensity and dust optical depth as derived from *Planck* observations can be found for low values of τ_{353} in the majority of the examined regions. Substructures showing differences in the shape of their relation between X-ray intensity and optical depth can be observed within these regions. As the substructures do not show distinct dust temperatures, the various correlations are likely caused by different geometries of the emitting and absorbing large-scale structures. Therefore, the 3-dimensional arrangement of various phases of the ISM is found to represent a crucial aspect in the analysis of soft X-ray observations. Possible extensions of this study could include the separation of the entire ROSAT survey into substructures, collecting all available information on the emitting and absorbing objects along the line of sight towards these structures and finally, modelling each substructure individually. Well-known clouds of interstellar material are self-evident candidates for this approach.

In order to avoid the need to speculate on the origin of the observed X-ray radiation, background point sources are used in a second study. X-ray spectra from extragalactic point sources contain information on the absorbing column density N_H, which is directly proportional to the optical depth. Since galaxies can suffer from intrinsic absorption that is not correlated to the dust optical depth, the sample is restricted to broad-line AGN, resulting in a sample size of ten sources for which both X-ray data is available and the desired classification is confirmed by the SDSS catalogue. Only a weak correlation between N_H as derived from XMM-*Newton* spectra and the dust optical depth by *Planck* can be observed. Using optical colour magnitudes from the SDSS catalogue instead of τ_{353}, a strong linear correlation is found, while the near-infrared colours by 2MASS exhibit large errors that do not allow any statements on a functional relation. Similar to the previous analysis, the weak correlation between N_H and τ_{353} may be caused by the fact that the column density is measured to the position of the X-ray source whereas thermal dust emission traces the optical depth along the entire line of sight. Although the study suggests that the properties of the ISM change across the sky, the small sample size does not allow firm conclusions to be drawn. Therefore, as a potential improvement of this analysis, the number of sources in the sample would need to be increased. This could involve

- increasing the overall number of observed sources in both the XMM-*Newton* and the SDSS catalogue,
- increasing the number of classified sources within the SDSS catalogue,
- obtaining reliable estimates of the intrinsic absorption of extragalactic sources and expanding the sample to contain all galaxies, or
- finding another type of extragalactic source that shows little intrinsic absorption.

Additionally, better constraints on the (non-)correlation in different wavelength ranges could be derived if the uncertainties of near-infrared data on extragalactic sources were reduced and the errors of the absorbing column density would represent the instrumental uncertainties as well as fitting errors. As an alternative, the sample could include more nearby objects such as young stars within a cloud, rather than extragalactic sources. Since the interpretation of *Planck* data is not straight-forward in this case, other measures of dust column densities would need to be used, for example near-infrared extinction, with the advantage of lower observational uncertainties. If a clear correlation can be observed and the distance to the stellar object is known, a comparison with the optical depth as measured by *Planck* could provide information on the amount of interstellar material in front of and behind the star.

This path is followed in the last study of this work examining the Orion Nebula Cluster. An extinction map produced from *Planck* and *Herschel* data is correlated with the X-ray source catalogue of the *Chandra* Orion Ultradeep Project and the VISTA near-infrared survey VISION. While a clear relation between the near-infrared colour magnitudes and the absorbing hydrogen column density derived from X-ray spectra exists, no correlation with the dust extinction from *Herschel* can be observed. The VISION data provide a means for restricting the source sample to objects for which X-ray and sub-millimetre measurements trace the same interstellar matter. The derived ratio between hydrogen column density and visual extinction is significantly lower than the value reported for the Milky Way in the literature, which may be caused by a lower gas-to-dust mass ratio of approximately 60. In order to confirm this number, measurements of elemental abundances and depletion factors would need to be considered. Furthermore, an estimate of the 3-dimensional structure of the dense material could be produced if the distances to individual stars were known.

All in all, this work has revealed that the target selection for studies of the ISM is crucial. In analyses of the diffuse ISM on large spatial scales, the distribution of interstellar structures altering the X-ray spectrum has a major impact on the deduction of physical properties. For point sources, the position relative to the absorbing and emitting matter determines whether X-ray and sub-millimetre measurements trace the same interstellar material and a study of the gas and dust in both the dense and diffuse ISM is possible. The approaches followed in this work point towards a dynamic and non-uniform nature of the ISM, providing evidence against the common practice of assuming constant properties of the ISM throughout the entire sky.

Bibliography

C. P. Ahn, R. Alexandroff, C. Allende Prieto, S. F. Anderson, T. Anderton, B. H. Andrews, É. Aubourg, S. Bailey, E. Balbinot, R. Barnes, et al. *The Ninth Data Release of the Sloan Digital Sky Survey: First Spectroscopic Data from the SDSS-III Baryon Oscillation Spectroscopic Survey.* Astrophysical Journal, Supplement, 203:21, December 2012.

J. Alves and H. Bouy. *Orion revisited. I. The massive cluster in front of the Orion nebula cluster.* Astronomy and Astrophysics, 547:A97, November 2012.

E. Anders and M. Ebihara. *Solar-system abundances of the elements.* Geochimica Cosmochimica Acta, 46:2363–2380, November 1982.

M. Audard, A. Güdel, A. Sres, R. Mewe, A. J. J. Raassen, E. Behar, C. R. Foley, and R. L. J. van der Meer. *A Study of the Coronal Plasma in RS CVn Binary Systems.* In A. Brown, G. M. Harper, and T. R. Ayres, editors, *The Future of Cool-Star Astrophysics: 12th Cambridge Workshop on Cool Stars, Stellar Systems, and the Sun*, volume 12 of *Cambridge Workshop on Cool Stars, Stellar Systems, and the Sun*, October 2003.

E. E. Barnard. *On a nebulous groundwork in the constellation Taurus.* Astrophysical Journal, 25:218–225, April 1907.

H. Bouy, J. Alves, E. Bertin, L. M. Sarro, and D. Barrado. *Orion revisited. II. The foreground population to Orion A.* Astronomy and Astrophysics, 564:A29, April 2014.

C. S. Bowyer, G. B. Field, and J. E. Mack. *Detection of an Anisotropic Soft X-ray Background Flux.* Nature, 217:32–34, January 1968.

D. N. Burrows and J. A. Mendenhall. *Soft X-ray shadowing by the Draco cloud.* Nature, 351: 629–631, June 1991.

J. A. Cardelli, G. C. Clayton, and J. S. Mathis. *The relationship between infrared, optical, and ultraviolet extinction.* Astrophysical Journal, 345:245–256, October 1989.

L. Carrasco, S. E. Strom, and K. M. Strom. *Interstellar dust in the Rho Ophiuchi dark cloud.* Astrophysical Journal, 182:95–109, May 1973.

M. R. Collier, S. L. Snowden, M. Sarantos, M. Benna, J. A. Carter, T. E. Cravens, W. M. Farrell, S. Fatemi, H. K. Hills, R. R. Hodges, M. Holmström, K. D. Kuntz, F. S. Porter, A. Read, I. P. Robertson, S. F. Sembay, D. G. Sibeck, T. J. Stubbs, P. Travnicek, and B. M. Walsh. *On lunar exospheric column densities and solar wind access beyond the terminator from ROSAT soft X-ray observations of solar wind charge exchange.* Journal of Geophysical Research (Planets), 119:1459–1478, July 2014.

A. Comastri, G. Setti, G. Zamorani, and G. Hasinger. *The contribution of AGNs to the X-ray background.* Astronomy and Astrophysics, 296:1, April 1995.

A. Corral, I. Georgantopoulos, S. Rosen, M. G. Watson, K. Page, and G. C. Stewart. *The XMM-Newton spectral-fit database.* In *IAU Symposium*, volume 304 of *IAU Symposium*, July 2014. doi: 10.1017/S1743921314003615.

J. W. den Herder, A. C. Brinkman, S. M. Kahn, G. Branduardi-Raymont, K. Thomsen, H. Aarts, M. Audard, J. V. Bixler, A. J. den Boggende, J. Cottam, T. Decker, L. Dubbeldam, C. Erd, H. Goulooze, M. Güdel, P. Guttridge, C. J. Hailey, K. A. Janabi, J. S. Kaastra, P. A. J. de Korte, B. J. van Leeuwen, C. Mauche, A. J. McCalden, R. Mewe, A. Naber, F. B. Paerels, J. R. Peterson, A. P. Rasmussen, K. Rees, I. Sakelliou, M. Sako, J. Spodek, M. Stern, T. Tamura, J. Tandy, C. P. de Vries, S. Welch, and A. Zehnder. *The Reflection Grating Spectrometer on board XMM-Newton.* Astronomy and Astrophysics, 365:L7–L17, January 2001.

B. T. Draine. *Physics of the Interstellar and Intergalactic Medium.* Princeton University Press, 2011a.

B. T. Draine. *Astronomical Models of PAHs and Dust.* In C. Joblin and A. G. G. M. Tielens, editors, *EAS Publications Series*, volume 46 of *EAS Publications Series*, March 2011b. doi: 10.1051/eas/1146003.

G. Fabbiano. *Populations of X-Ray Sources in Galaxies.* Annual Review of Astronomy and Astrophysics, 44:323–366, September 2006.

K. M. Ferrière. *The interstellar environment of our galaxy.* Reviews of Modern Physics, 73: 1031–1066, October 2001.

M. J. Freyberg and R. Egger. *ROSAT PSPC All-Sky Survey: completion and new spectral analysis of the diffuse soft X-ray background maps.* In B. Aschenbach and M. J. Freyberg, editors, *Highlights in X-ray Astronomy*, 1999.

G. P. Garmire, M. W. Bautz, P. G. Ford, J. A. Nousek, and G. R. Ricker, Jr. *Advanced CCD imaging spectrometer (ACIS) instrument on the Chandra X-ray Observatory.* In J. E. Truemper and H. D. Tananbaum, editors, *X-Ray and Gamma-Ray Telescopes and Instruments for Astronomy*, volume 4851 of *Society of Photo-Optical Instrumentation Engineers (SPIE) Conference Series*, March 2003. doi: 10.1117/12.461599.

K. V. Getman, E. Flaccomio, P. S. Broos, N. Grosso, M. Tsujimoto, L. Townsley, G. P. Garmire, J. Kastner, J. Li, F. R. Harnden, Jr., S. Wolk, S. S. Murray, C. J. Lada, A. A. Muench, M. J. McCaughrean, G. Meeus, F. Damiani, G. Micela, S. Sciortino, J. Bally, L. A. Hillenbrand, W. Herbst, T. Preibisch, and E. D. Feigelson. *Chandra Orion Ultradeep Project: Observations and Source Lists.* Astrophysical Journal, Supplement, 160:319–352, October 2005.

K. M. Górski, E. Hivon, A. J. Banday, B. D. Wandelt, F. K. Hansen, M. Reinecke, and M. Bartelmann. *HEALPix: A Framework for High-Resolution Discretization and Fast Analysis of Data Distributed on the Sphere.* Astrophysical Journal, 622:759–771, April 2005.

J. E. Gunn, W. A. Siegmund, E. J. Mannery, R. E. Owen, C. L. Hull, R. F. Leger, L. N. Carey, G. R. Knapp, D. G. York, W. N. Boroski, S. M. Kent, R. H. Lupton, C. M. Rockosi, M. L. Evans, P. Waddell, J. E. Anderson, J. Annis, J. C. Barentine, L. M. Bartoszek, S. Bastian, S. B. Bracker, H. J. Brewington, C. I. Briegel, J. Brinkmann, Y. J. Brown, M. A. Carr, P. C. Czarapata, C. C. Drennan, T. Dombeck, G. R. Federwitz, B. A. Gillespie, C. Gonzales, S. U. Hansen, M. Harvanek, J. Hayes, W. Jordan, E. Kinney, M. Klaene, S. J. Kleinman, R. G. Kron, J. Kresinski, G. Lee, S. Limmongkol, C. W. Lindenmeyer, D. C. Long, C. L. Loomis, P. M. McGehee, P. M. Mantsch, E. H. Neilsen, Jr., R. M. Neswold, P. R. Newman, A. Nitta,

J. Peoples, Jr., J. R. Pier, P. S. Prieto, A. Prosapio, C. Rivetta, D. P. Schneider, S. Snedden, and S.-i. Wang. *The 2.5 m Telescope of the Sloan Digital Sky Survey.* Astronomical Journal, 131:2332–2359, April 2006.

L. A. Hillenbrand. *On the Stellar Population and Star-Forming History of the Orion Nebula Cluster.* Astronomical Journal, 113:1733–1768, May 1997.

F. Jansen, D. Lumb, B. Altieri, J. Clavel, M. Ehle, C. Erd, C. Gabriel, M. Guainazzi, P. Gondoin, R. Much, R. Munoz, M. Santos, N. Schartel, D. Texier, and G. Vacanti. *XMM-Newton observatory. I. The spacecraft and operations.* Astronomy and Astrophysics, 365:L1–L6, January 2001.

J. S. Kaastra and R. Mewe. *X-ray emission from thin plasmas. I - Multiple Auger ionisation and fluorescence processes for Be to Zn.* Astronomy and Astrophysics, Supplement, 97:443–482, January 1993.

D. Kazanas, K. Fukumura, E. Behar, I. Contopoulos, and C. Shrader. *Toward a Unifed AGN Structure.* The Astronomical Review, 7(3):92–123, July 2012.

R. S. Klessen and S. C. O. Glover. *Physical Processes in the Interstellar Medium.* ArXiv e-prints, December 2014.

E. Kruegel. *The physics of interstellar dust.* The Institute of Physics Publishing, 2003.

K. D. Kuntz and S. L. Snowden. *Deconstructing the Spectrum of the Soft X-Ray Background.* Astrophysical Journal, 543:195–215, November 2000.

C. J. Lada, E. A. Lada, D. P. Clemens, and J. Bally. *Dust extinction and molecular gas in the dark cloud IC 5146.* Astrophysical Journal, 429:694–709, July 1994.

B. D. Lehmer, D. M. Alexander, F. E. Bauer, W. N. Brandt, A. D. Goulding, L. P. Jenkins, A. Ptak, and T. P. Roberts. *A Chandra Perspective on Galaxy-wide X-ray Binary Emission and its Correlation with Star Formation Rate and Stellar Mass: New Results from Luminous Infrared Galaxies.* Astrophysical Journal, 724:559–571, November 2010.

A. P. Lightman and G. B. Rybicki. *X-rays from active galactic nuclei - Inverse Compton reflection.* Astrophysical Journal, Letters, 229:L15–L18, April 1979.

M. Lombardi and J. Alves. *Mapping the interstellar dust with near-infrared observations: An optimized multi-band technique.* Astronomy and Astrophysics, 377:1023–1034, October 2001.

M. Lombardi, H. Bouy, J. Alves, and C. J. Lada. *Herschel-Planck dust optical-depth and column-density maps. I. Method description and results for Orion.* Astronomy and Astrophysics, 566:A45, June 2014.

J. S. Mathis and S. G. Wallenhorst. *The size distribution of interstellar particles. III - Peculiar extinctions and normal infrared extinction.* Astrophysical Journal, 244:483–492, March 1981.

J. S. Mathis, W. Rumpl, and K. H. Nordsieck. *The size distribution of interstellar grains.* Astrophysical Journal, 217:425–433, October 1977.

D. McCammon, D. N. Burrows, W. T. Sanders, and W. L. Kraushaar. *The soft X-ray diffuse background.* Astrophysical Journal, 269:107–135, June 1983.

S. T. Megeath, R. Gutermuth, J. Muzerolle, E. Kryukova, K. Flaherty, J. L. Hora, L. E. Allen, L. Hartmann, P. C. Myers, J. L. Pipher, J. Stauffer, E. T. Young, and G. G. Fazio. *The Spitzer Space Telescope Survey of the Orion A and B Molecular Clouds. I. A Census of Dusty Young Stellar Objects and a Study of Their Mid-infrared Variability.* Astronomical Journal, 144:192, December 2012.

K. M. Menten, M. J. Reid, J. Forbrich, and A. Brunthaler. *The distance to the Orion Nebula.* Astronomy and Astrophysics, 474:515–520, November 2007.

R. Morrison and D. McCammon. *Interstellar photoelectric absorption cross sections, 0.03-10 keV.* Astrophysical Journal, 270:119–122, July 1983.

G. L. Pilbratt, J. R. Riedinger, T. Passvogel, G. Crone, D. Doyle, U. Gageur, A. M. Heras, C. Jewell, L. Metcalfe, S. Ott, and M. Schmidt. *Herschel Space Observatory. An ESA facility for far-infrared and submillimetre astronomy.* Astronomy and Astrophysics, 518:L1, July 2010.

I. Pillitteri, S. J. Wolk, S. T. Megeath, L. Allen, J. Bally, M. Gagné, R. A. Gutermuth, L. Hartman, G. Micela, P. Myers, J. M. Oliveira, S. Sciortino, F. Walter, L. Rebull, and J. Stauffer. *An X-Ray Survey of the Young Stellar Population of the Lynds 1641 and Iota Orionis Regions.* Astrophysical Journal, 768:99, May 2013.

Planck Collaboration. *The Scientific Programme of Planck.* ArXiv Astrophysics e-prints, April 2006.

Planck Collaboration, A. Abergel, P. A. R. Ade, N. Aghanim, M. I. R. Alves, G. Aniano, C. Armitage-Caplan, M. Arnaud, M. Ashdown, F. Atrio-Barandela, et al. *Planck 2013 results. XI. All-sky model of thermal dust emission.* Astronomy and Astrophysics, 571:A11, November 2014.

C. E. Ryter. *Interstellar Extinction from Infrared to X-Rays: an Overview.* Astrophysics and Space Science, 236:285–291, February 1996.

M. F. Skrutskie, R. M. Cutri, R. Stiening, M. D. Weinberg, S. Schneider, J. M. Carpenter, C. Beichman, R. Capps, T. Chester, J. Elias, J. Huchra, J. Liebert, C. Lonsdale, D. G. Monet, S. Price, P. Seitzer, T. Jarrett, J. D. Kirkpatrick, J. E. Gizis, E. Howard, T. Evans, J. Fowler, L. Fullmer, R. Hurt, R. Light, E. L. Kopan, K. A. Marsh, H. L. McCallon, R. Tam, S. Van Dyk, and S. Wheelock. *The Two Micron All Sky Survey (2MASS).* Astronomical Journal, 131:1163–1183, February 2006.

R. K. Smith, N. S. Brickhouse, D. A. Liedahl, and J. C. Raymond. *Collisional Plasma Models with APEC/APED: Emission-Line Diagnostics of Hydrogen-like and Helium-like Ions.* Astrophysical Journal, Letters, 556:L91–L95, August 2001.

S. L. Snowden, D. P. Cox, D. McCammon, and W. T. Sanders. *A model for the distribution of material generating the soft X-ray background.* Astrophysical Journal, 354:211–219, May 1990.

S. L. Snowden, D. McCammon, D. N. Burrows, and J. A. Mendenhall. *Analysis procedures for ROSAT XRT/PSPC observations of extended objects and the diffuse background.* Astrophysical Journal, 424:714–728, April 1994.

S. L. Snowden, M. J. Freyberg, P. P. Plucinsky, J. H. M. M. Schmitt, J. Truemper, W. Voges, R. J. Edgar, D. McCammon, and W. T. Sanders. *First Maps of the Soft X-Ray Diffuse Background from the ROSAT XRT/PSPC All-Sky Survey.* Astrophysical Journal, 454:643, December 1995.

S. L. Snowden, R. Egger, M. J. Freyberg, D. McCammon, P. P. Plucinsky, W. T. Sanders, J. H. M. M. Schmitt, J. Trümper, and W. Voges. *ROSAT Survey Diffuse X-Ray Background Maps. II.* Astrophysical Journal, 485:125–135, August 1997.

S. L. Snowden, M. J. Freyberg, K. D. Kuntz, and W. T. Sanders. *A Catalog of Soft X-Ray Shadows, and More Contemplation of the 1/4 KEV Background.* Astrophysical Journal, Supplement, 128:171–212, May 2000.

Y. Sofue. *The North Polar Spur and Aquila Rift.* Monthly Notices of the Royal Astronomical Society, 447:3824–3831, March 2015.

L. Spitzer. *Physical processes in the interstellar medium.* Wiley-VCH, 1978.

W. Sutherland, J. Emerson, G. Dalton, E. Atad-Ettedgui, S. Beard, R. Bennett, N. Bezawada, A. Born, M. Caldwell, P. Clark, S. Craig, D. Henry, P. Jeffers, B. Little, A. McPherson, J. Murray, M. Stewart, B. Stobie, D. Terrett, K. Ward, M. Whalley, and G. Woodhouse. *The Visible and Infrared Survey Telescope for Astronomy (VISTA): Design, technical overview, and performance.* Astronomy and Astrophysics, 575:A25, March 2015.

J. A. Tauber, ESA Scientific Collaboration, and Planck Scientific Collaboration. *The Planck mission.* Advances in Space Research, 34:491–496, January 2004.

J. E. Trümper and G. Hasinger. *The Universe in X-Rays.* Springer, 2008.

M. H. Vuong, T. Montmerle, N. Grosso, E. D. Feigelson, L. Verstraete, and H. Ozawa. *Determination of the gas-to-dust ratio in nearby dense clouds using X-ray absorption measurements.* Astronomy and Astrophysics, 408:581–599, September 2003.

M. C. Weisskopf, B. Brinkman, C. Canizares, G. Garmire, S. Murray, and L. P. Van Speybroeck. *An Overview of the Performance and Scientific Results from the Chandra X-Ray Observatory.* Publications of the ASP, 114:1–24, January 2002.

J. Wilms, A. Allen, and R. McCray. *On the Absorption of X-Rays in the Interstellar Medium.* Astrophysical Journal, 542:914–924, October 2000.

V. Zubko, E. Dwek, and R. G. Arendt. *Interstellar Dust Models Consistent with Extinction, Emission, and Abundance Constraints.* Astrophysical Journal, Supplement, 152:211–249, June 2004.

Appendix

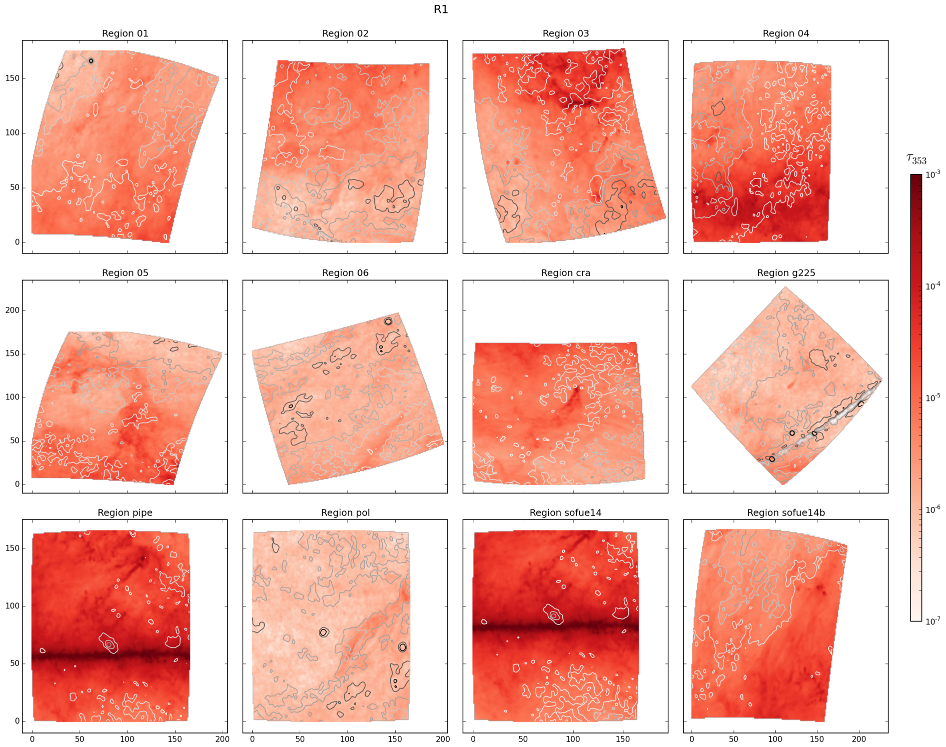

Figure 30: Comparison of X-ray intensity (contours) and dust optical depth (red colour-scale image) in the R1 energy band, where darker colours correspond to higher values. The x and y axis give the position in ROSAT pixels. The contours have been smoothed using a 1.5-σ Gaussian kernel and correspond to (50, 100, 200, 300, 400, 600 and 800) $\cdot 10^{-6}\ \frac{\text{counts}}{\text{s}\cdot\text{arcmin}^2}$. In Region g225, the stripe of low values almost parallel to the lower right edge of the image is caused by a thin area on the sky without valid ROSAT data.

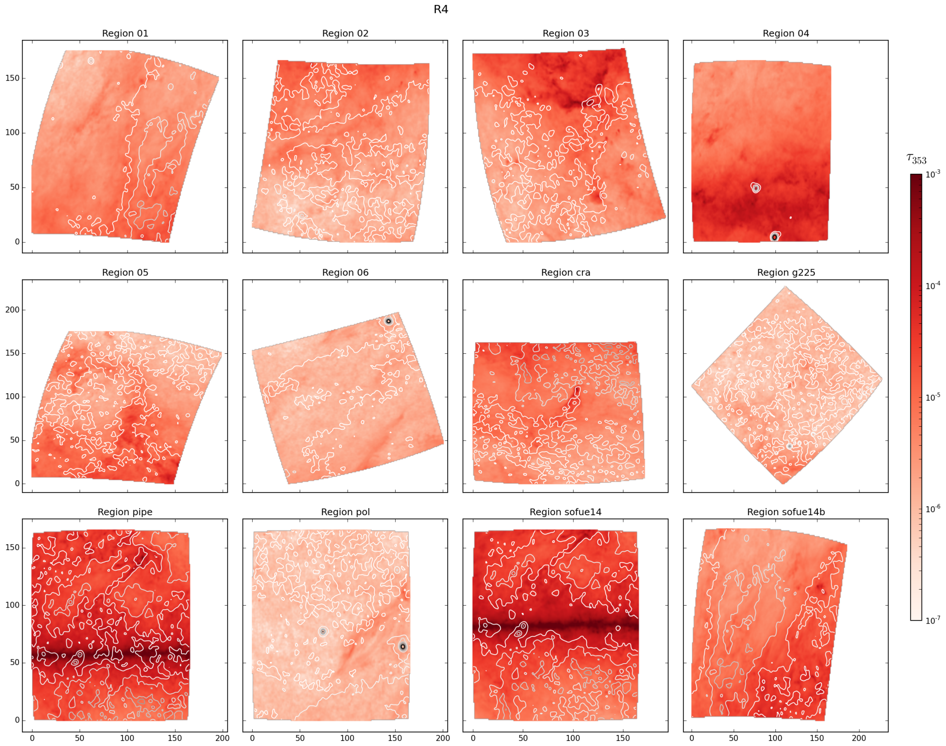

Figure 31: Same as Figure 30, but for R4.

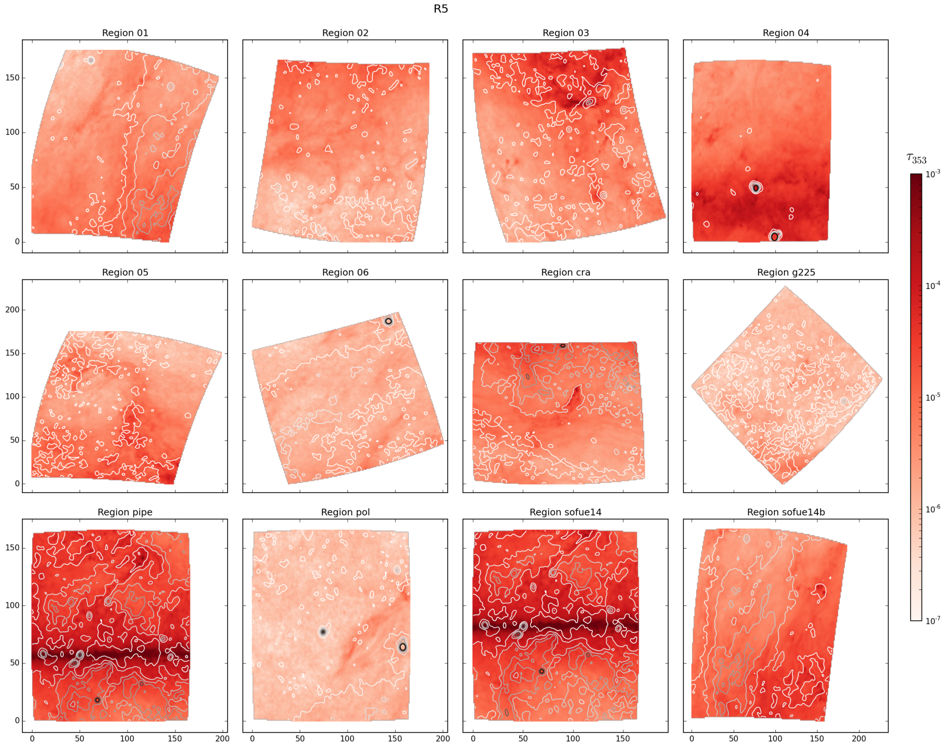

Figure 32: Same as Figure 30, but for R5.

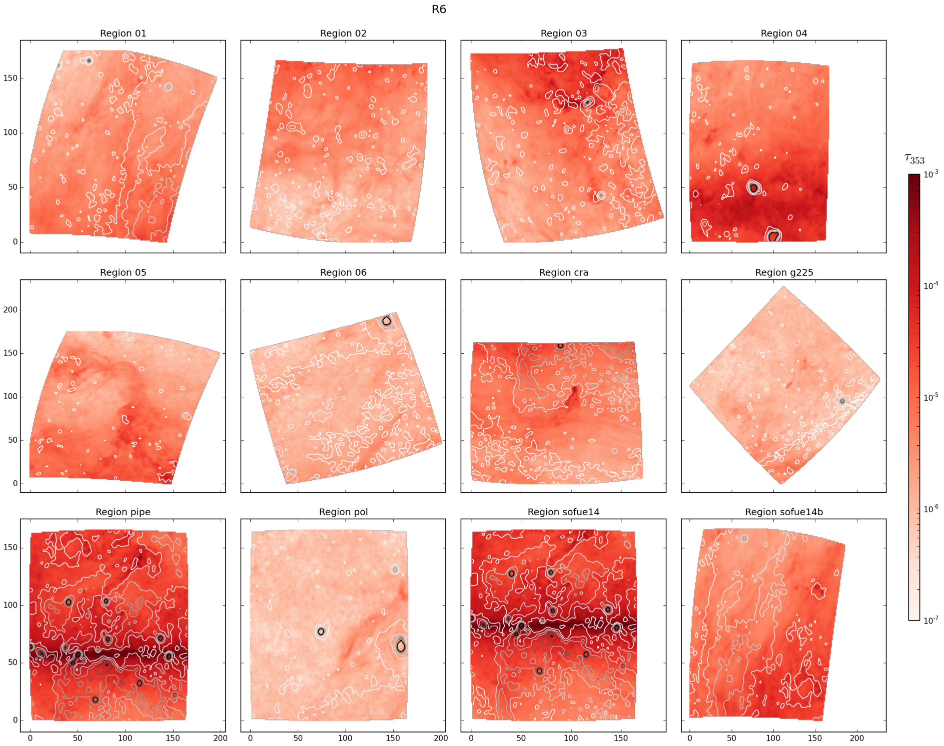

Figure 33: Same as Figure 30, but for R6.

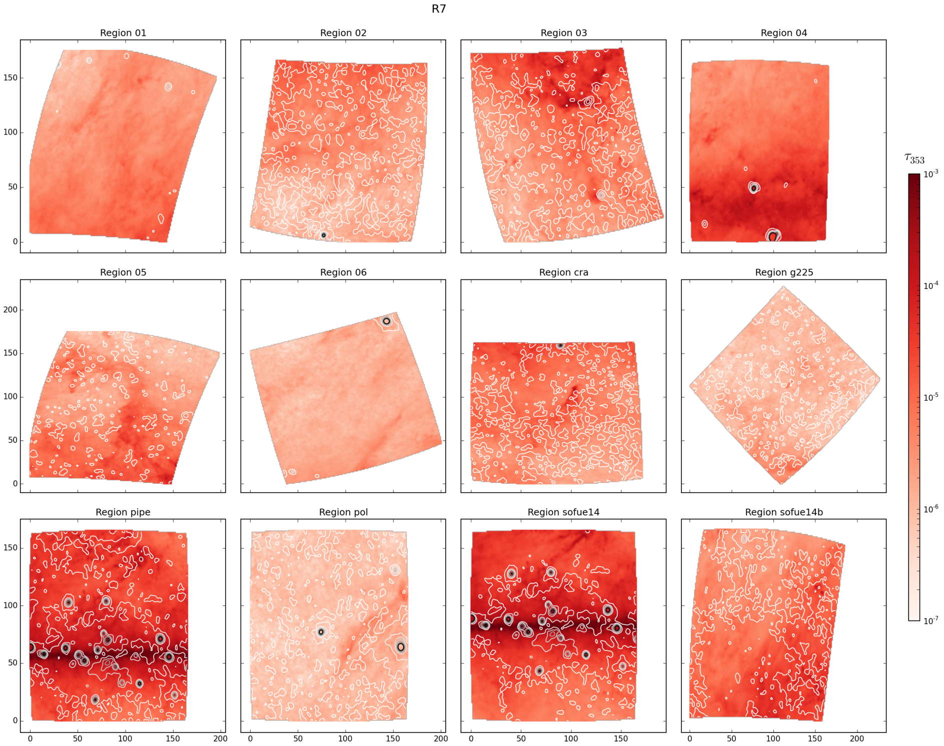

Figure 34: Same as Figure 30, but for R7.

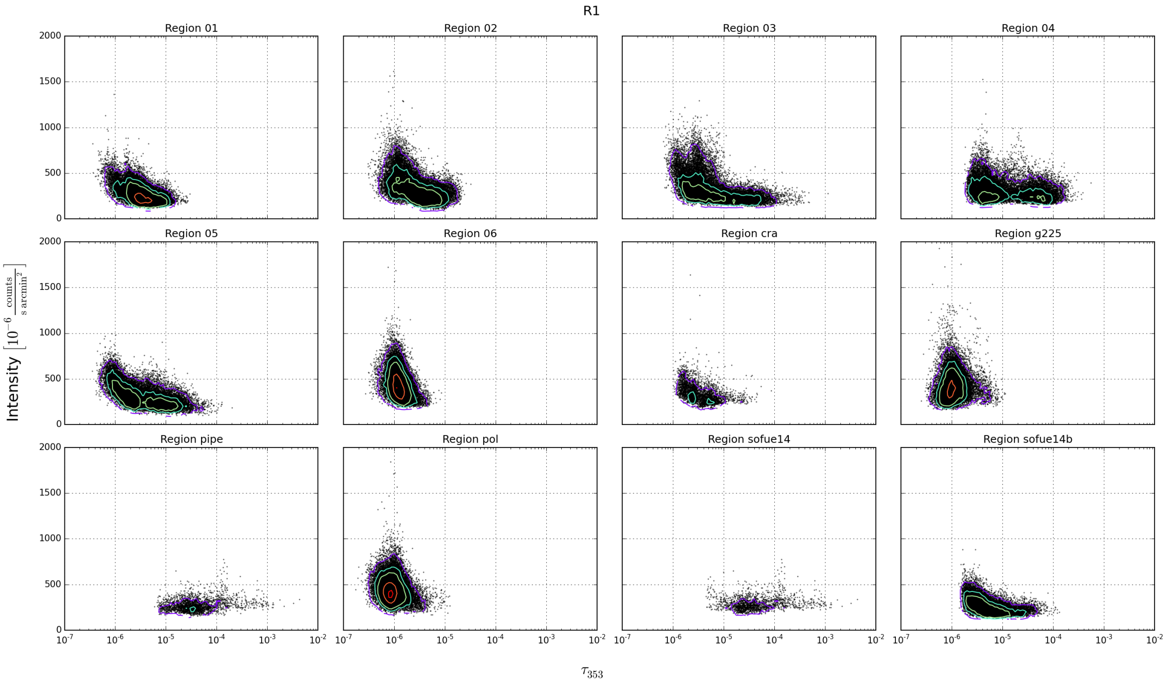

Figure 35: X-ray intensity in the R1 band as a function of dust optical depth. Every data point corresponds to one pixel. Contours of a 2-dimensional histogram are shown to illustrate the data point density. The histogram is calculated using 100 bins in the x and 50 bins in the y axis. The contours correspond to a number of 10, 50, 100, 300 and 500 data points per bin.

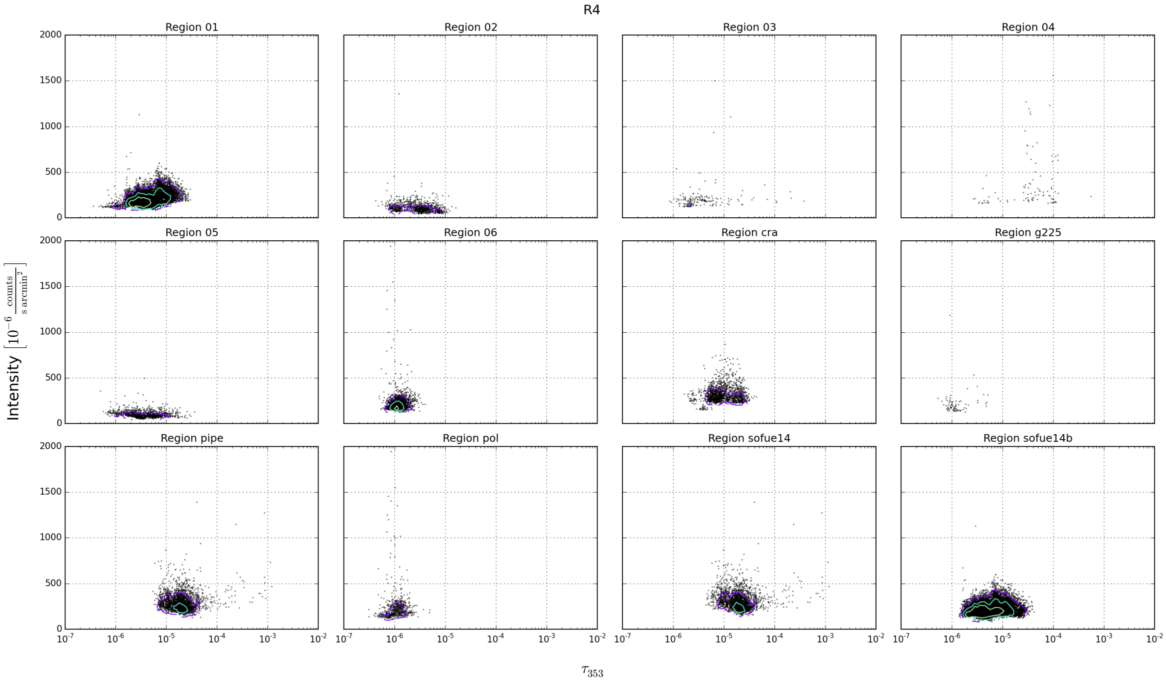

Figure 36: Same as Figure 35, but for R4.

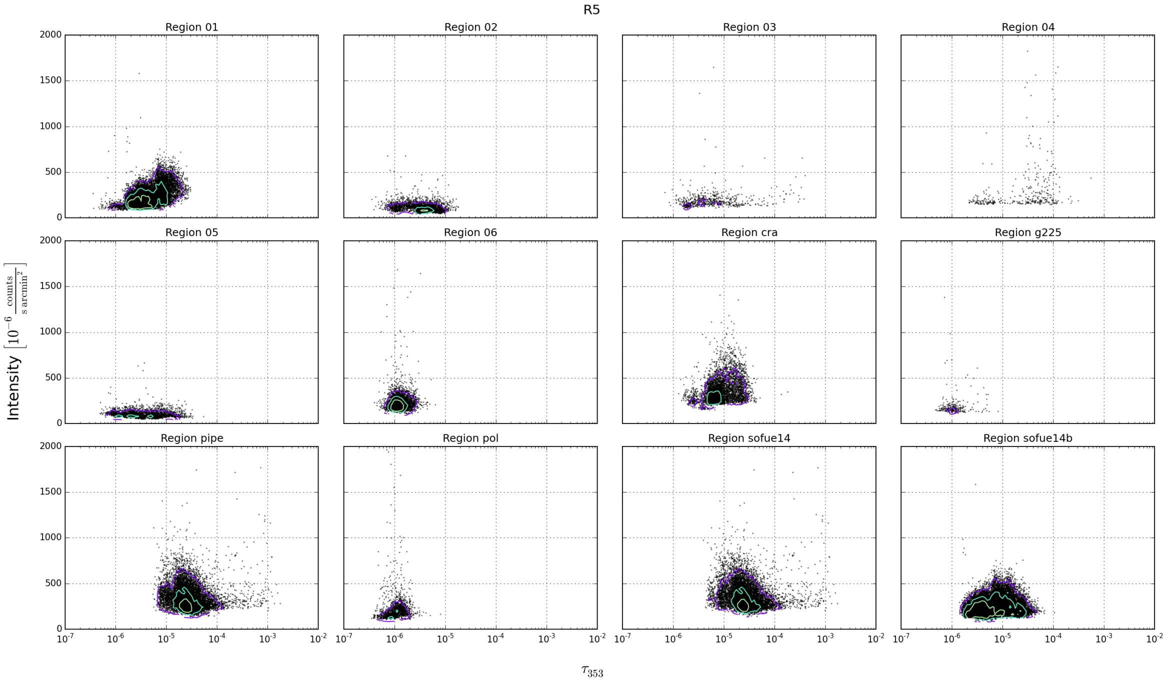

Figure 37: Same as Figure 35, but for R5.

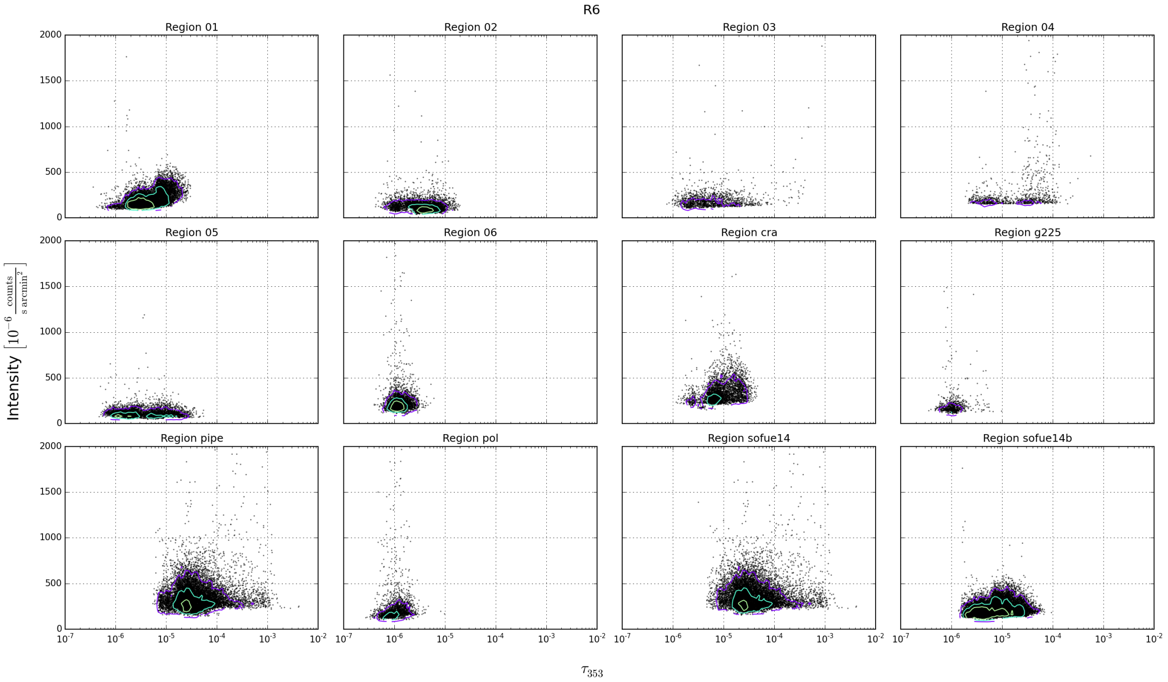

Figure 38: Same as Figure 35, but for R6.

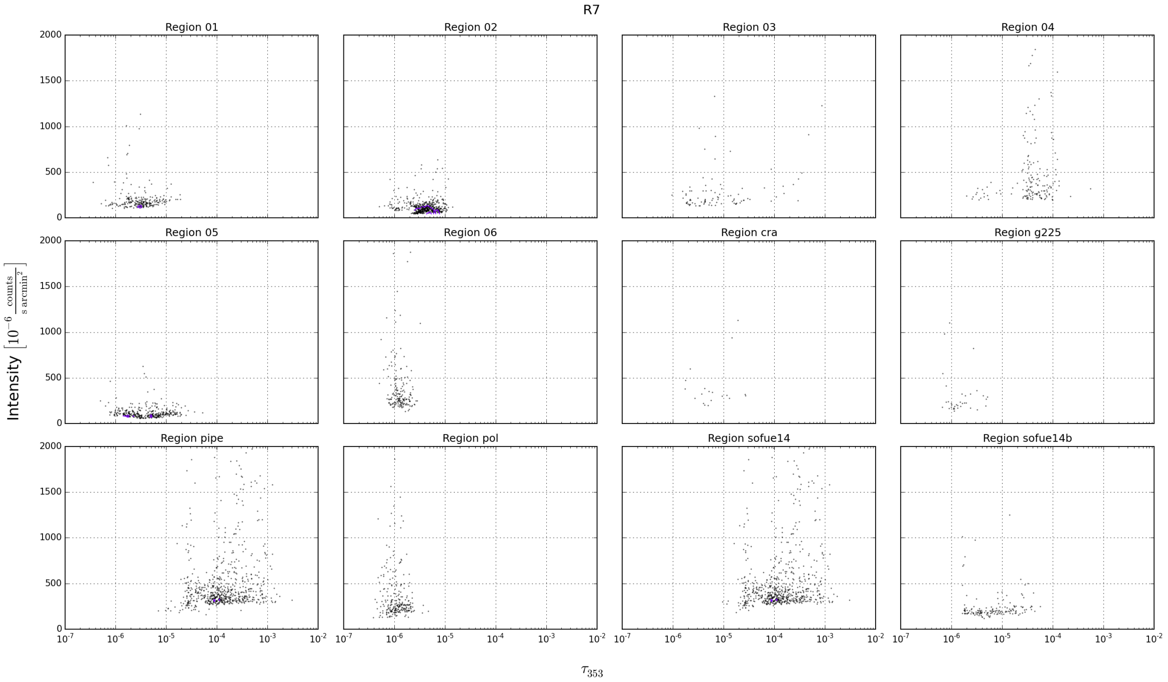

Figure 39: Same as Figure 35, but for R7.

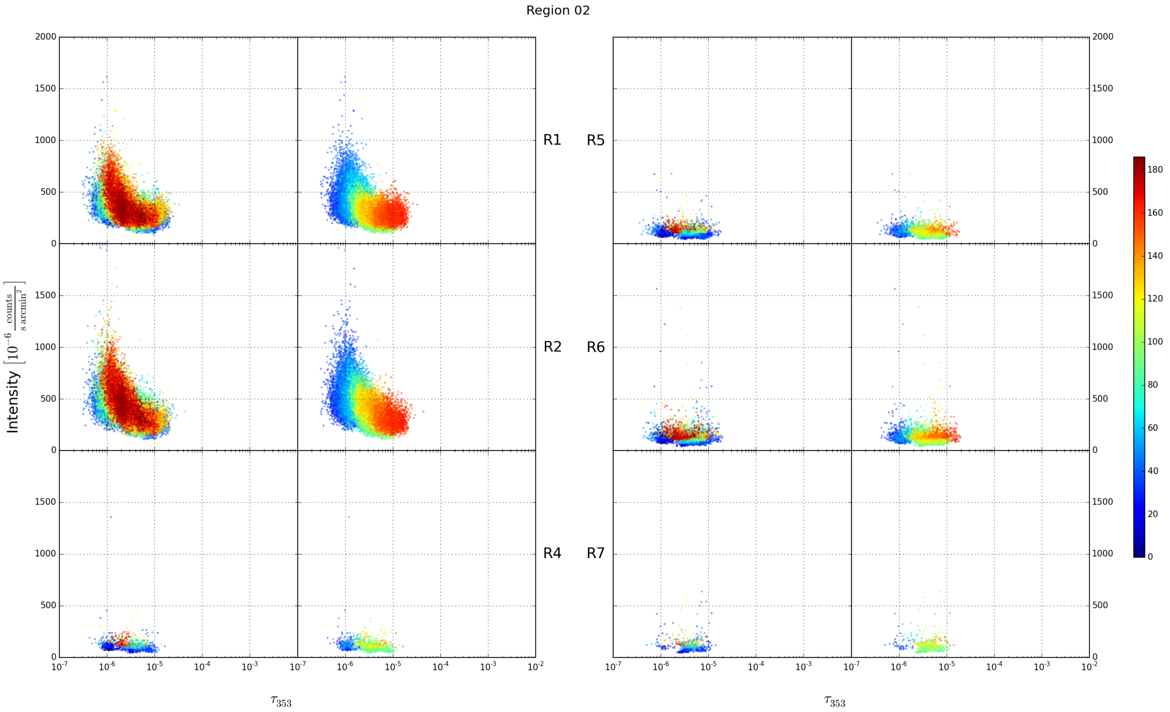

Figure 40: X-ray intensity as a function of dust optical depth in Region 02 for all bands, colour-coded with the pixel position. For each band, the left and right graphs show the position on the x and yaxis, respectively. The data points are semi-transparent and those with higher values in x or y are plotted on top.

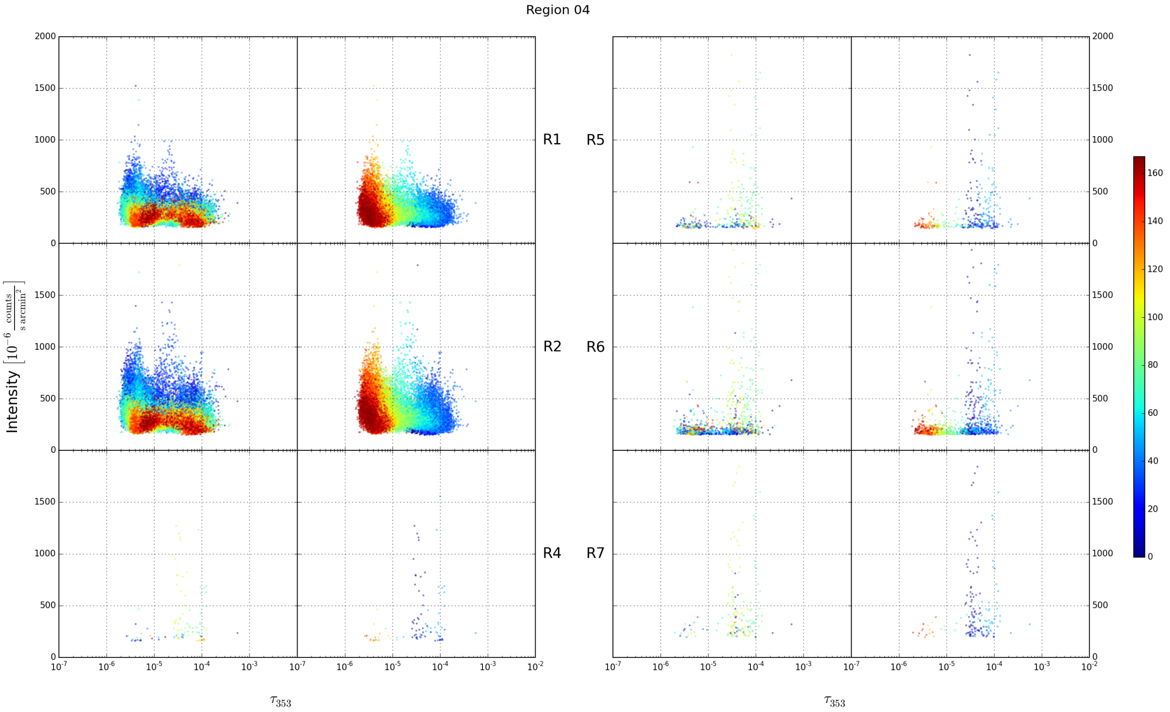

Figure 41: Same as Figure 40, but for Region 04.

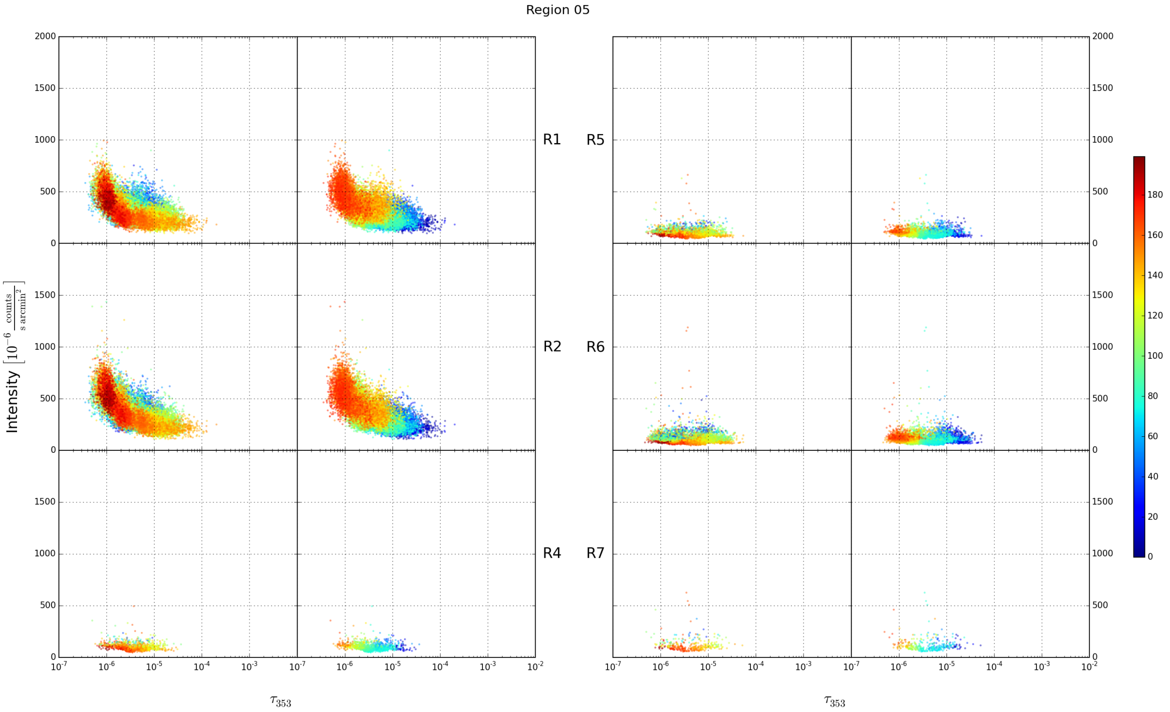

Figure 42: Same as Figure 40, but for Region 05.

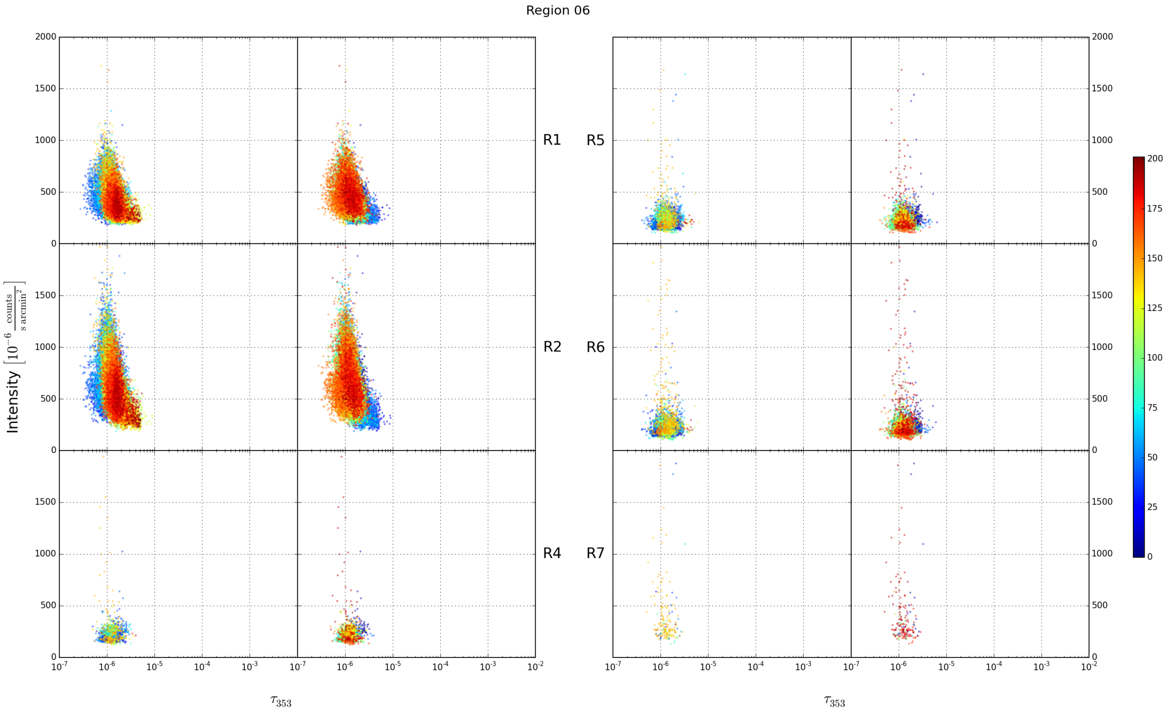

Figure 43: Same as Figure 40, but for Region 06.

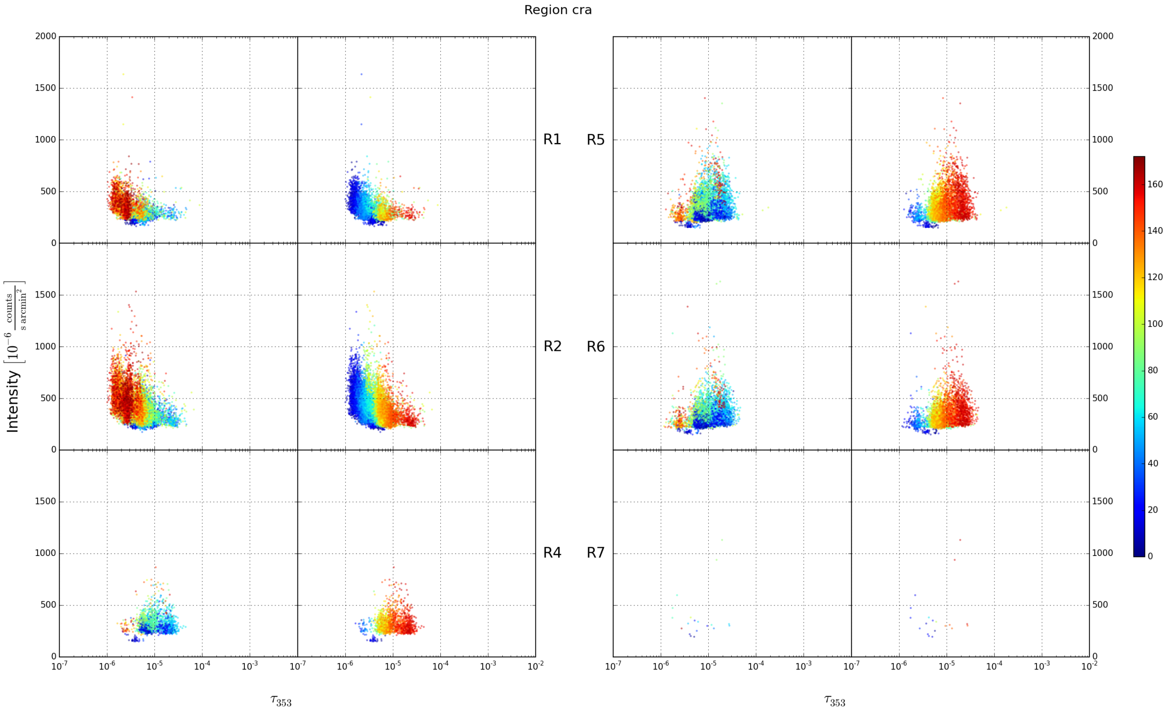

Figure 44: Same as Figure 40, but for Region cra.

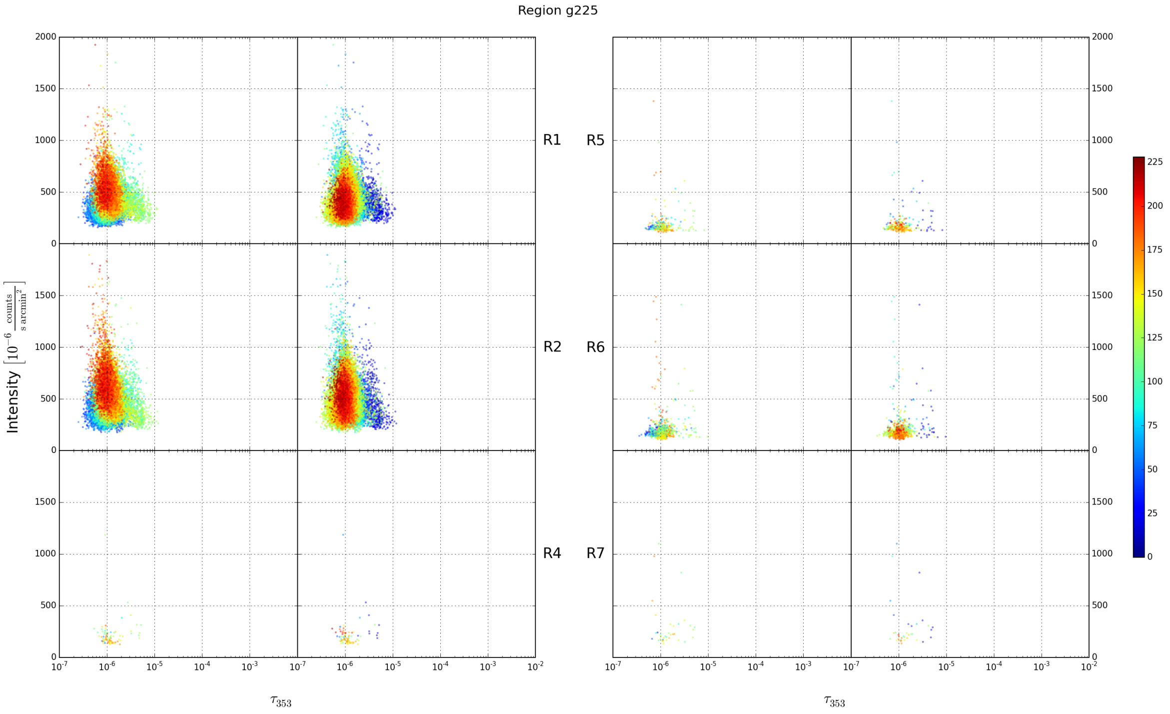

Figure 45: Same as Figure 40, but for Region g225.

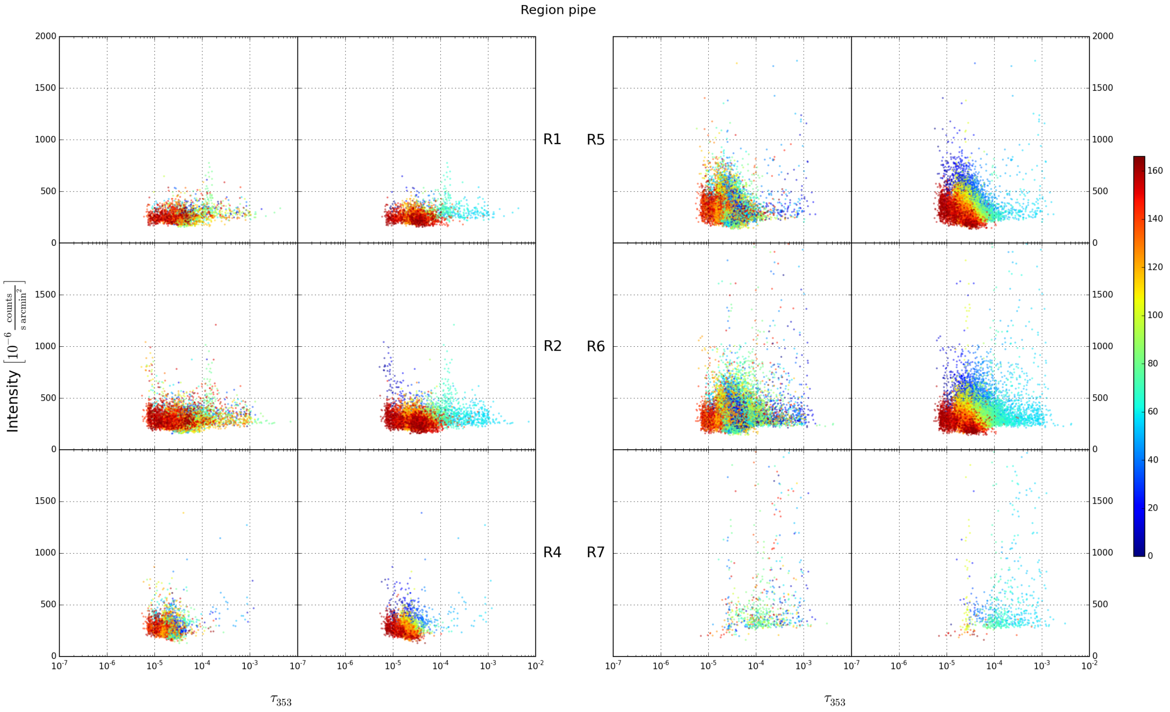

Figure 46: Same as Figure 40, but for Region pipe.

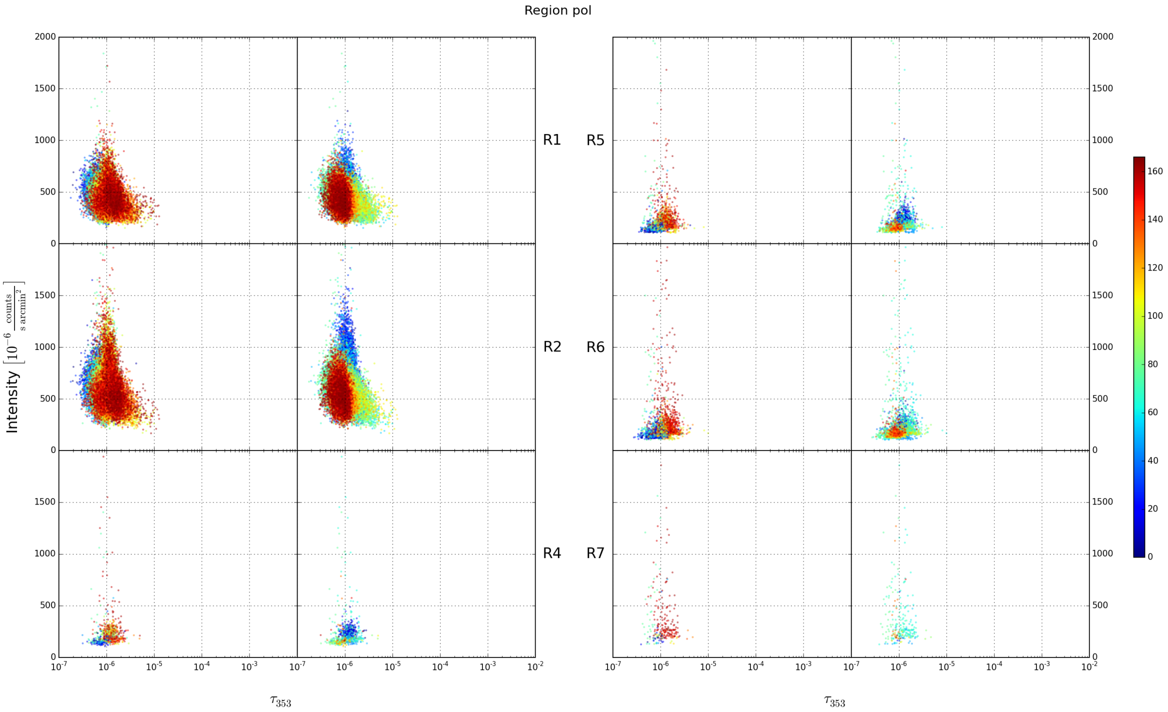

Figure 47: Same as Figure 40, but for Region pol.

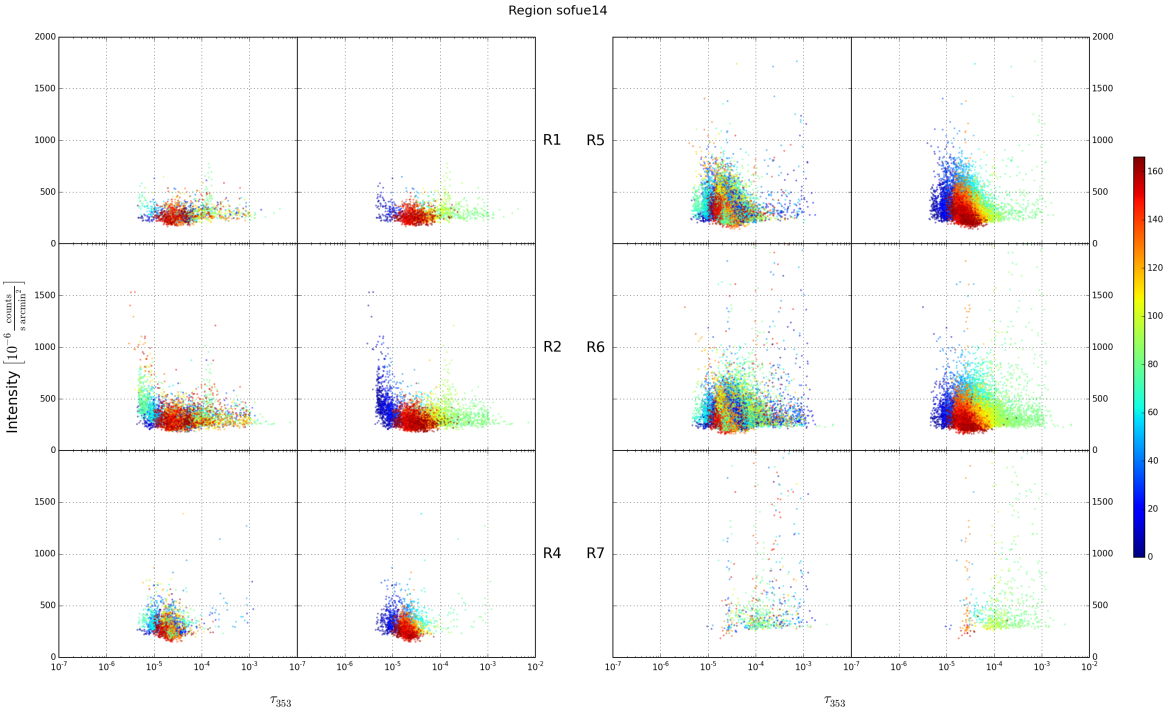

Figure 48: Same as Figure 40, but for Region sofue14.

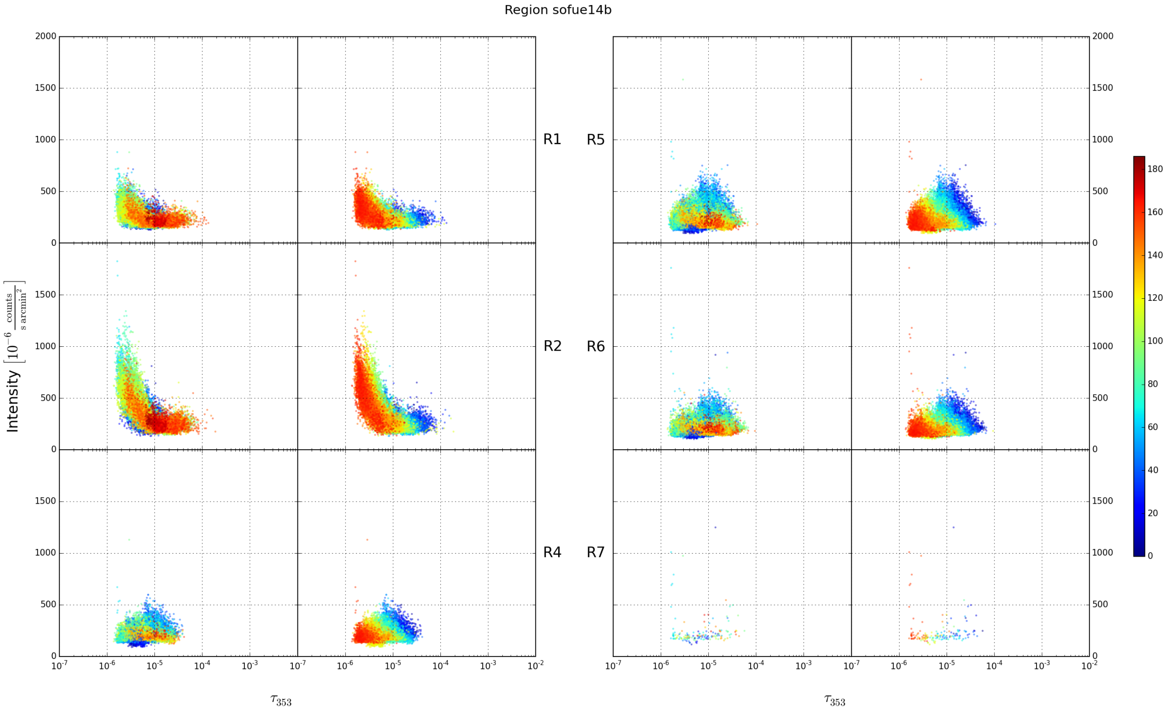

Figure 49: Same as Figure 40, but for Region sofue14b.

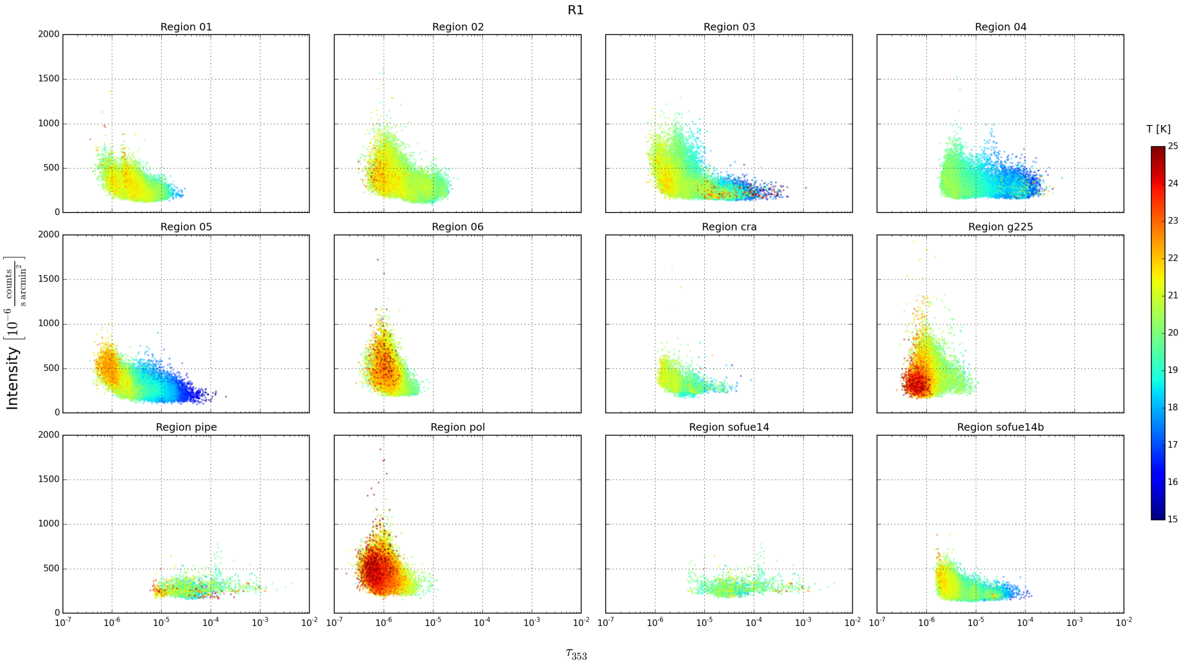

Figure 50: X-ray intensity as a function of dust optical depth in the R1 band, colour-coded with the dust temperature. The data points are semi-transparent and those with higher temperature values are plotted on top.

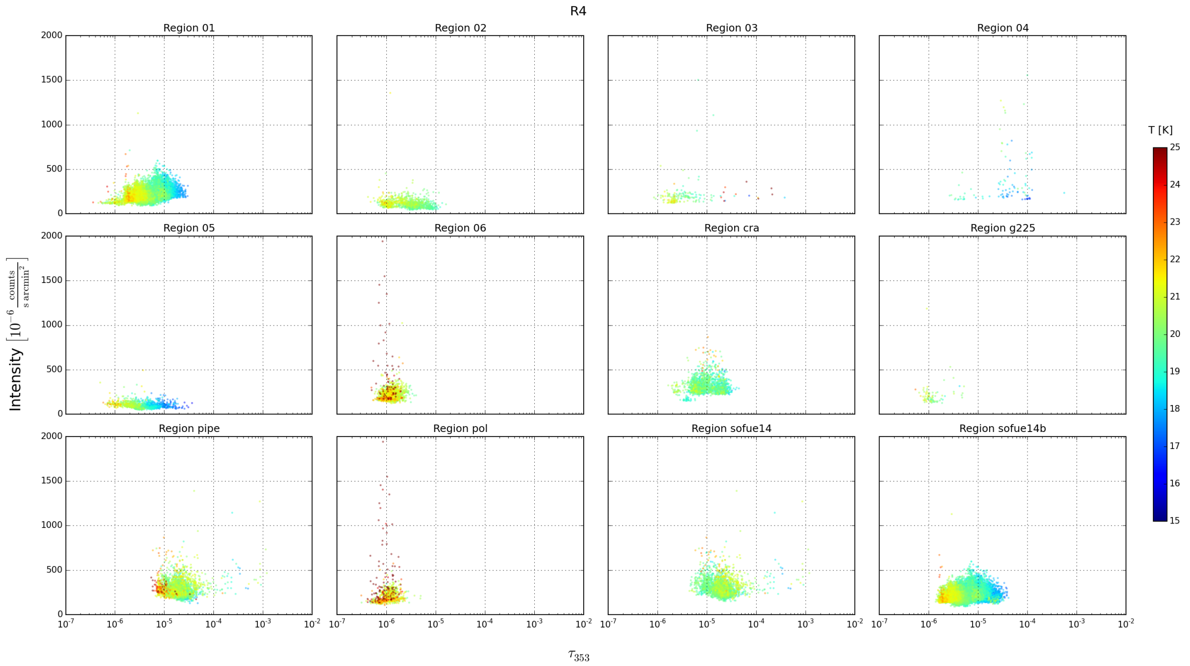

Figure 51: Same as Figure 50, but for R4.

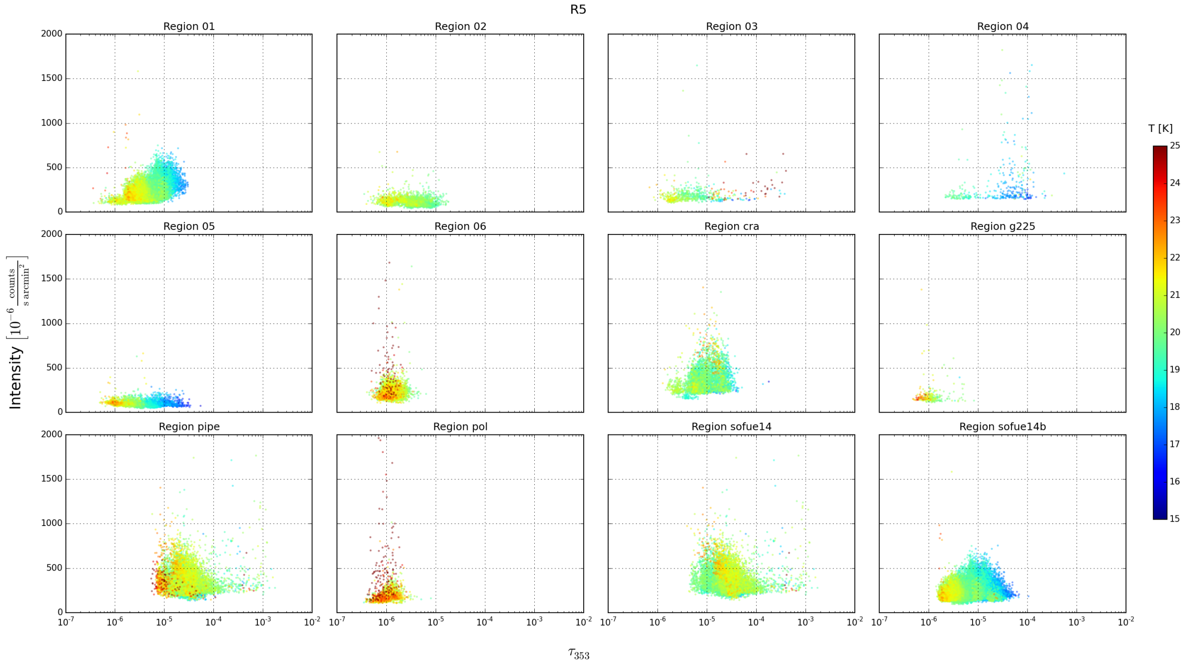

Figure 52: Same as Figure 50, but for R5.

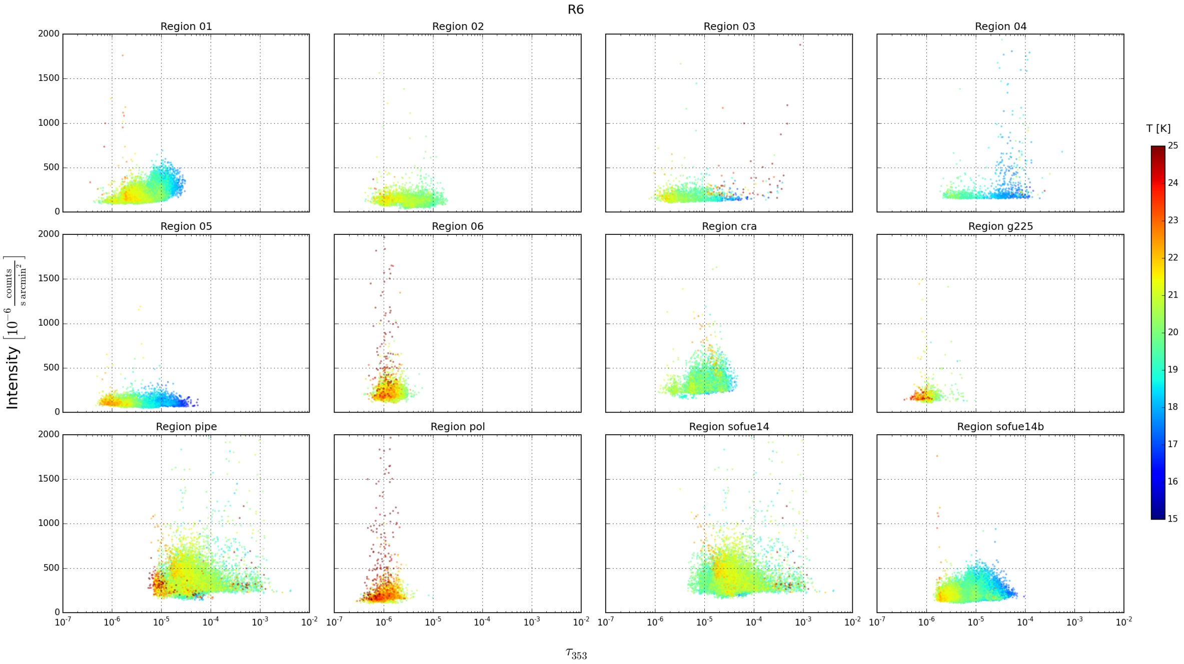

Figure 53: Same as Figure 50, but for R6.

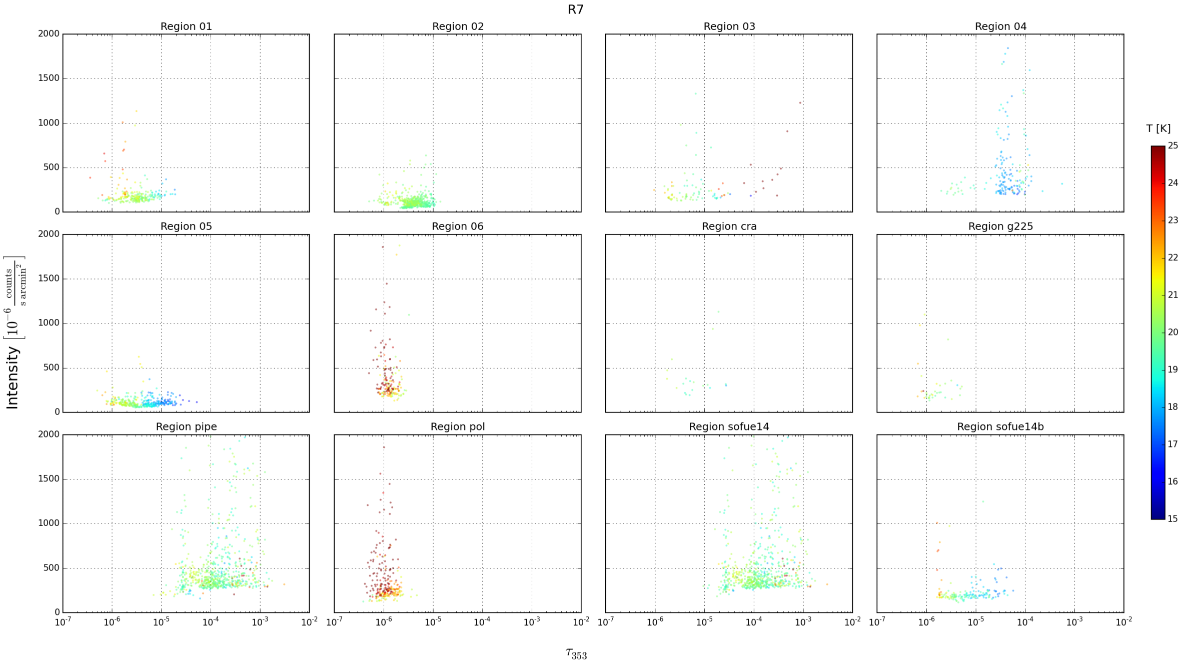

Figure 54: Same as Figure 50, but for R7.

Acknowledgements

In the following, I would like to express my gratitude towards a number of people who have supported me during the work on this thesis.

First, I would like to thank my supervisors at the Institute of Astrophysics, Prof. João Alves and Dr. Jan Forbrich for their excellent guidance, patience and shared expertise. I have had the privilege of working as part of Prof. Alves' research group which provided a motivating work environment and added to the quality of this thesis in several aspects. In particular, I am indebted to Stefan Meingast for making his VISION catalogue available to me and Kieran Leschinski for his Python realisation of the NICER algorithm. I would also like to show my gratitude towards my supervisor at the Vienna University of Technology, Prof. Helmut Leeb, without whom I would not have had the possibility to conduct this research as a collaboration with the University of Vienna.

I am very grateful to Prof. Gerhard Pfeiffer, an exceptionally committed teacher who has woken my interest in astronomy at an early stage. Without the curiosity and passion for this field that he conveyed to his students I may never have dared to turn towards astrophysics during my recent years of study.

Finally, I would like to thank my family and friends. I am very lucky to have parents who supported me throughout my studies in a number of ways and a brother who has a major impact on my language skills and academic aspirations. I would also like to thank Peter Lackner for his continuous and invaluable support and encouragement during the last four years.